

NPS 68-89-008

NAVAL POSTGRADUATE SCHOOL Monterey, California

AD-A219 858



THESIS

THE EFFECTS OF CLIMATOLOGICAL AND TRANSIENT
WIND FORCING ON EDDY GENERATION
IN THE CALIFORNIA CURRENT SYSTEM

by

Robert W. Edson

September, 1989

Thesis Advisor:

M.L. Batteen

Approved for public release; distribution is unlimited.

Prepared for:
Office of Naval Research
800 N. Quincy Street
Arlington, VA 22217-5000

DTIC
SELECTED
MAR 29 1990
S B D

90 03 28 10%

NAVAL POSTGRADUATE SCHOOL
Monterey, CA. 93943

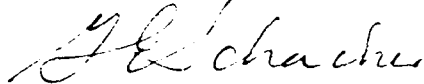
Rear Admiral Ralph W. West, Jr.
Superintendent

Harrison Shull
Provost

This report was prepared in conjunction with research conducted for Chief of Naval Research and Funded by the Naval Postgraduate School.

Reproduction of this report is authorized.

Released By:



GORDON E. SCHACHER
Dean of Science and Engineering

Unclassified

SECURITY CLASSIFICATION OF THIS PAGE

REPORT DOCUMENTATION PAGE				Form Approved OMB No. 0704-0188	
1a REPORT SECURITY CLASSIFICATION Unclassified		1b RESTRICTIVE MARKINGS			
2a SECURITY CLASSIFICATION AUTHORITY		3 DISTRIBUTION / AVAILABILITY OF REPORT Approved for public distribution; distribution is unlimited.			
2b DECLASSIFICATION / DOWNGRADING SCHEDULE					
4. PERFORMING ORGANIZATION REPORT NUMBER(S) NPS-68-89-008		5. MONITORING ORGANIZATION REPORT NUMBER(S)			
6a. NAME OF PERFORMING ORGANIZATION Naval Postgraduate School	6b. OFFICE SYMBOL (If applicable) 68	7a. NAME OF MONITORING ORGANIZATION Office of Naval Research			
6c. ADDRESS (City, State, and ZIP Code) Monterey, CA 93943-5000		7b. ADDRESS (City, State, and ZIP Code) 800 N. Quincy St., Arlington, VA 22217-5000			
8a. NAME OF FUNDING / SPONSORING ORGANIZATION Naval Postgraduate School	8b. OFFICE SYMBOL (If applicable)	9 PROCUREMENT INSTRUMENT IDENTIFICATION NUMBER O&MN, Direct Funding			
8c. ADDRESS (City, State, and ZIP Code) Monterey, CA 93943		10 SOURCE OF FUNDING NUMBERS			
		PROGRAM ELEMENT NO	PROJECT NO	TASK NO	WORK UNIT ACCESSION NO.
11. TITLE (Include Security Classification) EFFECTS OF CLIMATOLOGICAL AND TRANSIENT WIND FORCING ON EDDY GENERATION IN THE CALIFORNIA CURRENT SYSTEM					
12. PERSONAL AUTHOR(S) Robert W. Edson in conjunction with M.L. Batteen and C.S. Nelson					
13a TYPE OF REPORT Master's Thesis	13b TIME COVERED FROM _____ TO _____	14 DATE OF REPORT (Year, Month, Day) September, 1989	15 PAGE COUNT 155		
16 SUPPLEMENTARY NOTATION The views expressed in this thesis are those of the author and do not reflect the official policy or position of the Department of Defense or the U.S. Government.					
17 COSATI CODES			18 SUBJECT TERMS (Continue on reverse if necessary and identify by block number) Primitive equation model, eddies, jets, filaments, wind forcing, coastal jet and undercurrent, wind stress curl, California Current System		
FIELD	GROUP	SUB-GROUP			
19 ABSTRACT (Continue on reverse if necessary and identify by block number) → A high-resolution, multi-level, primitive equation ocean model is used to examine the response to transient and climatological wind forcing of an idealized, flat-bottomed oceanic regime on a beta-plane, along an eastern boundary. An annually periodic wind forcing function with zonal variability is used as transient forcing in several experiments using both winter and summer initializations. When the curl component of the forcing is stronger than the stress, as in the wintertime, a surface poleward flow develops in the nearshore region with an equatorward flow offshore. When wind stress dominates the forcing, as in the summertime, a coastal jet develops with an undercurrent. In other experiments, spatially varying one degree and two tenths degree steady wind stress data are used as climatological forcing. The one degree climatological wind stress data has positive curl at the coast which causes a poleward surface flow to develop. When two tenths degree wind stress data is used in the nearshore area, both,					
20 DISTRIBUTION AVAILABILITY OF ABSTRACT <input checked="" type="checkbox"/> UNCLASSIFIED/UNLIMITED <input type="checkbox"/> SAME AS RPT <input type="checkbox"/> DTIC USERS			21 ABSTRACT SECURITY CLASSIFICATION Unclassified		
22a NAME OF RESPONSIBLE INDIVIDUAL M.L. Batteen		22b TELEPHONE (Include Area Code) (408) 646-2768	22c OFFICE SYMBOL 54Ss		

DD Form 1473, JUN 86

Previous editions are obsolete

S/N 0102-LF-014-6603

SECURITY CLASSIFICATION OF THIS PAGE

Unclassified

Unclassified

SECURITY CLASSIFICATION OF THIS PAGE

Block 19, Continued

positive and negative curl in the coastal region result in the formation of poleward and equatorward currents, respectively. As a result of convergence in the surface flow, eddies and a well defined cold filament develop. These results show that the interaction of diverse coastal currents driven by an equally diverse wind field can play an important role in the production of cold filaments and eddies. *Theses (2)*

Approved for public release; distribution is unlimited

The Effects of Climatological and Transient
Wind Forcing on Eddy Generation
in the California Current System

by

Robert W. Edson
Lieutenant, United States Navy
B.S., George Mason University

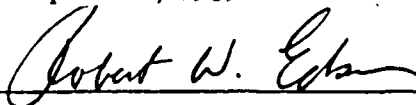
Submitted in partial fulfillment
of the requirements for the degree of

MASTER OF SCIENCE IN METEOROLOGY AND OCEANOGRAPHY

from the

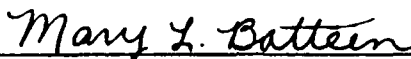
NAVAL POSTGRADUATE SCHOOL
September, 1989

Author:

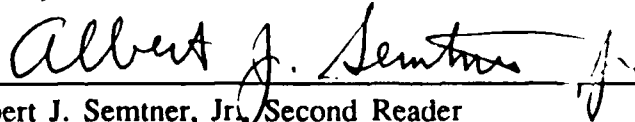


Robert W. Edson

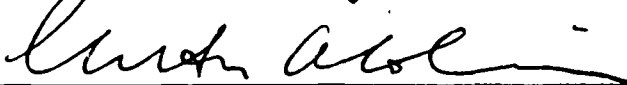
Approved by:



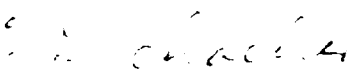
Mary L. Batteen, Thesis Advisor



Albert J. Semtner, Jr., Second Reader



Curtis A. Collins, Chairman
Department of Oceanography



Gordon E. Schacher,
Dean of Science and Engineering

ABSTRACT

A high-resolution, multi-level, primitive equation ocean model is used to examine the response to transient and climatological wind forcing of an idealized, flat-bottomed oceanic regime on a β -plane, along an eastern boundary. An annually periodic wind forcing function with zonal variability is used as transient forcing in several experiments using both winter and summer initializations. When the curl component of the forcing is stronger than the stress, as in the wintertime, a surface poleward flow develops in the nearshore region with an equatorward flow offshore. When wind stress dominates the forcing, as in the summertime, a coastal jet develops with an undercurrent. In other experiments, spatially varying one degree and two tenths degree steady wind stress data are used as the climatological forcing. The one degree climatological wind stress data has positive curl at the coast which causes a poleward surface flow to develop. When two tenths degree wind stress data is used in the nearshore area, both positive and negative curl in the coastal region result in the formation of poleward and equatorward currents, respectively. As a result of convergence in the surface flow, eddies and a well defined cold filament develop. These results show that the interaction of diverse coastal currents driven by an equally diverse wind field can play an important role in the production of cold filaments and eddies.

ACKNOWLEDGEMENTS

I wish to thank my thesis advisor, Dr. Mary L. Batteen, for her guidance and help throughout my thesis research and writing. I would especially like to thank her for her seemingly endless patience with my seemingly endless procrastination. The help and data supplied by Craig S. Nelson is also gratefully acknowledged.

I would also like to thank my favorite coach, Arlene Bird, for her much appreciated assistance in programming and for her understanding when I needed someone to complain to. Finally, a special thanks to Chuck and Bernice without whom finishing this thesis would not have been nearly as much fun.



Accession For	
NTIS GRA&I	<input checked="" type="checkbox"/>
DTIC TAB	<input type="checkbox"/>
Unannounced	<input type="checkbox"/>
Justification	
By _____	
Distribution/	
Availability Codes	
Dist	Avail and/or Special
A-1	

TABLE OF CONTENTS

I. INTRODUCTION	1
A. BACKGROUND ON THE CALIFORNIA CURRENT SYSTEM ...	1
1. Regional Description	1
2. Climatological Winds	3
3. Numerical Model Studies	5
B. OBJECTIVES FOR THESIS	8
II. NUMERICAL MODEL OF THE CALIFORNIA CURRENT SYSTEM	17
A. MODEL DESCRIPTION	17
1. Model Equations	17
2. Model Domain and Resolution	20
3. Finite Difference Scheme	21
4. Heat and Momentum Diffusion	22
5. Surface Thermal Forcing	22
6. Boundary Conditions	23
7. Initial Conditions	24
B. SPECIFIC EXPERIMENTAL CONDITIONS	24
1. Transient Wind Forcing (Exps. 1-2)	24
2. One Degree Climatological Wind Forcing (Exps. 3-5)	27
3. Two Tenths Degree Climatological Wind Forcing (Exp. 6)	29

III. EXPERIMENT RESULTS	39
A. TRANSIENT WIND FORCING	39
1. Experiment 1	39
2. Experiment 2	41
B. ONE DEGREE CLIMATOLOGICAL WIND FORCING	44
1. Experiment 3	44
2. Experiment 4	47
3. Experiment 5	49
C. TWO TENTHS DEGREE CLIMATOLOGICAL WIND FORCING ..	53
1. Experiment 6	53
D. STABILITY ANALYSIS	58
1. Experiment 5	59
2. Experiment 6	60
IV. COMPARISON OF MODEL RESULTS WITH OBSERVATIONS	119
V. SUMMARY AND RECOMMENDATIONS	126
A. SUMMARY	126
B. RECOMMENDATIONS	129
LIST OF REFERENCES	131
INITIAL DISTRIBUTION LIST	137

LIST OF TABLES

Table I	Constants used in the model.	21
Table II	Summary of experimental conditions	32
Table III	Instantaneous comparison of model experiments with model results of Batteen <i>et al.</i> (1989) and observations of the CCS	123

LIST OF FIGURES

Figure 1.1	Climatological wind stress for June (from Nelson, 1977).	11
Figure 1.2	Climatological wind stress for July (from Nelson, 1977).	12
Figure 1.3	Climatological wind stress for August (from Nelson, 1977). . .	13
Figure 1.4	Climatological wind stress curl for June (from Nelson, 1977). .	14
Figure 1.5	Climatological wind stress curl for July (from Nelson, 1977). .	15
Figure 1.6	Climatological wind stress curl for August (from Nelson, 1977).	16
Figure 2.1	Study domain	33
Figure 2.2	Wind stress versus offshore distance for December.	34
Figure 2.3	Wind stress versus offshore distance for June.	35
Figure 2.4	Wind stress isopleths for one degree resolution climatological data over the model domain.	36
Figure 2.5	Sampling domain for the two tenths degree climatological wind stress forcing.	37
Figure 2.6	Wind stress isopleths for one degree / two tenths degree resolution climatological data over the model domain.	38
Figure 3.1	Surface isopleths of (a) zonal (u) velocity (cm s^{-1}), (b) meridional (v) velocity (cm s^{-1}), and (c) temperature ($^{\circ}\text{C}$) for Experiment 1 at day 60.	64
Figure 3.2	Surface isopleths of (a) zonal (u) velocity (cm s^{-1}), (b) meridional (v) velocity (cm s^{-1}), and (c) temperature ($^{\circ}\text{C}$) for Experiment 2 at day 5.	65
Figure 3.3	Vertical cross-shore section of meridional (v) velocity (cm s^{-1}) for Experiment 2 at day 10.	66
Figure 3.4	Vertical cross-shore section of temperature ($^{\circ}\text{C}$) for Experiment 2 at day 10.	67

Figure 3.5	Surface isopleths of (a) zonal (u) velocity (cm s^{-1}), (b) meridional (v) velocity (cm s^{-1}), (c) temperature ($^{\circ}\text{C}$), and (d) dynamic height (cm) relative to 2400 m for Experiment 2 at day 25.	68
Figure 3.6	Vertical cross-shore section of meridional (v) velocity (cm s^{-1}) for Experiment 2 at day 30.	69
Figure 3.7	Surface isopleths of (a) zonal (u) velocity (cm s^{-1}), (b) meridional (v) velocity (cm s^{-1}), (c) temperature ($^{\circ}\text{C}$), and (d) dynamic height (cm) relative to 2400 m for Experiment 2 at day 80.	70
Figure 3.8	Surface isopleths of (a) zonal (u) velocity (cm s^{-1}), (b) meridional (v) velocity (cm s^{-1}), (c) temperature ($^{\circ}\text{C}$), and (d) dynamic height (cm) relative to 2400 m for Experiment 2 at day 120.	71
Figure 3.9	Vertical cross-shore section of temperature ($^{\circ}\text{C}$) for Experiment 2 at day 120.	72
Figure 3.10	Vertical cross-shore section of meridional (v) velocity (cm s^{-1}) for Experiment 2 at day 120.	73
Figure 3.11	Surface isopleths of (a) zonal (u) velocity (cm s^{-1}), (b) meridional (v) velocity (cm s^{-1}), (c) temperature ($^{\circ}\text{C}$), and (d) dynamic height (cm) relative to 2400 m for Experiment 3 at day 40.	74
Figure 3.12	Vertical cross-shore section of meridional (v) velocity (cm s^{-1}) for Experiment 3 at day 40.	75
Figure 3.13	Vertical cross-shore section of temperature ($^{\circ}\text{C}$) for Experiment 3 at day 40.	76
Figure 3.14	Surface isopleths of zonal (u) velocity (cm s^{-1}) for Experiment 3 at (a) day 40, (b) day 50, (c) day 70 and (d) day 80.	77
Figure 3.15	Surface isopleths of (a) zonal (u) velocity (cm s^{-1}), (b) meridional (v) velocity (cm s^{-1}), (c) temperature ($^{\circ}\text{C}$), and (d) dynamic height (cm) relative to 2400 m for Experiment 4 at day 40.	78
Figure 3.16	Vertical cross-shore section of meridional (v) velocity (cm s^{-1}) for Experiment 4 at day 40.	79
Figure 3.17	Vertical cross-shore section of temperature ($^{\circ}\text{C}$) for Experiment 4 at day 40.	80

Figure 3.18	Surface isopleths of (a) zonal (u) velocity (cm s^{-1}), (b) meridional (v) velocity (cm s^{-1}), (c) temperature ($^{\circ}\text{C}$), and (d) dynamic height (cm) relative to 2400 m for Experiment 4 at day 85.	81
Figure 3.19	Surface isopleths of (a) zonal (u) velocity (cm s^{-1}), (b) meridional (v) velocity (cm s^{-1}), (c) temperature ($^{\circ}\text{C}$), and (d) dynamic height (cm) relative to 2400 m for Experiment 4 at day 110.	82
Figure 3.20	Vertical cross-shore section of meridional (v) velocity (cm s^{-1}) for Experiment 4 at day 110.	83
Figure 3.21	Surface current vectors for Experiment 4 at (a) day 40, and (b) day 110.	84
Figure 3.22	Surface isopleths of (a) zonal (u) velocity (cm s^{-1}), (b) meridional (v) velocity (cm s^{-1}), (c) temperature ($^{\circ}\text{C}$), and (d) dynamic height (cm) relative to 2400 m for Experiment 5 at day 10.	85
Figure 3.23	Vertical cross-shore section of meridional (v) velocity (cm s^{-1}) for Experiment 5 at day 10.	86
Figure 3.24	Vertical cross-shore section of temperature ($^{\circ}\text{C}$) for Experiment 5 at day 10.	87
Figure 3.25	Surface isopleths of (a) zonal (u) velocity (cm s^{-1}), (b) meridional (v) velocity (cm s^{-1}), (c) temperature ($^{\circ}\text{C}$), and (d) dynamic height (cm) relative to 2400 m for Experiment 5 at day 20.	88
Figure 3.26	Vertical cross-shore section of meridional (v) velocity (cm s^{-1}) for Experiment 5 at day 20.	89
Figure 3.27	Surface isopleths of (a) zonal (u) velocity (cm s^{-1}), (b) meridional (v) velocity (cm s^{-1}), (c) temperature ($^{\circ}\text{C}$), and (d) dynamic height (cm) relative to 2400 m for Experiment 5 at day 40.	90
Figure 3.28	Surface isopleths temperature ($^{\circ}\text{C}$) Experiment 5 at day 55. . .	91
Figure 3.29	Surface isopleths of (a) zonal (u) velocity (cm s^{-1}), (b) meridional (v) velocity (cm s^{-1}), (c) temperature ($^{\circ}\text{C}$), and (d) dynamic height (cm) relative to 2400 m for Experiment 5 at day 80.	92
Figure 3.30	Vertical cross-shore section of meridional (v) velocity (cm s^{-1}) for Experiment 5 at day 80.	93
Figure 3.31	Vertical cross-shore section of temperature ($^{\circ}\text{C}$) for Experiment 5 at day 80.	94

Figure 3.32	Surface isopleths of (a) zonal (u) velocity (cm s^{-1}), (b) meridional (v) velocity (cm s^{-1}), (c) temperature ($^{\circ}\text{C}$), and (d) dynamic height (cm) relative to 2400 m for Experiment 5 at day 110.	95
Figure 3.33	Vertical cross-shore section of temperature ($^{\circ}\text{C}$) for Experiment 5 at day 110.	96
Figure 3.34	Vertical cross-shore section of meridional (v) velocity (cm s^{-1}) for Experiment 5 at day 110.	97
Figure 3.35	Surface current vectors for Experiment 5 at (a) day 20, (b) day 40, (c) day 80, and (d) day 110.	98
Figure 3.36	Surface isopleths of (a) zonal (u) velocity (cm s^{-1}), (b) meridional (v) velocity (cm s^{-1}), (c) temperature ($^{\circ}\text{C}$), and (d) dynamic height (cm) relative to 2400 m for Experiment 6 at day 5.	99
Figure 3.37	Surface isopleths of (a) zonal (u) velocity (cm s^{-1}), (b) meridional (v) velocity (cm s^{-1}), (c) temperature ($^{\circ}\text{C}$), and (d) dynamic height (cm) relative to 2400 m for Experiment 6 at day 10.	100
Figure 3.38	Vertical cross-shore section of meridional (v) velocity (cm s^{-1}) for Experiment 6 at day 10.	101
Figure 3.39	Vertical cross-shore section of temperature ($^{\circ}\text{C}$) for Experiment 6 at day 10.	102
Figure 3.40	Vertical cross-shore section of meridional (v) velocity (cm s^{-1}) for Experiment 6 at day 10.	103
Figure 3.41	Vertical cross-shore section of meridional (v) velocity (cm s^{-1}) for Experiment 6 at day 20.	104
Figure 3.42	Vertical cross-shore section of meridional (v) velocity (cm s^{-1}) for Experiment 6 at day 20.	105
Figure 3.43	Surface isopleths of (a) zonal (u) velocity (cm s^{-1}), (b) meridional (v) velocity (cm s^{-1}), (c) temperature ($^{\circ}\text{C}$), and (d) dynamic height (cm) relative to 2400 m for Experiment 6 at day 25.	106
Figure 3.44	Surface isopleths of (a) zonal (u) velocity (cm s^{-1}), (b) meridional (v) velocity (cm s^{-1}), (c) temperature ($^{\circ}\text{C}$), and (d) dynamic height (cm) relative to 2400 m for Experiment 6 at day 40.	107

Figure 3.45	Vertical cross-shore section of meridional (v) velocity (cm s^{-1}) for Experiment 6 at day 40.	108
Figure 3.46	Vertical cross-shore section of temperature ($^{\circ}\text{C}$) for Experiment 6 at day 40.	109
Figure 3.47	Surface isopleths of (a) zonal (u) velocity (cm s^{-1}), (b) meridional (v) velocity (cm s^{-1}), (c) temperature ($^{\circ}\text{C}$), and (d) dynamic height (cm) relative to 2400 m for Experiment 6 at day 80.	110
Figure 3.48	Surface isopleths of (a) zonal (u) velocity (cm s^{-1}), (b) meridional (v) velocity (cm s^{-1}), (c) temperature ($^{\circ}\text{C}$), and (d) dynamic height (cm) relative to 2400 m for Experiment 6 at day 100.	111
Figure 3.49	Surface isopleths of (a) zonal (u) velocity (cm s^{-1}), (b) meridional (v) velocity (cm s^{-1}), (c) temperature ($^{\circ}\text{C}$), and (d) dynamic height (cm) relative to 2400 m for Experiment 6 at day 120.	112
Figure 3.50	Vertical cross-section of the cross-stream derivative of potential vorticity multiplied by the grid size ($^{\circ}\text{C m}^{-1} \text{s}^{-1}$) scaled by 10^6 for the time-averaged days 90-99 of Experiment 5.	113
Figure 3.51	Vertical cross-section of the cross-stream derivative of potential vorticity multiplied by the grid size ($^{\circ}\text{C m}^{-1} \text{s}^{-1}$) scaled by 10^6 for the time-averaged days 1-12 of Experiment 6.	114
Figure 3.52	Kinetic energy (ergs cm^{-3}) time series for Experiment 6.	115
Figure 3.53	Basin-averaged energy diagram for days 1 to 12 of Experiment 6.	116
Figure 3.54	Vertical cross-section of the cross-stream derivative of potential vorticity multiplied by the grid size ($^{\circ}\text{C m}^{-1} \text{s}^{-1}$) scaled by 10^6 for the time-averaged days 100-120 of Experiment 6.	117
Figure 3.55	Basin-averaged energy diagram for days 100 to 120 of Experiment 6.	118
Figure 4.1	Current vector time series for a station (a) north of Cape Mendocino and a station (b) south of Cape Mendocino.	124
Figure 4.2	Pilot moored instrument station locations during NCCCS program.	125

I. INTRODUCTION

A. BACKGROUND ON THE CALIFORNIA CURRENT SYSTEM

1. Regional Description

The California Current System (CCS) is a complex combination of several ocean currents. Dominating this system is the California Current (CC), an eastern boundary current extending approximately 1000 kilometers offshore with a southeastward flow (Sverdrup *et al.*, 1942; Chelton, 1984). The CC represents the eastern limb of the North Pacific gyre (Lynn and Simpson, 1987), and is driven by the large-scale North Pacific High (Huyer, 1983). Typically extending to only 300 meters, this current is characterized by low temperature, low salinity and high dissolved oxygen (Lynn and Simpson, 1987). The core of the CC is found approximately 100-200 km offshore (Chelton, 1984). Average current speeds are less than 25 cm s^{-1} (Reid and Schwartzlose, 1962; Bernstein *et al.*, 1977), but daily average speeds as high as 50 cm s^{-1} have been recorded (Davis, 1985).

From the shoreline to roughly 100 km off the coast, there is evidence of a separate current (Chelton, 1984; Hickey, 1979). This current has a seasonal variation in flow direction which serves to demarcate it from the broader CC (Chelton, 1984; Hickey, 1979). This nearshore surface current has been observed to have equatorward flow from February through September extending ~ 125 km offshore (Hickey, 1979). From November to February, this nearshore flow reverses direction and flows

northward in the area from Pt. Conception to Cape Mendocino (Hickey, 1979). During the winter season this flow is called the Davidson Current (Chelton, 1984; Hickey, 1979). This simplistic interpretation of the nearshore current is deceptive. The nearshore mean flow between Pt. Conception and Pt. Sur has been observed to be poleward during the summer, while the flow further north to Cape Mendocino has been documented as flowing both poleward and equatorward during the same summer months (Chelton *et al.*, 1988; Freitag and Halpern, 1981). These observations further highlight the variable nature of this region.

The California Undercurrent (CU) makes up the third major part of the CCS. The CU is found over the continental shelf with a northward flow 20 to 70 km wide (Hickey, 1979; Reid 1962). It has a core velocity greater than 15 cm s^{-1} with some measurements as high as 40 cm s^{-1} (Hickey, 1979; Reid 1962). With a vertical extent of approximately 300 m, the core is usually located 200-250 m below the surface (Wickham *et al.*, 1987; Hickey, 1979). Reed and Halpern (1976) found the undercurrent off Washington to have a vertical extent in excess of 500 m. They also felt that the undercurrent they observed was an extension of the CU seen further south, making the CU have a latitudinal extent of over 2200 km.

The fourth constituent of the CCS is the Southern California Countercurrent (SCC). This current is comprised of the poleward flow found in the California Bight, south of Pt. Conception (Hickey, 1979). The SCC has a semi-permanent eddy-like circulation which seems to be strongly affected by the topography of the region (Lynn and Simpson, 1987). While this current is an important part of the CCS, it does not enter into the area modeled and as such will not be considered further.

The California Current System is not a quiescent, stable system of currents with a well defined, unchanging structure. Rather, the flow fluctuates greatly in both time and space (Chelton, 1984). Irregularities in the flow were noted as early as 1950 (Reid, 1988). There exist mesoscale meanders, eddies, filaments and jet-like surface currents which are superimposed on the large scale flow (Bernstein *et al.*, 1977; Chelton, 1984). Eddy-like features with wavelengths of 100-150 km (Freitag and Halpern, 1981; Bernstein *et al.*, 1977) have been documented and are prevalent in most current satellite observations (e.g., Ikeda and Emery, 1984; Ikeda *et al.*, 1984a,b; Kelly, 1985). The current itself may take the form of a meandering jet, with wavelengths of 300 to 500 km (Bernstein *et al.*, 1977). These meanders have associated with them cold filaments, exhibiting a 1 to 3 °C temperature change across their boundaries (Bernstein *et al.*, 1977). The filaments can extend to 100 m, with a width of 30 km and peak speeds of up to 80 cm s⁻¹ (Kosro and Huyer, 1986). The combination of these features leads to a new conceptualization of the CCS as a system of currents with filamented jets and synoptic-mesoscale eddies modifying the mean flow (Mooers and Robinson, 1984).

2. Climatological Winds

Interaction between the North Pacific subtropical high and the southwest United States thermal low, two relatively stationary systems in the summer, establishes the summer wind patterns seen in the CCS (Nelson, 1977; Halliwell and Allen, 1987). The wind regime is further complicated by the interaction of these two systems with propagating atmospheric disturbances (Halliwell and Allen, 1987) and other atmospheric mesoscale phenomena (Huyer, 1983). Within 100-200 km of the shore, the winds are

additionally affected by coastal atmospheric boundary layer processes, resulting in measured wind fluctuations strongly polarized in the alongshore direction (Halliwell and Allen, 1987).

The climatological wind stress for the summer months is favorable for upwelling with a mean alongshore equatorward component (Nelson, 1977; Halliwell and Allen, 1987; Wickham *et al.*, 1987). An alongshore wind stress time series compiled over nine years by Strub *et al.* (1987) clearly depicts the dominance of equatorward wind stress during the summer. Halpern (1976) found similar conditions of southward wind stress during July and August in a study conducted off the coast of Oregon. The long term means for the surface wind stress for June, July, and August are shown in Figures 1.1, 1.2, and 1.3, respectively. It is important to note the maximum core of the wind stress (denoted by shading in the figures) which extends along the California coast for 1000 km. The wind stress values reach a maximum off Cape Mendocino in June and July (Nelson, 1977), with values greater than $1.5 \text{ dynes cm}^{-2}$. This maximum is originally seen in March, south of Point Conception, and it intensifies and shifts northward over the year. Also seen in these figures is that the alongshore stress component is larger than the cross-shore component. The climatological winter wind stress regime is much weaker (typically less than $0.5 \text{ dynes cm}^{-2}$) but is still equatorward in the region from Cape Mendocino to Baja, California (Nelson, 1977). Finally, Nelson (1977) found that the wind stress velocities can vary a large amount both spatially and temporally, making any analytical representation of the wind stress field extremely difficult.

There is positive wind stress curl at the coast during all months of the year with the strongest curl occurring from May to September (Nelson, 1977; Halpern, 1976). The wind stress curl plots for the summer months are shown in Figures 1.4 through 1.6. Bakun (1987) found that anticyclonic wind stress curl dominated the offshore region giving convergent Ekman transport, Ekman pumping downward from the surface and equatorward Sverdrup flow. Conversely, at the coast he found cyclonic wind stress curl, i.e., divergent surface Ekman transport, upward Ekman pumping, oceanic upwelling, and poleward Sverdrup flow. A zero wind stress curl line occurs parallel to the coast approximately 200-300 km offshore in the spring and summer upwelling seasons coincident with the offshore wind stress maximum (Nelson, 1977; Chelton, 1984).

The importance of the wind stress and wind stress curl in the current dynamics and upwelling of the CCS is well documented (e.g., Huyer, 1983; Nelson, 1977; Chelton, 1984; Hickey, 1979; Kelly, 1985). Wind stress data has been correlated with satellite infrared imagery of eddies and filaments, illustrating the possible importance of wind stress in these mesoscale processes (Kelly, 1985; Wickham *et al.*, 1987). However, the roles of the wind stress and wind stress curl in eddy and jet generation is not clearly understood. It is this phenomena which is the thrust of this research.

3. Numerical Model Studies

The complexity of the CCS has led to tremendous diversity in numerical model studies of this region over the last two decades. This section makes no attempt to review all past studies, but rather will concentrate on those modeling experiments

with direct application to this research. More extensive reviews are included in Allen (1980), Chelton (1984), and O'Brien *et al.* (1977). The primary thrust of this thesis is wind forcing of the CCS. Within this area, however, classification can be made as to whether the wind forcing is steady or transient and whether the forcing contains a curl component or is curl-free. Further divisions are possible, but will be avoided here for simplicity.

Initial studies primarily concentrated on the application of steady wind stress forcing on a modelled current system. Chief amongst these studies was Pedlosky (1974). He found that steady equatorward wind stress drives a baroclinic equatorward jet, and that an undercurrent is not necessarily formed. If positive wind stress curl is introduced at the coast, a barotropic poleward coastal flow develops. If the stress is strong enough at the coast, the baroclinic jet may override the poleward flow and an equatorward jet may result in addition to an undercurrent.

One of the first transient wind forcing numerical model experiments was done by Philander and Yoon (1982). Their periodic forcing was meridionally restricted but otherwise constant in the cross-shore and alongshore direction. The particular response of the model depended on the frequency of the wind forcing. At low frequencies the response spreads offshore, while at high frequencies the response is coastally trapped. It should be emphasized that there was no positive wind stress curl at the coast in Philander and Yoon's study.

The response of reduced-gravity models to realistic coastal winds was investigated by Carton (1984) and Carton and Philander (1984). They utilized temporally varying one degree resolution geostrophic winds to force their model and

found a time dependency in their results. At periods of less than 50 days the coastal current was trapped within a Rossby radius of deformation of the coast and the alongshore flow was well correlated with the alongshore stress. At periods longer than 50 days, wind stress curl became important, and at 100 days the alongshore currents began to weaken and disperse, becoming a series of alternating jets.

The remaining three studies are most directly applicable to the experimentation of this thesis. McCreary *et al.* (1987) did a series of experiments utilizing a linear model with both transient and steady wind forcing. The wind forcing included stress functions both with and without curl. Steady, equatorward, curl-free wind forcing resulted in an equatorward surface jet and an undercurrent. If steady, positive wind curl was used to force the model, a broad, deep, poleward surface current developed near the coast. In addition to this poleward current, the positive curl also forced equatorward flow offshore. Similar results were obtained from the periodic wind forcing. An additional experiment was done by McCreary *et al.* in which an idealized representation of the wind field was varied over an annual cycle to force the model. This idealized forcing included both a wind stress and wind stress curl component. In this experiment, the curl accounted for both the Davidson current and the equatorward flow offshore. Only during those times in the forcing cycle when stress was strong compared to the curl component was the equatorward jet and undercurrent seen. In all of these experiments no eddies or filaments were developed.

Tielking (1988) extended this work by conducting numerical simulations utilizing a full primitive equation model. His forcing was derived from meridionally averaged summer climatological data for the region of central California. The forcing

varied only in the cross-shore direction, had a positive curl at the coast and was steady throughout the experiment. Tielking obtained results similar to those of McCreary *et al.*, i.e., strong broad poleward flow at the coast, equatorward flow offshore, no undercurrent, and no eddies or filaments.

The final study was done by Batteen *et al.* (1989). Again a primitive equation model was used and the forcing took two forms, steady forcing constant throughout the domain and forcing which varied meridionally. The constant stress forcing resulted in an equatorward jet and an undercurrent. Additionally, the shear between the jet and undercurrent led to instability and the production of eddies in the coastal region. Similar results were seen when the model was forced by wind stress which varied in y only. In neither case was there any curl at the coast in the cross-shore direction.

It appears from these studies that equatorward wind stress is dominant in forcing the coastal jet and undercurrent, and further, is instrumental in the instability processes which lead to eddy production in the CCS. Conversely, positive wind stress curl at the coast develops poleward surface flow with no eddies or filaments. Interaction of these two components can lead to a mixed current structure at the coast, but eddies and filaments not necessarily develop. Finally, there seems to be a time scale to the relative importance of the stress and curl components.

B. OBJECTIVES FOR THESIS

The preceding two sections highlight a problem in the study of upwelling off the California coast. Clearly, the prevailing surface wind pattern during the summer upwelling season is one of strong equatorward wind stress, oriented predominantly in

the alongshore direction. Additionally, there is strong positive climatological wind stress curl at the coast during this same season. It is these two characteristics, alongshore equatorward stress and positive wind stress curl at the coast, that are dominant during the summer. However, when numerical studies are conducted to study the contributions of the wind stress and wind stress curl to the mesoscale processes of the region, conflicting results are found. When wind stress alone is utilized as a forcing mechanism, an equatorward jet and undercurrent are seen and eddies result. When wind stress curl is applied, a poleward surface flow is generated at the coast and no eddies are formed. Simply put, what is seen in model results does not agree with what is seen observationally.

Two logical paths arise at this stage towards the further study and resolution of the aforementioned paradox. First, it is possible that transient forcing is required to produce more realistic results. McCreary *et al.* (1987) applied a transient wind stress forcing function to CCS numerical simulations, but utilized a linear model in his studies. A first objective of this thesis research is to apply an annually periodic wind forcing function, with both a stress and curl component, to a fully nonlinear primitive equation numerical model of the CCS and study the resultant mesoscale events.

The second possibility for continued research lies in the area of the exact formulation of the wind stress forcing itself. Most studies to date have utilized forcing which was either constant throughout the domain or which varied in only one direction. Possibly it is not the relative weight of stress versus curl that is important in forcing instability, but rather full two dimensional variability in the forcing field. With this in mind, a second objective is to study the effects of climatological winds varying in

the cross-shore and the alongshore direction on eddy formation in the CCS. A final objective will be to apply various energy analysis techniques to the above studies to characterize the energetics of the CCS under the applied conditions of these numerical model experiments.

The thesis is organized as follows. Section II discusses the numerical model used in the research as well as the conditions unique to each experiment. Experimental results with the associated energy analyses are presented in Section III. A comparison with observations is made in Section VI, and a summary and recommendations are presented in Section V.

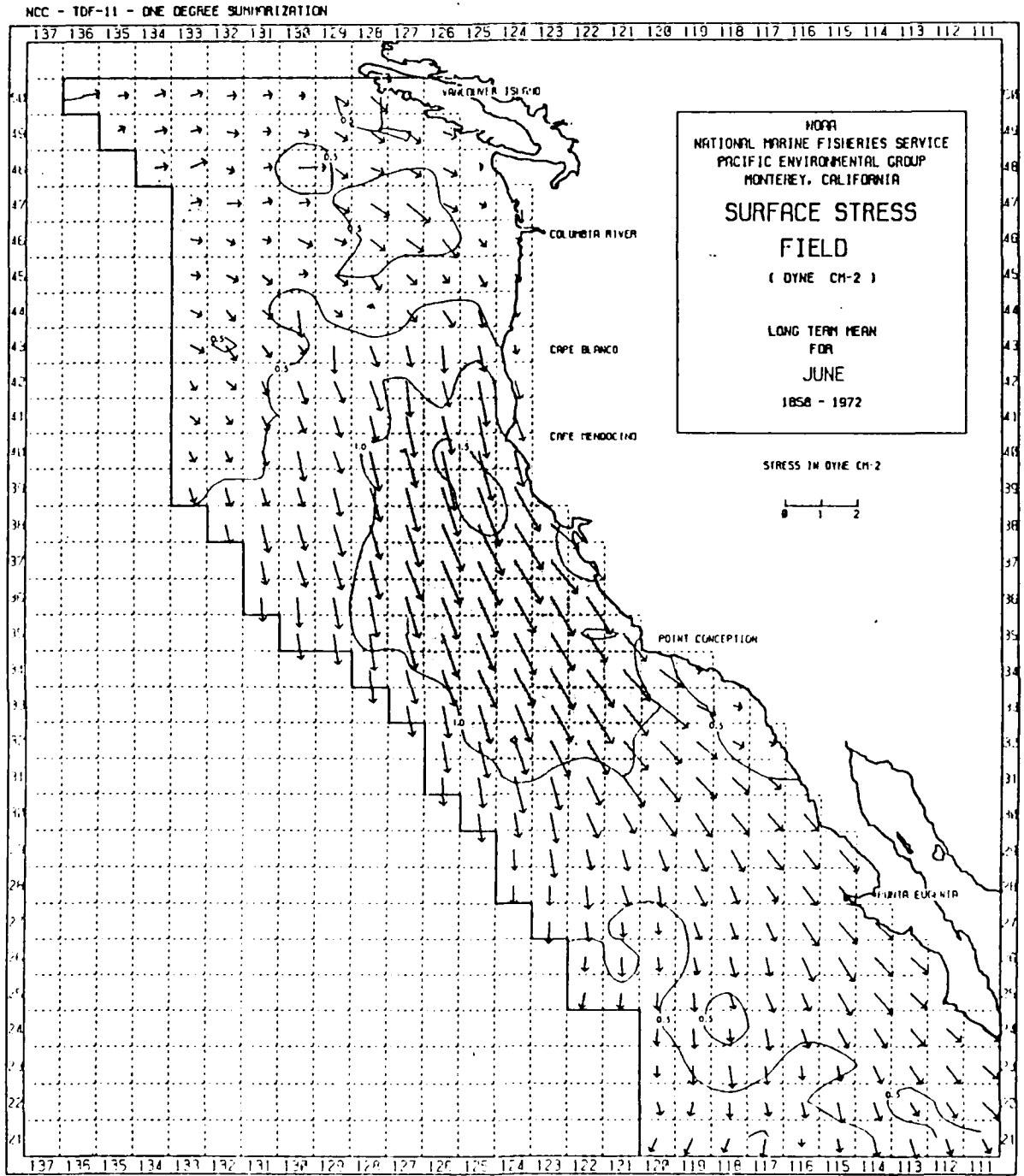


Figure 1.1 Climatological wind stress for June (from Nelson, 1977).

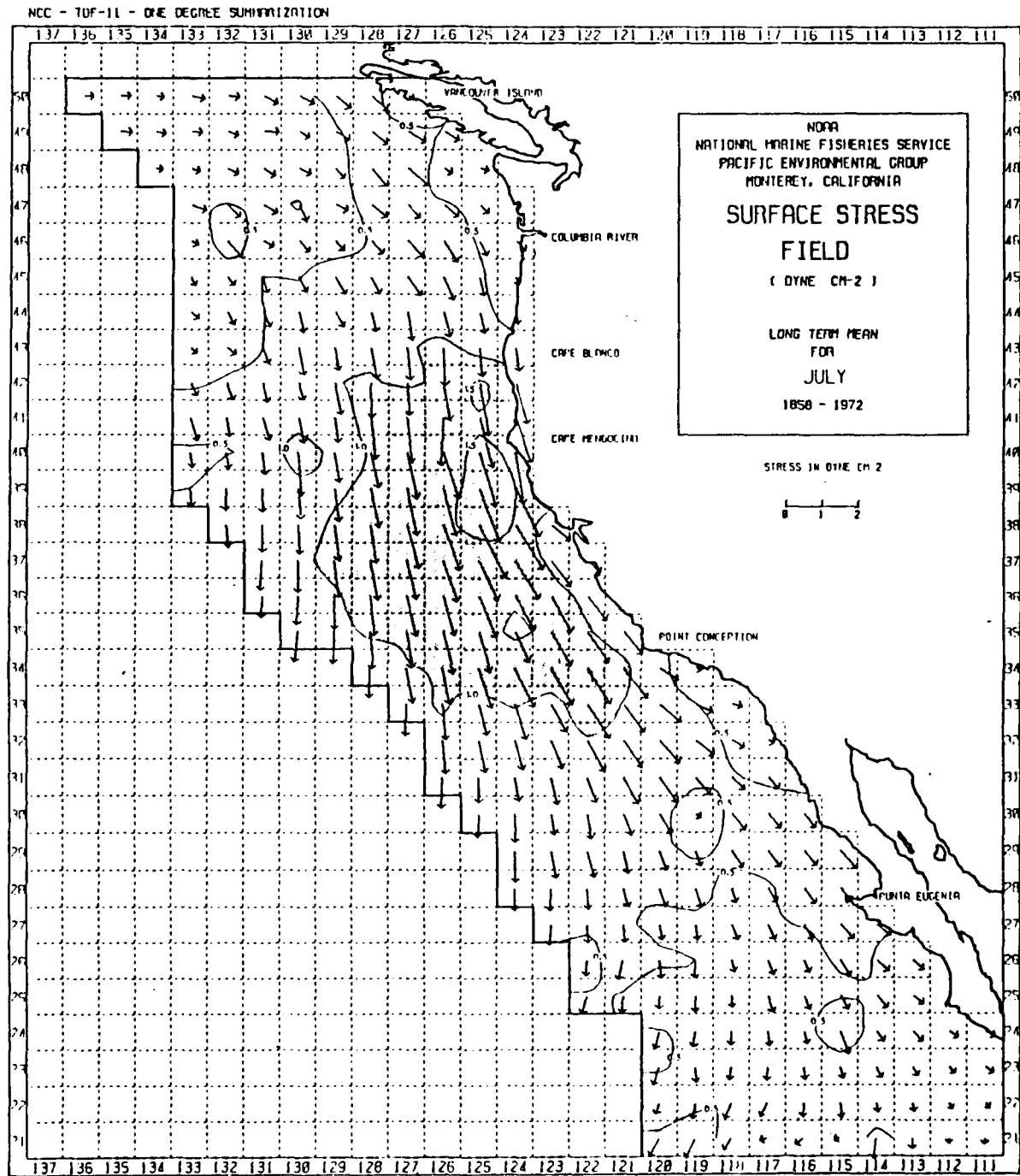


Figure 1.2 Climatological wind stress for July (from Nelson, 1977).

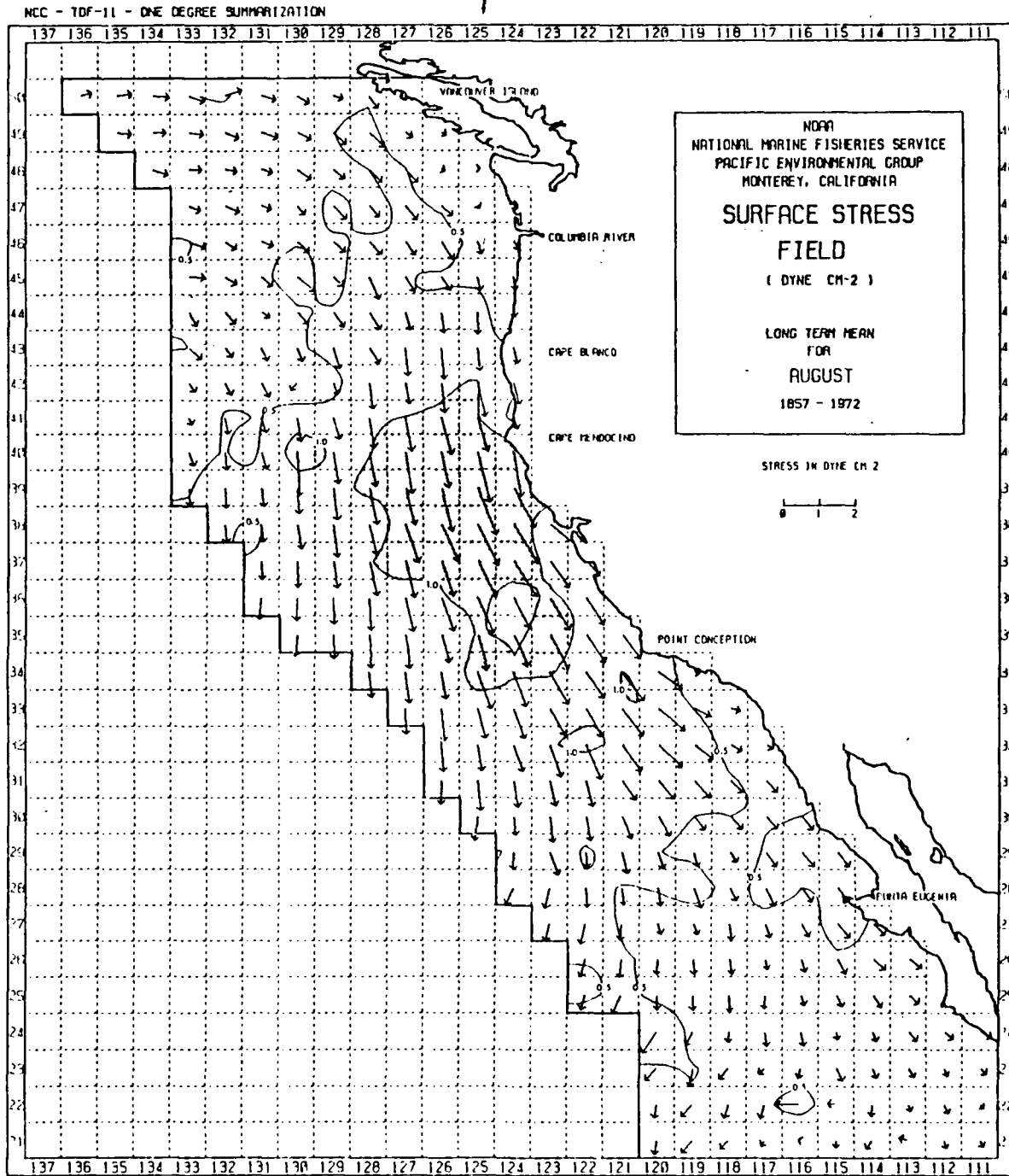


Figure 1.3 Climatological wind stress for August (from Nelson, 1977).

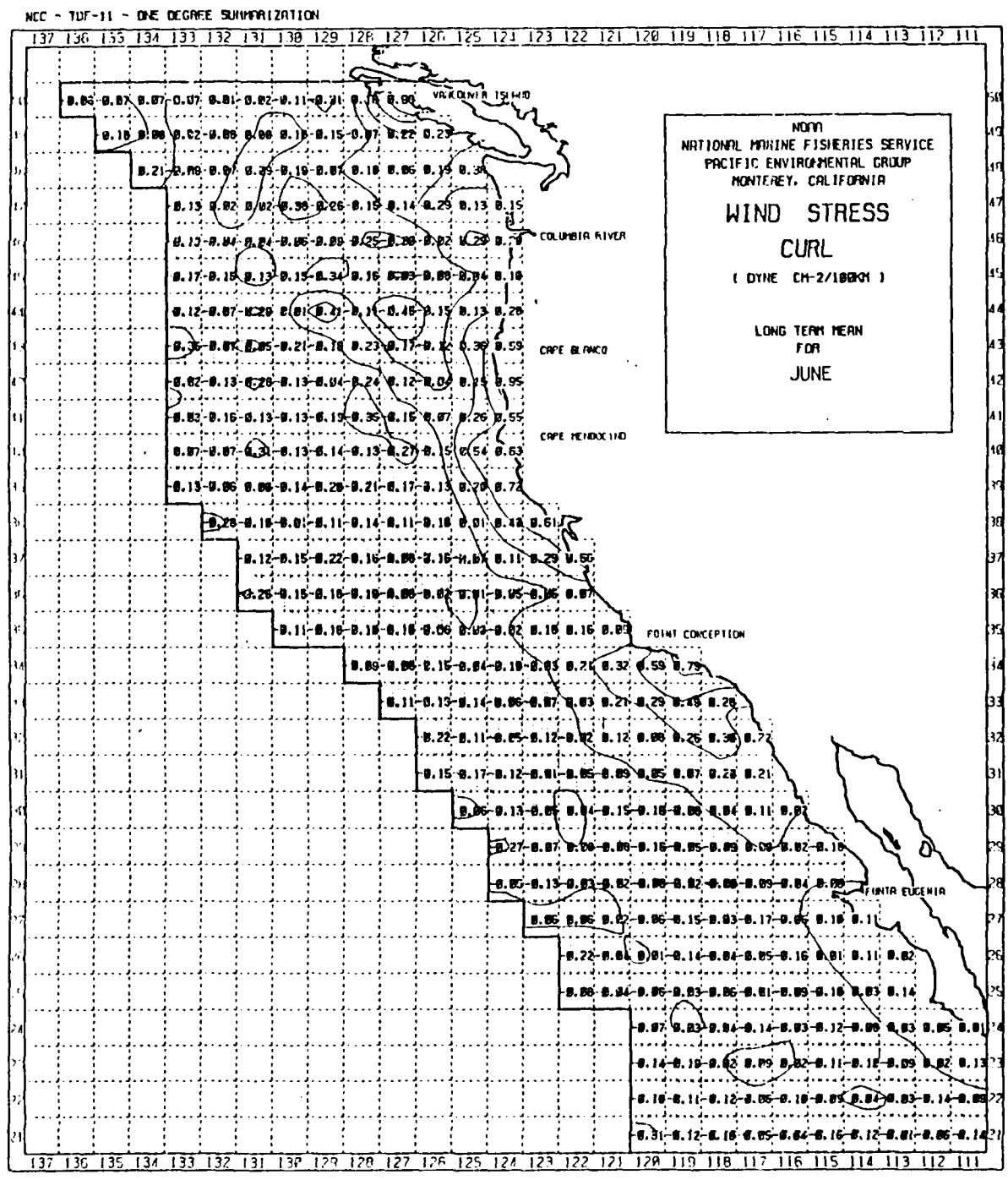


Figure 1.4 Climatological wind stress curl for June (from Nelson, 1977).

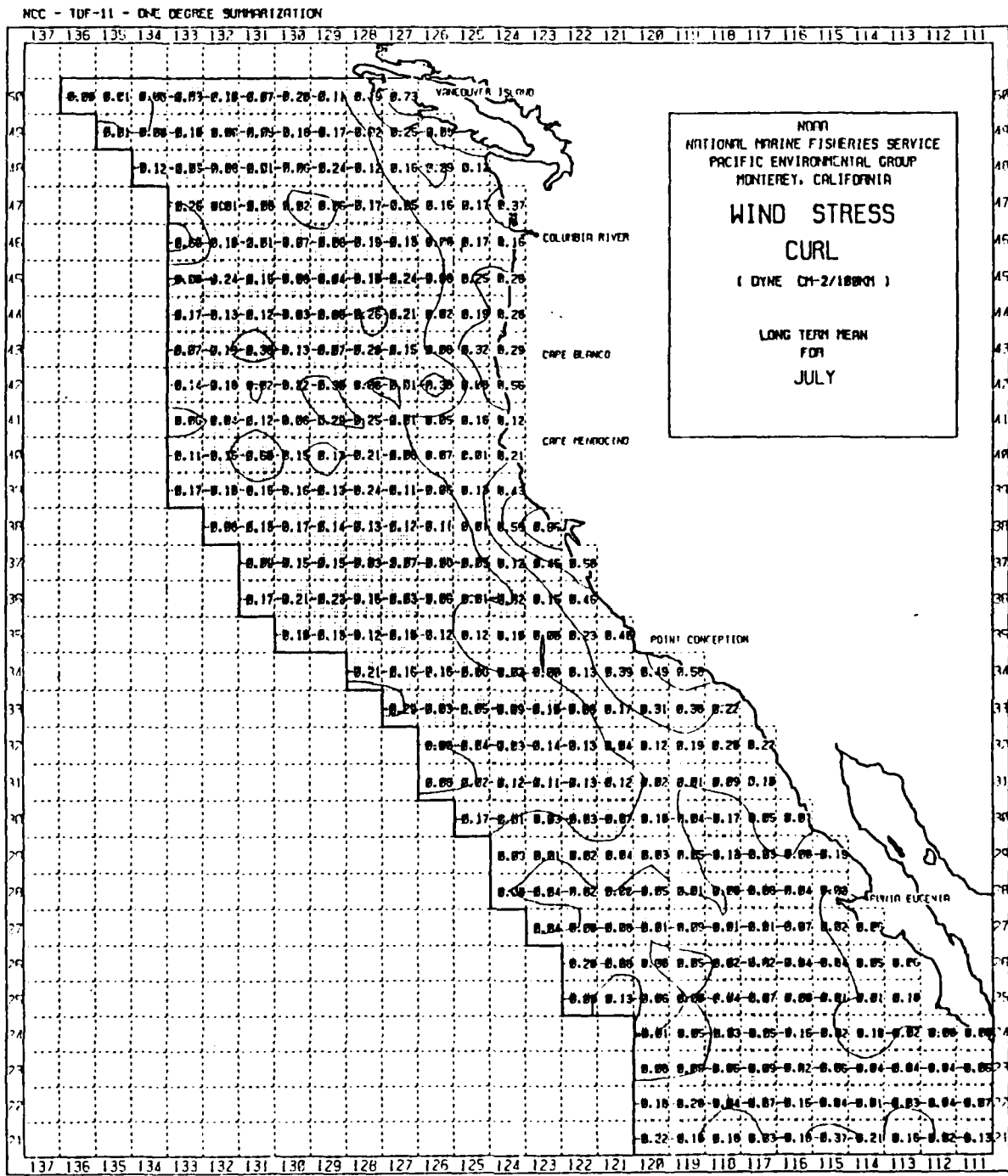


Figure 1.5 Climatological wind stress curl for July (from Nelson, 1977).

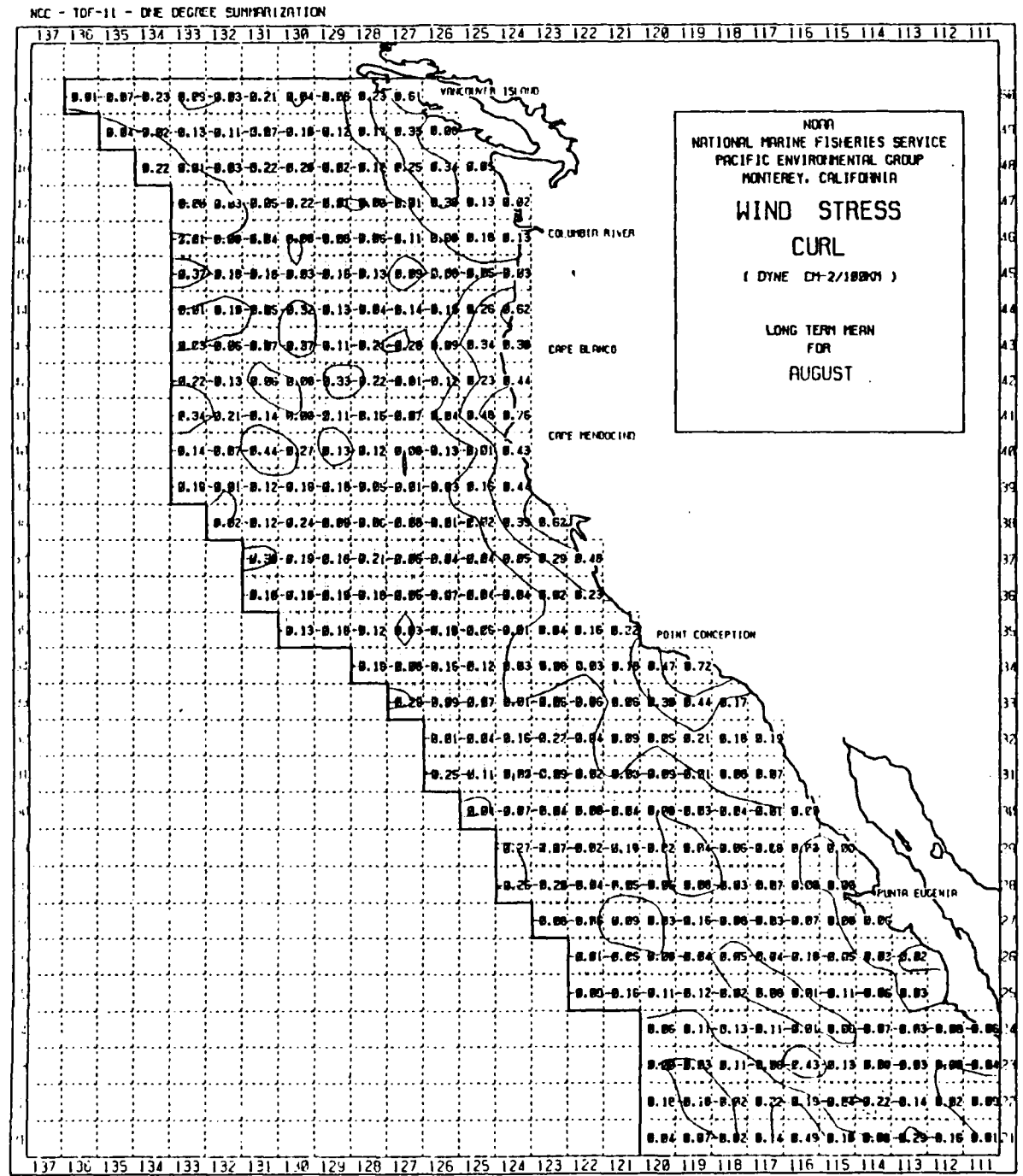


Figure 1.6 Climatological wind stress curl for August (from Nelson, 1977).

II. NUMERICAL MODEL OF THE CALIFORNIA CURRENT SYSTEM

A. MODEL DESCRIPTION

1. Model Equations

The numerical model used in this research was developed by Haney (1974, 1985) and modified by Batteen (1989). Most recently, the model, including specific modifications applicable to this study, has been thoroughly detailed in Batteen *et al.* (1989) and that discussion has been summarized here for the convenience of the reader. The model is a multilevel, primitive equation (PE) model which uses hydrostatic, rigid lid, and β -plane approximations. While the model also has a topographic capability, a flat-bottom is used in this study to ensure separation of the wind forcing role from the possible coupled role of wind forcing with bottom topography. The governing equations are as follows:

a. Momentum Equations:

$$\frac{du}{dt} = \frac{-1}{\rho_0} \frac{\partial p'}{\partial x} + fv - A_m \nabla^4 u + K_m \frac{\partial^2 u}{\partial z^2} + \delta_a(u) \quad (2.1)$$

$$\frac{dv}{dt} = \frac{-1}{\rho_0} \frac{\partial p'}{\partial y} - fu - A_m \nabla^4 v + K_m \frac{\partial^2 v}{\partial z^2} + \delta_a(v) \quad (2.2)$$

b. Continuity Equation:

$$w = \int_{-H}^z \left(\frac{\partial u}{\partial x} + \frac{\partial v}{\partial y} \right) d\xi \quad (2.3)$$

c. Vertically Integrated Hydrostatic Equation:

$$p' = \int_z^0 \rho g d\xi - \frac{1}{H} \int_{-H}^0 \left[\int_z^0 \rho g d\xi \right] dz \quad (2.4)$$

d. Equation of State:

$$\rho = \rho_0 (1 - \alpha (T - T_0)) \quad (2.5)$$

e. Thermodynamic Equation:

$$\frac{dT}{dt} = -A_H \nabla^2 T + K_H \frac{\partial^2 T}{\partial z^2} + Q_s + \delta_d (T) \quad (2.6)$$

In the above equations, t is time, (x,y,z) is a right-handed cartesian coordinate system with x pointing towards the shore, y alongshore, and z upward, with (u,v,w) being the corresponding velocity components. Temperature is denoted by T , density by ρ , and the departure of the pressure from the vertically averaged pressure by p' . In equations (2.3) and (2.4), ξ is a dummy variable of integration. Equation (2.4) includes the assumption that the depth-averaged pressure is a constant (assumed zero); i.e., the barotropic mode is ignored in this study. Equation (2.5) assumes that density is a function of temperature only. This assumption is consistent with the region being modeled (Lynn *et al.*, 1982). Salinity may be a good water mass tracer in the CCS (Huyer and Kosro, 1987; Lynn and Simpson, 1987), but inclusion of salinity in the calculations is not essential for a zero-order description of the CCS because there are no major sinks or sources of salinity in the model area.

In (2.6), $Q_s = \partial S / (\rho_0 C \partial z)$ is the heating due to solar radiation, with

$$S = S_0 (R e^{z/z_1} + (1 - R) e^{z/z_2}) \quad (2.7)$$

Here S_0 is the downward flux of solar radiation at the surface, $R = .62$ is the fraction of solar radiation absorbed in the upper few meters ($z_1 = 1.5$ m) and $(1 - r) = .038$ is the fraction that penetrates to somewhat deeper levels ($z_2 = 20$ m) as given by Paulson and Simpson (1977). The terms $\delta_a(u)$, $\delta_a(v)$, and $\delta_a(T)$ represent the vertical turbulent mixing of heat and momentum by a dynamic adjustment mechanism. This adjustment, a generalization of the convective adjustment mechanism, is based on the assumption of a critical Richardson number, and it serves to maintain dynamic stability in the water column (Adamec *et al.*, 1981).

The boundary conditions at the top ($z=0$) of the model ocean are:

$$K_m \frac{\partial u}{\partial z} = 0 \quad (2.8a)$$

$$K_m \frac{\partial v}{\partial z} = \tau/\rho_0 \quad (2.8b)$$

$$K_H \frac{\partial T}{\partial z} = -Q_B \quad (2.8c)$$

$$w = 0, \quad (2.8d)$$

and at the bottom ($z = -H$) they are

$$K_m \frac{\partial u}{\partial z} = C_D (u^2 + v^2)^{1/2} (u \cos \gamma - v \sin \gamma) \quad (2.9a)$$

$$K_m \frac{\partial v}{\partial z} = C_D (u^2 + v^2)^{1/2} (v \cos \gamma - u \sin \gamma) \quad (2.9b)$$

$$K_H \frac{\partial T}{\partial z} = 0 \quad (2.9c)$$

$$w = 0 \quad (2.9d)$$

In (2.8b), τ is the alongshore component of the surface stress which is varied in accordance with the experimental conditions as noted. In (2.8c), Q_B is the net upward

flux of longwave radiation, sensible and latent heat across the sea surface which is described below. In (2.9a,b), $\gamma = 10^\circ$ is a geostrophic inflow angle (Weatherly, 1972). The bottom stress in (2.9a,b) represents one of the simplest possible parameterizations of a bottom Ekman layer. Table I provides definitions for other symbols used in the model equations. This table also provides values for the constants used throughout the study.

2. Model Domain and Resolution

The domain of the model is rectangular in shape covering an area of 6° of latitude by 6° of longitude. The area of interest extends from 124° to 130° W and from 36.5° to 42.5° N (Figure 2.1). Extending off the coast of central California approximately 512 km, the model extends from Pt. Sur in the south to Cape Blanco in the north (640 km). The horizontal model grid is comprised of 65 by 65 points with 8 km resolution in the cross-shore direction and 10 km resolution in the alongshore direction. This horizontal resolution is adequate for resolving mesoscale features in the CCS whose scales are approximately 100 to 300 km (Bernstein *et al.*, 1977; Breaker and Mooers, 1986; Freitag and Halpern, 1981). The California coast is approximated with a straight line and topography is ignored. Both of these approximations are necessary to allow for the isolation of wind forcing effects from other contributing factors.

Table I Constants used in the model.

	VALUE	DEFINITION
C	0.958 cal gm ⁻¹ (°K) ⁻¹	specific heat of sea water
C _D	1.225 × 10 ⁻³	drag coefficient
T.	278.2°K	constant reference temperature
ρ _a	1.23 × 10 ⁻³ gm cm ⁻³	density of air
ρ _o	1.20276 gm cm ⁻³	density of sea water at T.
α	2.01 × 10 ⁻⁴ (°K) ⁻¹	thermal expansion coefficient
K	10	number of levels in vertical
Δx	8 × 10 ⁵ cm	cross-shore grid spacing
Δy	1 × 10 ⁶ cm	alongshore grid spacing
D	4.5 × 10 ⁵ cm	total ocean depth
Δt	800 s	time step
f _o	0.93 × 10 ⁻⁴ s ⁻¹	mean Coriolis parameter
g	980 cm s ⁻²	acceleration of gravity
A _M	2 × 10 ¹⁷ cm ⁴ s ⁻¹	biharmonic momentum diffusion coefficient
A _H	2 × 10 ¹⁷ cm ⁴ s ⁻¹	biharmonic heat diffusion coefficient
K _M	0.5 cm ² s ⁻¹	vertical eddy viscosity
K _H	0.5 cm ² s ⁻¹	vertical eddy conductivity
p _{surf}	1013.25 mb	surface air pressure
Ω	2 π day ⁻¹	earth rotation rate

3. Finite Difference Scheme

A space-staggered B-scheme is utilized for differencing in the horizontal (Arakawa and Lamb, 1977; Batteen and Han, 1981). A sigma coordinate system is incorporated in the model giving 10 layers in the vertical. Since bottom topography is ignored, these layers are separated by constant z-levels at depths of 13, 46, 98, 182,

316, 529, 870, 1416, 2283 and 3656 m. This vertical spacing is advantageous in that it allows more layers to be concentrated in the upper, more dynamically active surface region.

4. Heat and Momentum Diffusion

Biharmonic lateral momentum and heat diffusion are used in the model to allow for less restriction of baroclinic and barotropic instability processes. Laplacian lateral heat diffusion can decrease baroclinic signals associated with eddy generation (Holland and Batteen, 1986). Further, biharmonic diffusion is selective for scales smaller than those of eddies (Holland, 1978), therefore allowing eddy generation as a result of baroclinic and barotropic instability mechanisms.

5. Surface Thermal Forcing

The solar radiation at the sea surface, S_0 , was specified to be the summer- and CCS-mean value from Nelson and Husby (1983). The sum of the net longwave radiation, latent and sensible heat fluxes, Q_B , was computed during the model experiments from standard bulk formulas (Haney *et al.*, 1978) using the summer- and CCS-mean value of alongshore wind, cloud cover, relative humidity, air temperature and model-predicted sea surface temperature. The sea surface temperature for the experiments of this study was chosen so that the total heat flux across the sea surface, $S_0 - Q_B$, was zero at the initial time. The only surface heat flux forcing, therefore, was that which developed as a result of sea surface temperature variation being forced by the wind. This highly simplified formulation of the surface thermal forcing in the model was utilized to focus the study on wind forced variation of the thermal structure

in the CCS. Further discussions concerning both the necessity and applicability of this formulation are found in Batteen *et al.* (1989) and Haney (1985).

6. Boundary Conditions

The California coastline is modeled as a straight, vertical wall and represents the eastern boundary of the model. A no-slip condition is imposed on the tangential velocity at the coastline.

The northern, southern, and western boundaries are open (Camerlengo and O'Brien, 1980). The application of open boundary conditions can lead to unrealistic results in studies utilizing wind forcing if the forcing is applied to the entire domain including the open northern and southern boundaries. Uniform wind forcing of this form will result in a steady alongshore current which is both too strong and too deep, and is also equatorward with no undercurrent (McCreary, 1981). Following the work of Batteen *et al.* (1989) and McCreary *et al.* (1987) wind band forcing of the form

$$\tau = \tau_0 Y(y) \quad (2.10)$$

is used in all model runs to generate a more realistic current structure. The wind stress forcing at a location is represented by τ_0 and will vary in these experiments in either x alone, or in both x and y depending on the specific experimental conditions. $Y(y)$ is the imposed latitudinal variation in the stress given by the following equation:

$$Y(y) = \begin{cases} 1 & 100 \text{ km} < y < 600 \text{ km} \\ 0 & \text{otherwise.} \end{cases} \quad (2.11)$$

This form for $Y(y)$ results in the imposition of wind forcing in the interior of the model domain only and allows for the propagation of coastal trapped Kelvin waves.

It is these Kelvin waves which produce the alongshore pressure gradient and the resultant surface trapped coastal jet and undercurrent (Batteen *et al.*, 1989).

7. Initial Conditions

The model has the option of being spun up from rest by surface winds or heat flux, or being initiated with a specific current field. All experiments conducted in this study were started from rest and forced using wind stress alone. The specific wind forcing conditions of each experiment are discussed in the following section.

An exponential temperature profile was used in all experiments to give the mean stratification. This profile had a length scale of $h = 450$ m and took the form

$$T(z) = T_B + \Delta T e^{z/h}, \quad (2.12)$$

where $T_B = 2$ °C is the temperature at great depth and $\Delta T = 13$ °C is the temperature change from the bottom of the ocean to the surface. This temperature profile is considered to be representative of the long-term, mean climatological temperature stratification of the CCS and was developed by Blumberg and Mellor (1987) for use in the Dynalysis of Princeton model.

B. SPECIFIC EXPERIMENTAL CONDITIONS

1. Transient Wind Forcing (Exps. 1-2)

a. Experiment 1

Transient wind forcing as a mechanism for baroclinic / barotropic instability is a poorly understood phenomenon. McCreary *et al.* (1987) have laid a strong foundation for the study of transient wind forcing in their work and it is the

purpose of the first two experiments to expand on this previous study. They utilized a viscid linearized model to investigate the effects of annually periodic wind stress forcing on the dynamics of the CCS. The forcing used is as shown below in Equation 2.13 (McCreary *et al.*, 1987, Equation 11).

$$\tau^y = \tau_0 Y(y) (.5 + .4 e^{-i\sigma t}) + \tau_0 X(x) Y(y) (.45 + .15 e^{-i\sigma t}) \quad (2.13)$$

In this equation τ^y represents the meridional stress; τ_0 is an initial stress value set equal to -1 dyne / cm²; σ is an oscillatory annual period equal to 2π / year; t represents time, with June 1 set equal to zero; $Y(y)$ is a meridional weighing function; and $X(x)$ represents the zonal distribution of the stress. McCreary *et al.* used a cosine function to taper the meridional distribution of the stress at the northern and southern boundaries. In this study $Y(y)$ was formulated as previously described. The $X(x)$ weighing function acts to modify the wind stress component of Equation 2.13 and produces wind stress curl in the model domain. The exact formulation of $X(x)$ is given by

$$X(x) = \begin{cases} \sin \frac{\pi |x|}{2 \Delta}, & -\Delta < x \leq 0 \\ 1, & x \leq -\Delta \end{cases} \quad (2.14)$$

where x is equal to zero at the coast and Δ is equal to 200 km.

Equation 2.13 represents two distinct forcing terms. The left half of the right hand side (RHS) of the equation, $\tau_0 Y(y) (.5 + .4 e^{-i\sigma t})$, represents the meridionally constant wind stress portion of the forcing function, while the other half of the RHS, $\tau_0 X(x) Y(y) (.45 + .15 e^{-i\sigma t})$, acts to produce the wind stress curl part of the idealized wind field. This formulation gives a maximum positive curl at the coast and non-zero means for both the stress and curl components of the wind field. These

two characteristics correlate well with observations of the CCS (Nelson, 1977; Hickey, 1979). Additionally, this formulation allows the relative contributions of each component to vary over the annual cycle.

Experiment 1 is forced throughout the domain with Equation 2.13. The experiment was initialized with a t value equal to December 1 and the equation utilized the same time step as found in the model, 800 seconds, with t being reset to 0 on June 1 in a cyclic manner. December is a minimum in the strength of the forcing function, but is also the month when the ratio of wind stress to wind stress curl is the smallest so that the curl makes its largest relative contribution. The December starting point was chosen to allow the model sufficient time to spin up and establish a proper current structure before the upwelling season begins (usually around March). Figure 2.2 shows a graph of the initial forcing function compared to the climatological values of Nelson (1977). Although the full wind stress / curl formulation of McCreary *et al.* (1987) does follow the trend of the climatological data, it is seen that the climatological values are more positive (less intense) throughout the region.

b. Experiment 2

Experiment 2 was the same as Experiment 1 except for the starting date. A time value of June 1 was used to initialize the experiment to allow the two extremes (i.e., December and June) of the forcing function to be tested. June represents the maximum forcing values from Equation 2.13 and the largest ratio of wind stress to wind stress curl. This maximum correlates well with observations for the month of June (Nelson, 1977), a major upwelling month. Starting at this time also more closely resembles Experiments 3 through 6 which were initialized with the strong

climatological wind stress values seen in the summer months. A plot of Equation 2.13 for June 1 with comparisons to climatological data is given in Figure 2.3 and again it is seen that the Equation 2.13 solutions of McCreary *et al.* (1987) are stronger than climatology. All other factors remained the same as in the above experiment.

2. One Degree Climatological Wind Forcing (Exps. 3-5)

a. Experiment 3

The wind stress field for Experiment 3 was derived from Nelson (1977). Nelson utilized historic ship reports covering a time period from the mid-19th century to 1972 to compile monthly wind stress and wind stress curl averages for one degree boxes along the west coast of the United States.

The north-south component of the monthly stress averages of each one degree block for the months of June, July and August were averaged giving a mean summer stress value for each block. (Refer to Figures 1.1 through 1.6 for the appropriate monthly plots.) These one degree summer stress averages were then utilized to initiate the model. The cross shore (east-west) wind stress component is much less than the alongshore component and can be ignored for a first order approximation (Nelson, 1977; Chelton *et al.*, 1987). The six degree by seven degree (six by seven points) climatological stress domain was fit to the 65 by 65 model grid utilizing a bivariate interpolation scheme after Akima (1978).

The original one degree stress values were computed such that the average was valid in the middle of a one degree box. As a result, the first stress value available for the interpolation was actually 42.5 km (one half of a degree of latitude)

offshore. The interpolation scheme had a closed boundary to interpolate to except at the coast. This inconsistency led to the necessity of some form of artificiality in the coastal wind field. The nearshore region is possibly the most dynamically important area in the coastal upwelling region (Philander and Yoon, 1982; Allen, 1980) and as such, the treatment of this region becomes of major importance.

In Experiment 3 the wind stress in the nearshore region, within 48 km of the coast throughout the north-south extent of the model, was set constant to an equatorward stress of 1 dyne cm^{-2} . This value for wind stress is a good approximation of the summer climatological mean for the area of the model domain (Nelson, 1977). This treatment of the wind stress eliminates all spatial variability in the nearshore region, reducing the total wind stress curl to zero. Neglecting wind stress curl in the nearshore region can be justified via a scaling argument (Allen, 1980), but again, the effects of this neglect are not clearly understood.

b. Experiment 4

Experiment 4 utilized wind stress fields developed in a manner similar to that of Experiment 3, again using data from Nelson (1977). The difference in the two experiments lies in the treatment of the wind field next to the coast. In Experiment 4, the wind stress was set constant in the east-west direction in the region within 48 km of the coast. This method of portraying the nearshore wind stress field has the advantages of using real wind stress values, i.e., ones obtained from a closed boundary interpolation, in the data poor region near the coast, and it also allows for change in the meridional wind field in the coastal region. However, setting the wind stress zonally constant does result in zero curl in this region. The curl in the coastal

region of the west coast of California has been shown to be climatologically positive (Nelson, 1977). Even though spatial diversity in y has been introduced in the nearshore region, it still does not accurately represent climatology.

c. Experiment 5

Experiment 5 represents the first simulation utilizing full two dimensional surface wind stress forcing throughout the entire model domain. As in the previous 2 experiments, one degree climatological wind stress data was used for forcing (Nelson, 1977). In Experiment 5, the interpolation routine is allowed to extrapolate the trend established just offshore to obtain values for the nearshore wind stress field. The resultant model wind stress field, varying in both x and y , is shown in Figure 2.4. It was this interpolated wind stress field that was used to initialize the model. As will be seen later, the interpolated wind stress field compares well with finer resolution data. There is a zero curl line off the coast at ~ 128 km and positive curl at the coast throughout the model. However, the stress maximum does reach the coast at $y \sim 280$ km, lower than is actually seen climatologically.

3. Two Tenths Degree Climatological Wind Forcing (Exp. 6)

a. Experiment 6

Experiment 6 was initiated utilizing a wind stress field derived from monthly stress averages calculated for two tenths degree boxes along the western coast of California (Nelson, Unpublished Data). The data was compiled in a manner similar to the two tenths degree data above (Nelson, 1977; Parrish *et al.*, 1983; Nelson, Personal Communication). The stress values were based on approximately two million

historical ship observations in the Tape Data Family II (National Climatic Center, NOAA/EDIS/NCC, Asheville, N.C.) accumulated from the mid-1800's up to 1979. The observations were biased towards the coastlines and transoceanic shipping lanes, making the data sparse nearshore region of Experiments 3, 4 and 5 the most heavily sampled area. A single pass editor was used to remove gross errors in the data, including erroneous position reports and observations which exceeded extreme value limits. Upon completion of editing, independent monthly averages were calculated for each two tenths degree square. A summer mean for each block was computed by averaging the monthly means for June, July and August. Since the original block values were calculated independently of each other, several areas of erroneous data developed in the averaged field. To smooth out these isolated discontinuities, the summer mean data was run through a three by three median filter (Rabiner *et al.*, 1975).

The averaged, smoothed two tenths degree data covered an area from the coast to 255 km offshore, and 640 km alongshore, from 36.55° to 42.55° N. The data was sampled as depicted in Figure 2.5, paralleling the coast as closely as possible. The fine resolution of the data enabled the acquisition of wind stress values right at the coast, i.e., there is now a closed boundary at the coast. No artificiality is introduced by the interpolation scheme. The 16 X 31 two tenths degree data grid was interpolated to fit the model grid of 8 km X 10 km resolution (Akima, 1978). The area offshore where two tenths degree data was unavailable was filled utilizing interpolated one degree data from above. The resultant wind stress field used in this experiment is shown in Figure 2.6.

The two tenths degree data has several advantages over the one degree data used in the previous experiments. First, interpolation was possible right up to the coast eliminating the artificiality and approximations required in Experiments 3, 4, and 5. The complexity of the wind field in the nearshore region was greatly enhanced giving a much more realistic portrayal of actual conditions. Secondly, even in the offshore region more detail in the wind stress field is noted. Of particular interest is the jet extending up across the domain from 260 km to 440 km in the alongshore direction, and from 160 km offshore to the coast at the top of its extent. The upper maximum of this jet is roughly coincident with Cape Mendocino, an area of climatologically strong wind stress (Nelson, 1977). In contrast, the maximum value found for the interpolated one degree data (Figure 2.4) is not as large, it covers a much wider, less concentrated area, and it reaches the coast at $y \sim 280$ km, much lower in the domain. Specific conditions for all experiments in this thesis are summarized in Table II.

TABLE II Summary of Experimental Conditions

EXPERIMENT	CORIOLIS	WIND FORCING	TIME DEPENDENCE	NEARSHORE FORMULATION
Experiment 1	β - Plane	McCreary <i>et al.</i> (1987) Eqn. 11 Start date of December 1. Variation in x only with positive wind stress curl at the coast.	Annual Cycle	Equation solved up to coast. Variation in x only.
Experiment 2	β - Plane	McCreary <i>et al.</i> (1987) Eqn. 11 Start date of June 1. Variation in x only with positive wind stress curl at the coast.	Annual Cycle	Equation solved up to coast. variation in x only.
Experiment 3	β - Plane	1° wind stress climatology (Nelson, 1977). Full x-y variation. Values averaged to give summer mean (Jun, Jul, Aug).	None	Wind stress set constant to -1 dyne / cm ² from the coast to 48 km off shore. No spatial variation.
Experiment 4	β - Plane	1° wind stress climatology (Nelson, 1977). Full x-y variation. Values averaged to give summer mean (Jun, Jul, Aug).	None	Wind stress set zonally constant from the coast to 48 km off shore. Variation in y only.
Experiment 5	β - Plane	1° wind stress climatology (Nelson, 1977). Full x-y variation. Values averaged to give summer mean (Jun, Jul, Aug).	None	Nearest off shore values extrapolated to coast. Variation in x and y.
Experiment 6	β - Plane	.2° wind stress climatology (Nelson, Unpub. Data) used within 255 km of coast. 1° data utilized to fill remainder of model domain. Full x-y variation. Values averaged to give summer mean (Jun, Jul, Aug).	None	.2° data available up to the coast allowing for interpolation in the nearshore region. Variation in x and y.

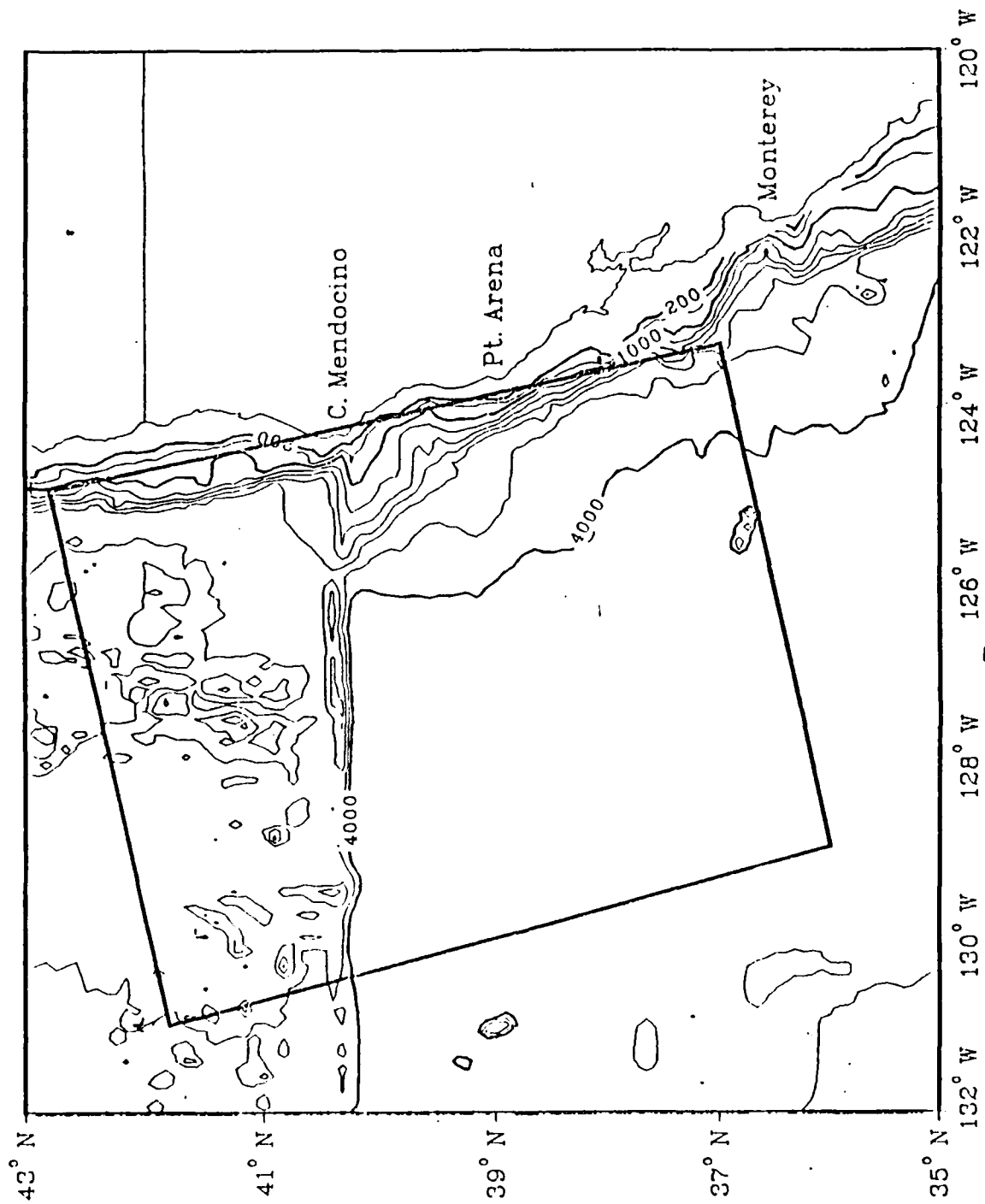


Figure 2.1 Study domain. The rectangle represents the primitive equation (PE) model domain. Bathymetry in meters.

DECEMBER
ALONGSHORE WIND STRESS, τ_y

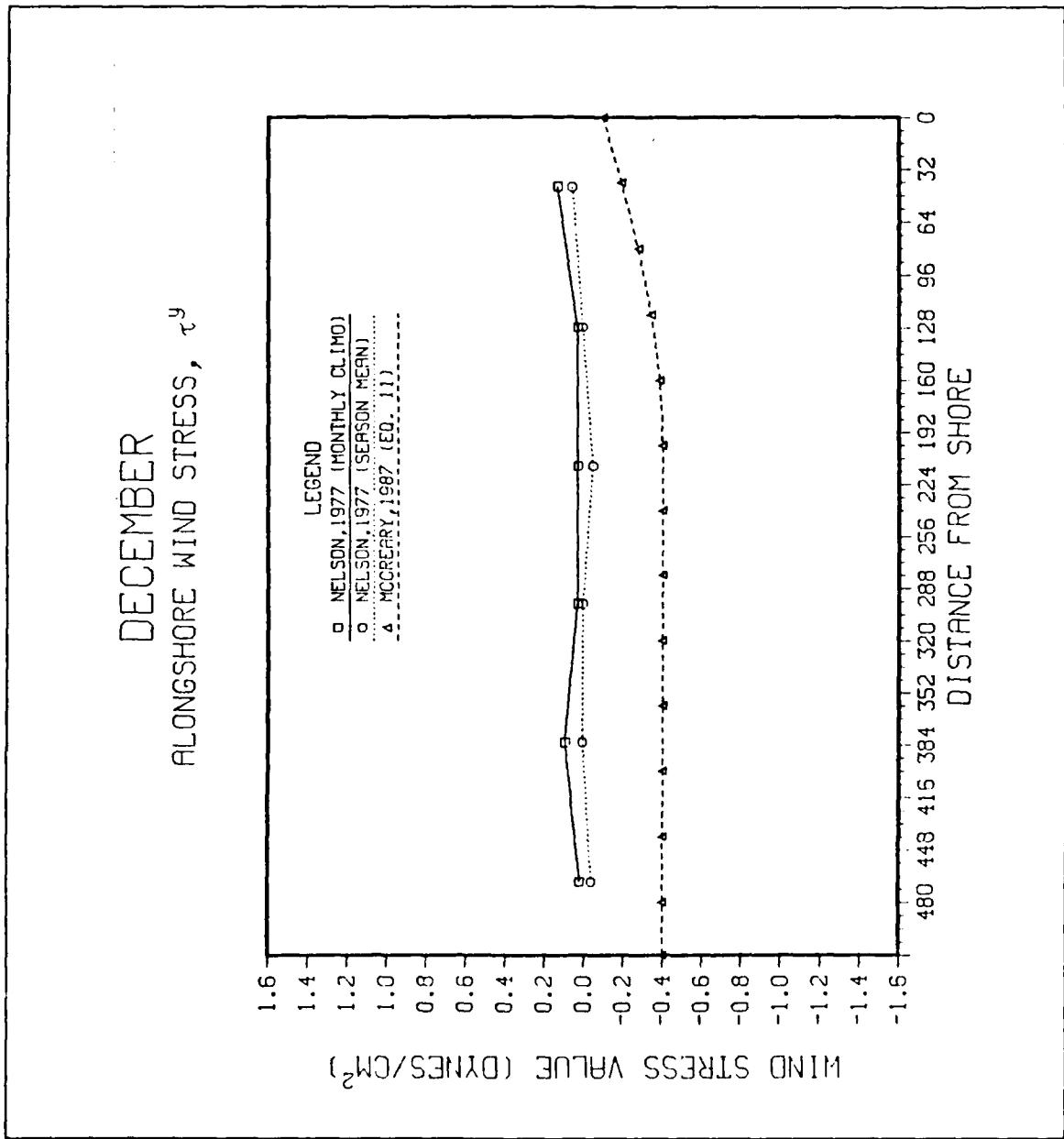


Figure 2.2

Wind stress versus offshore distance for December. The climatological wind stress data is an alongshore average with the seasonal average being comprised of December, January, and February (Nelson, 1977). McCreary's Equation 11 (McCreary *et al.*, 1987) is given in Equation 2.8 of this thesis. Solution of this equation was made for December 1.

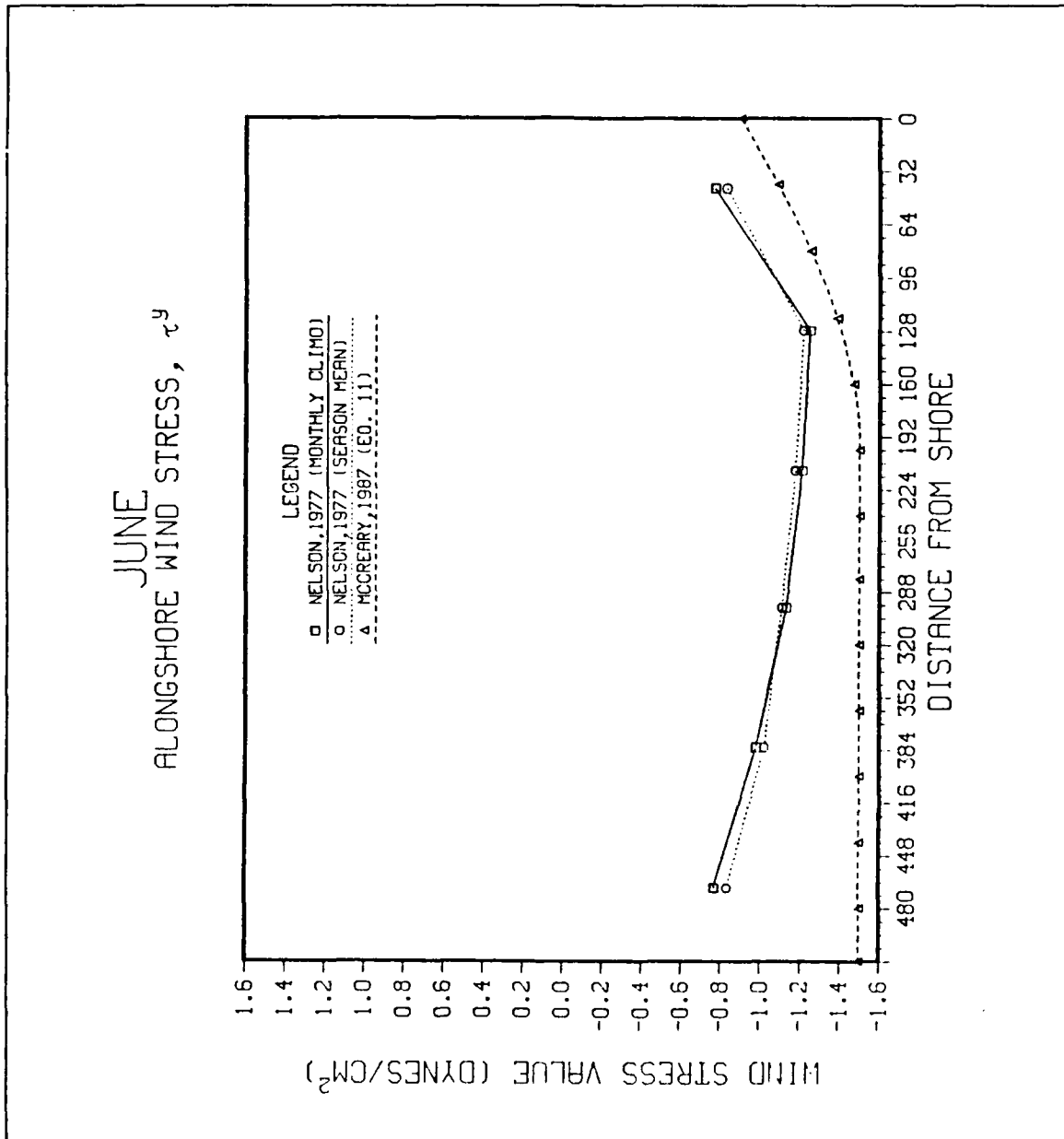


Figure 2.3 Wind stress versus offshore distance for June. The climatological wind stress data is an alongshore average with the seasonal average being comprised of June, July, and August (Nelson, 1977). McCreary's Equation 11 (McCreary *et al.*, 1987) is given in Equation 2.8 of this paper. Solution of this equation was made for June 1.

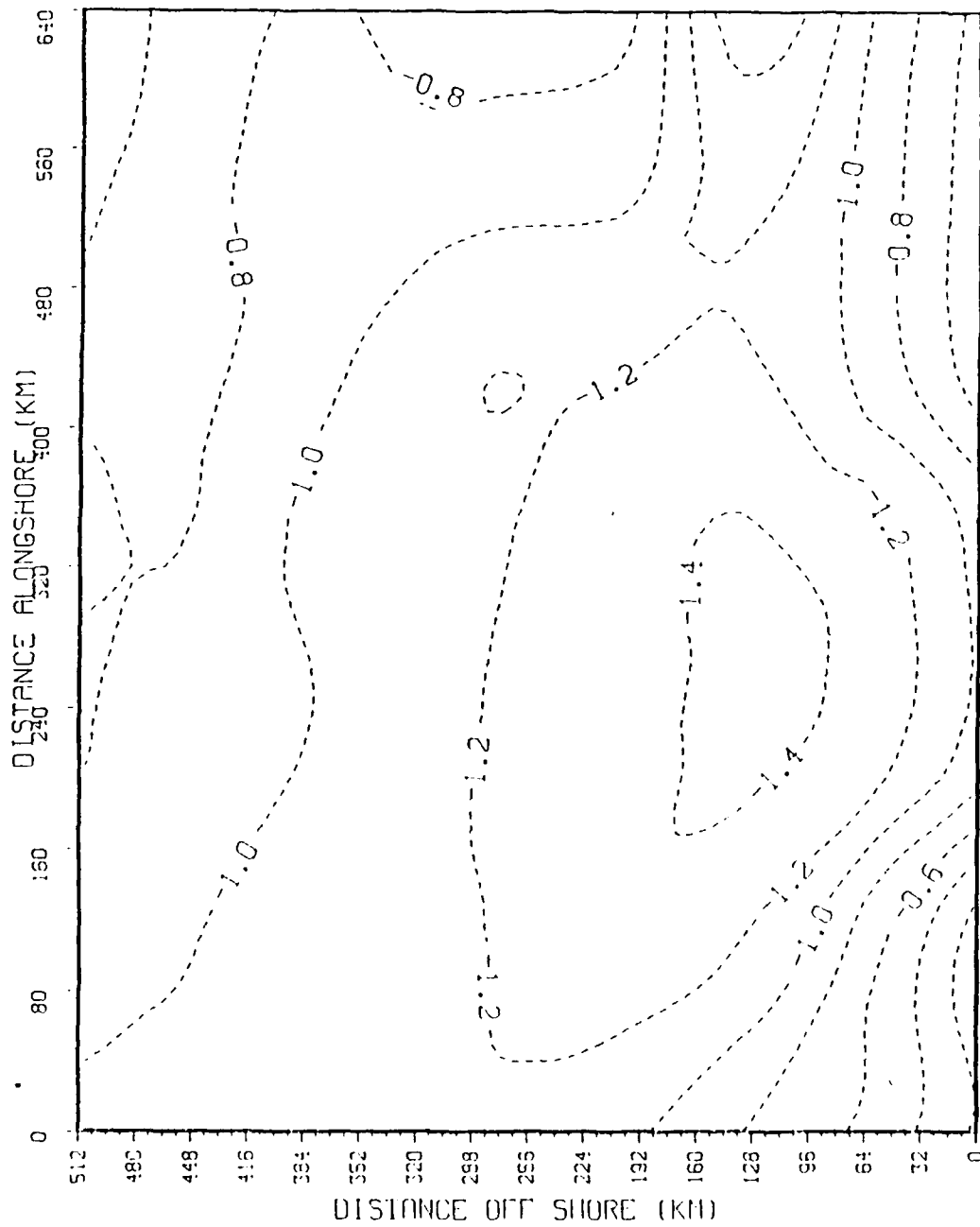


Figure 2.4 Wind stress isopleths for one degree resolution climatological data over the model domain. Contour interval is .2 dyne / cm².

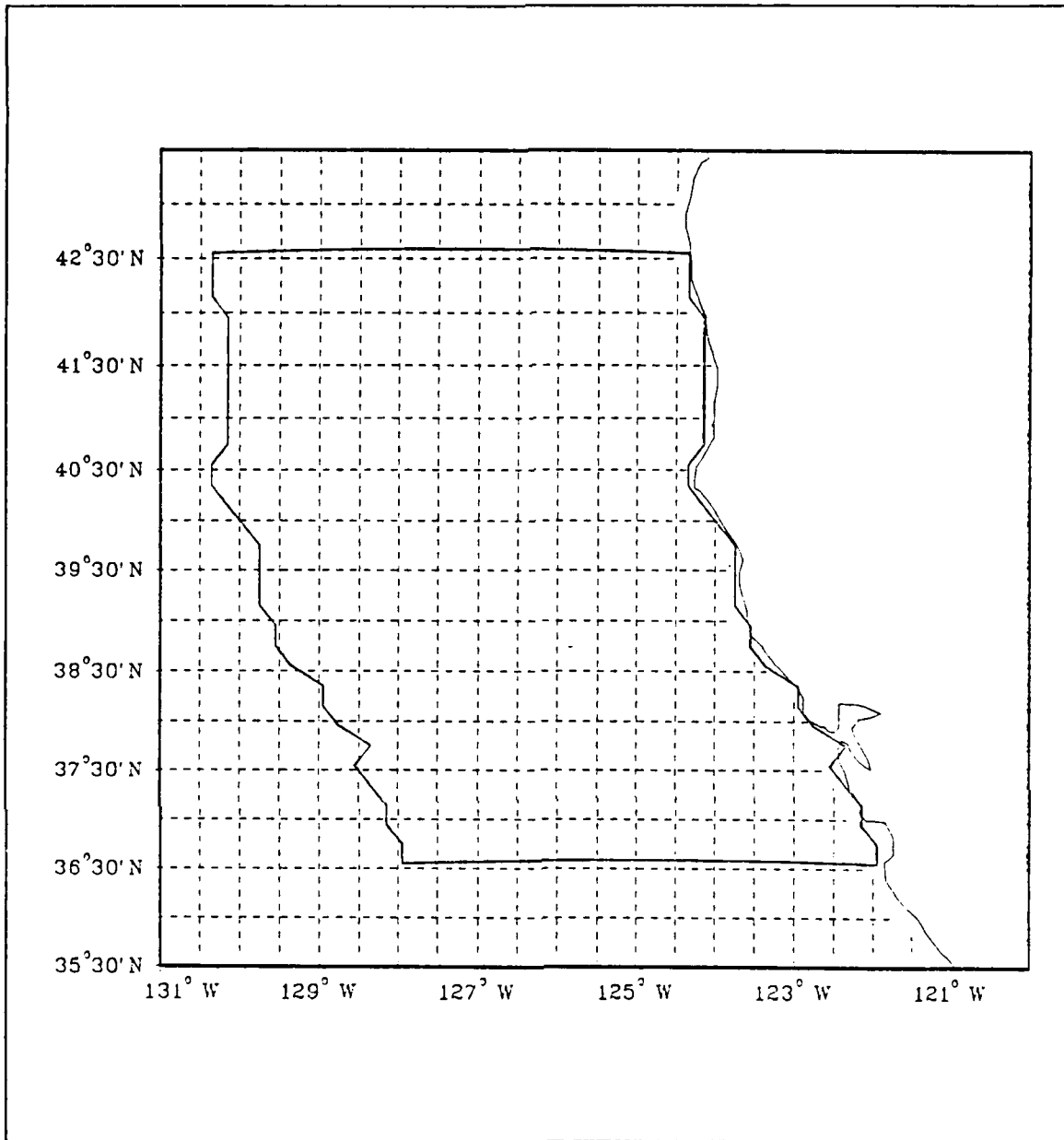


Figure 2.5 Sampling domain for the two tenths degree climatological wind stress forcing. Sampled area is outlined.

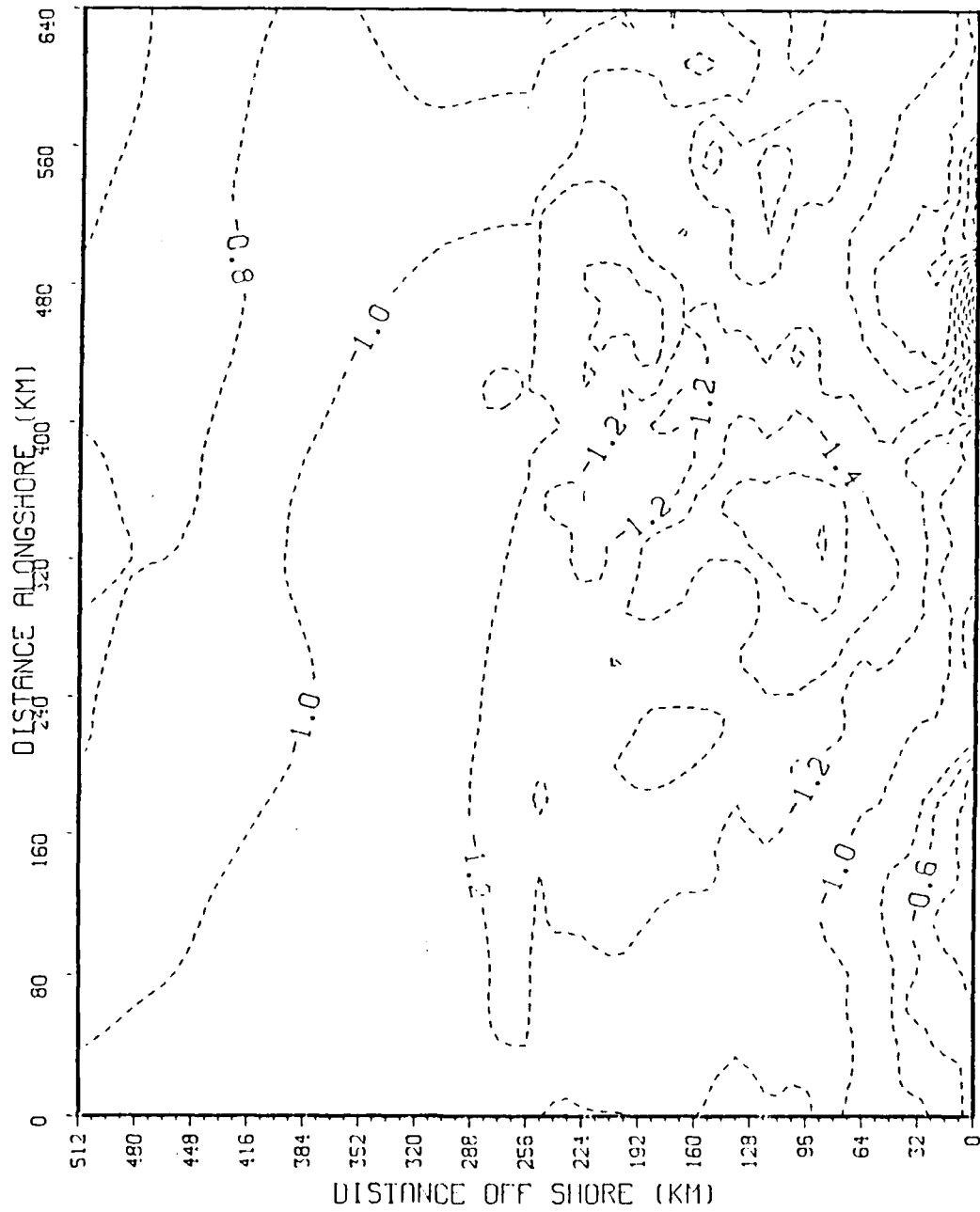


Figure 2.6

Wind stress isopleths for one degree / two tenths degree resolution climatological data over the model domain. Contour interval is .2 dyne / cm².

III. EXPERIMENT RESULTS

A. TRANSIENT WIND FORCING

1. Experiment 1

The transient wind forcing experiments, numbers 1 and 2, were designed to replicate work done by McCreary *et al.* (1987) using a primitive equation model. McCreary *et al.* forced a linearized model with equation 2.13 and were able to produce a model current system which varied in a manner similar to that of the CCS. However, the results of McCreary *et al.* did not include the formation of eddies and filaments. It was hoped that inclusion of the nonlinear terms would allow for eddy development. The sensitivity of the model to the starting date of the wind forcing was not known so the model was initiated with two different times.

Experiment 1 was initiated with a starting time of December 1, representing the minimum forcing values for wind stress and curl. Unlike the rest of the experiments, the model was extremely slow. For example, on day 20 (December 20) an alongshore current was still not established, there was negligible offshore Ekman transport, and there were no perturbations in the temperature field.

A poleward alongshore surface current finally developed in the nearshore region on day 25 (December 25). The poleward nature of this surface current is consistent with the dominance of the curl component over the stress in the wind forcing function with a December 1 start date. As will be seen in later experiments,

all run in the summertime, the initial reaction in the model is usually driven predominately by the equatorward wind stress. In this experiment, however, the stress is completely overwhelmed from the very beginning by the curl portion of the forcing function. Ekman transport throughout the model domain on day 25 (December 25) is still extremely weak and calculations of dynamic heights with reference to 2400 m show no perturbations at the surface. If upwelling of cold water was ongoing, it would appear as a negative pressure perturbation due to the denser nature of the cold upwelled water. Conversely, downwelling can be characterized as positive pressure perturbations. The lack of any pressure structure in the dynamic height plots serves to illustrate the quiescent nature of this experiment.

Development continues in this weak manner throughout the experiment. A equatorward coastal flow is first seen in the northern portion of the model domain on day 40 (January 10). Experiment 1 was concluded after 60 days (February 1). Figure 3.1 shows the zonal (u) and meridional (v) velocities, temperature (T) and pressure (p) fields for day 60 of Experiment 1. Poleward flow is dominant in the nearshore region and has reached a maximum velocity of 4 cm s^{-1} (Fig. 3.1b). Equatorward coastal flow is evident in the northern reaches of the model, but has reached a velocity of only 2 cm s^{-1} . The southern extent of this equatorward jet has slowly increased throughout the experiment and extends to $y \sim 448 \text{ km}$. Equatorward flow is also evident offshore of 100 km. The temperature field (Fig. 3.1c) shows downwelling coincident with the poleward surface current and weak upwelling coincident with the equatorward flow at $y \sim 550 \text{ km}$. In later experiments it will be seen that Ekman transport is most strongly influenced by the direction of the wind stress. Here,

however, it appears that the poleward current flow due to the curl dominates equatorward wind stress.

Overall, these results compare favorably with McCreary *et al.* (1987). They found that when wind stress curl dominated in relation to wind stress, as was the case in this experiment, a broad poleward surface current developed in the nearshore region with equatorward flow offshore at approximately 100 km. Both these features were seen in Experiment 1. Furthermore, neither McCreary *et al.* nor Experiment 1 showed any signs of instability or concurrent mesoscale processes. Additionally, McCreary *et al.* observed that as the strength of the stress forcing component increased in proportion to the wind stress curl component, an equatorward coastal jet became discernible. This phenomenon was seen in this experiment. As the model simulation time progressed through January, the equatorward flow increased in width and in southern extent. Theoretically, if computer resources had allowed for the extension of this experiment, the equatorward jet should continue to grow and develop in a manner similar to a summer regime. These results support the concept that positive wind stress curl can generate both a poleward surface current at the coast and an equatorward flow offshore which are seen in the winter season (McCreary *et al.*, 1987).

2. Experiment 2

Experiment 2 was initiated with a forcing function representing the wind stress of June. As previously mentioned, June has the maximum wind stress forcing of the yearly cycle, and is the month which depicts the greatest ratio of wind stress to wind stress curl seen throughout the year (Nelson, 1977).

As expected, the equatorward coastal jet sets up early in the model run. On day 5 (June 5) a coastal jet has developed (Fig. 3.2b) extending from the northern boundary to the southern extent of the forcing ($y = 100$ km). The velocity of this jet is 12 cm s^{-1} , a relatively large value when compared to Experiment 1. Offshore Ekman flow is also strong at this time (Fig. 3.2a) and upwelling as denoted by the closed 14° isotherm (Fig. 3.2c) is evident along the coast.

The cross-shore plot of the alongshore averaged velocity field for day 10 (June 10, Fig. 3.3) shows the current field to be characterized by an equatorward jet extending to a depth of 100 m with an undercurrent from 100 m to 320 m. The width of this jet is at a maximum early in the run and does not exceed ~ 40 km. The associated vertical temperature plot for day 10 (Fig. 3.4) shows a bending up of the isotherms in the nearshore region down to a depth of 100 m, just above the undercurrent. This bending is indicative of the upwelling in the region. What is not seen is a bending down of the isotherms below the undercurrent as would be expected as a result of the undercurrent forced Ekman flow.

This pattern of development continues to day 25 (June 25, Fig. 3.5) when the nearshore poleward flow becomes dominant and offshore equatorward flow develops. The coastal jet still exists with a velocity of 10 cm s^{-1} , but it is steadily being overwhelmed by the poleward flow (Fig. 3.5b). Although the northern areas of the model domain still show an equatorward jet overlaying an undercurrent, the average alongshore flow in the model (shown for day 30 in Figure 3.6) has become poleward in the nearshore region with only a very thin band of equatorward flow evident at the surface. The temperature signature at the coast has developed a core of 13°C (Fig.

3.5c). The pressure field for this day (Fig. 3.5d) shows little structure, with only one large meridionally oriented negative perturbation indicative of coastal upwelling.

By day 80 (July 20) the coastal equatorward jet (Fig. 3.7b) has been nearly eliminated. The poleward surface flow dominates the nearshore region out to approximately 100 km and has reached a velocity of 8 cm s^{-1} . The predominant feature in the offshore region is a weak equatorward surface flow, of $\sim 4 \text{ cm s}^{-1}$. Offshore Ekman transport is still evident (Fig. 3.7a), but onshore Ekman forcing by the poleward surface current is also exhibited. The upwelling temperature signature has been reduced in both area and strength and downwelling is also seen in the southern coastal region.

The features noted above continue to develop until the completion of the model run at day 120 (October 1). The nearshore poleward flow maintains a velocity of 8 cm s^{-1} , and extends out to 128 km from shore (Fig. 3.8b). The equatorward offshore flow has maintained the same intensity, but has become better defined. The Ekman induced upwelling has been greatly weakened and is now confined to the northernmost region of the model domain (Fig. 3.8c). While it appears that the poleward flow is causing a downwelling regime, this downwelling is extremely weak as seen in the vertical cross-shore plot of temperature (Fig. 3.9). The isotherms bend up slightly in the middle of the domain at $y \sim 290 \text{ km}$, but cross-sections south of this point show no isotherm deformation. The alongshore averaged velocity plot (Fig. 3.10) clearly shows the prevailing current structure of this model run. There is a poleward surface current well defined to a depth of 520 m and extending offshore to approximately 120 km, with an average maximum velocity of 6 cm s^{-1} . The offshore

region contains a broader, shallower, weaker equatorward flow, with a maximum velocity 4 cm s^{-1} .

McCreary *et al.* (1987) had similar model results for their transient wind forcing experiment. In general, their velocities for both the surface and undercurrent were comparable with those of this study. Neither experiment showed any signs of eddy or filament development. However, several inconsistencies do exist between the two simulations. While the coastal jet of McCreary *et al.* extended well offshore (greater than 200 km) and persisted in this form well into late fall, the jet of Experiment 2 did not exceed more than 40 km in width and as documented, showed rapid decline by late July. In addition, the growth of the poleward surface flow progressed at a faster rate than in McCreary *et al.* (1987). These differences in results are most likely due to differences in nonlinear versus linear models and to different treatments of the boundary conditions at the coast.

If computing resources had not been restricted to 120 days for this experiment, this experiment would have been continued for a full multi-year long simulation. This would have given continuity over the seasonal changes, and would have allowed for observations of the effects of continued periodic forcing.

B. ONE DEGREE CLIMATOLOGICAL WIND FORCING

1. Experiment 3

Extensive literature has documented the effects of one dimensional wind stress forcing both with and without curl components (e.g., McCreary *et al.*, 1987; Batteen *et al.*, 1989; Tielking, 1988). If in fact the nearshore region is the primary

area of eddy and filament developments in the CCS, then how we treat this specific area should play an important role in the mesoscale activity of the model. Experiments 3 and 4 use constant and meridionally varying forcing in the nearshore region to examine the role of these forms of forcing.

The coastal equatorward jet dominated the surface flow throughout the entire experiment run. By day 40 (Fig. 3.11) the surface meridional velocity contours (Fig. 3.11b) exhibited a surface equatorward jet ~ 64 km wide with a velocity of 35 cm s^{-1} . The width of this current agrees well with the results of Batteen *et al.* (1989) in their constant stress, β -plane simulation, but the speed in this experiment is considerably larger. Batteen *et al.* found a maximum speed for the jet of only ~ 15-20 cm s^{-1} . (For a summary of comparisons of the instantaneous results of Batteen *et al.* (1989) and Experiments 2, 3, 4, and 6, refer to Table III of Section IV.) The offshore region of Experiment 3 shows the development of equatorward flow, another feature absent from the model results of Batteen *et al.*. A vertical cross section of the alongshore average of the meridional velocity for day 40 (Fig. 3.12) shows the presence of a large undercurrent with a vertical extent of over 1000 m ($z \sim -1520 \text{ m}$). While the speed of the undercurrent (4 cm s^{-1}) correlates well with the work of Batteen *et al.*, the size of the undercurrent is nearly twice as large as the one seen at the end of their experimentation. Strong upwelling is exhibited in the surface temperature plot (Fig. 3.11c), with a core temperature in the coastal region of $11.5 \text{ }^\circ\text{C}$, the coldest of any of the 6 experiments. Isotherm deformation is seen throughout the water column for day 40 (Fig. 3.13). Nearshore, the upward bending of the isotherms is seen from ~ 320 m to surface, while the downward bending of the isotherms due to effects of the

undercurrent is seen all the way to ~ -1520 m. The extent of this downward deformation exceeds that of all other experiments run in this thesis as well as similar numerical model studies.

The zonal velocity time sequence shown in Figure 3.14 illustrates the eddy development over this experiment run. Day 40 (Fig. 3.14a) shows two eddies in the coastal region at $y \sim 256$ km and 320 km. These eddies enlarge, intensify and move southwest over the time sequence shown. Three additional eddies are seen forming on day 70 (Fig. 3.14c), including one in the offshore region ($x \sim 208$ km, $y \sim 480$ km). Figure 3.14d, day 80, completes the sequence showing the continued development of the eddies, with velocities of $\sim 10-15$ cm s⁻¹. These eddies differ from those in Batteen *et al.* (1989) in several respects. The eddies of Experiment 3 are larger, less densely populated and form further offshore. However, the zonal velocities of the two sets of eddies do correlate well.

The development of Experiment 3 continued as outlined above until the completion of the model run on day 95 (not shown). The meridional speed has continued to increase and is now at 45 cm s⁻¹. The upwelling region has also intensified extending offshore to ~ 320 km with a core temperature of 10 °C.

Clearly the inclusion of spatial variability in the far field has allowed for more development than was seen in constant wind stress forcing. This fact is primarily seen in the offshore equatorward and poleward flows, which were absent from Batteen *et al.* (1989). The greater extent and intensity of the undercurrent than that seen in Batteen *et al.* can be explained by the much stronger coastal jet which occurred in this

experiment and the compensatory increase in the intensity of the processes which drive the undercurrent.

2. Experiment 4

Experiment 4 utilized a wind stress forcing which was zonally constant but varied meridionally within 48 km of the coast. The offshore forcing still varied in x and y . As previously mentioned, this gives a variation in the alongshore stress, but causes the curl to equal zero in the critical nearshore region. This forcing is very similar to that of Batteen *et al.* (1989) of utilizing a meridionally varying stress function for the wind forcing throughout the domain.

The results of Experiment 4 were as expected. The curl-free stress in the nearshore region led to the establishment of a coastal jet, which extended offshore to the limits of the zonally constant forcing, ~ 48 km. Additionally, a narrow poleward surface current was formed offshore (~ 48 -96 km), and even further offshore (~ 96 -208 km) another equatorward current developed. All three of these alternating currents were relatively strong compared to the previous experiments. Day 40 (Fig. 3.15) clearly shows these strong well defined surface currents (Fig. 3.15b). The vertical alongshore averaged velocity plot (Fig. 3.16) shows the offshore currents extending to ~ 300 m, while the nearshore equatorward jet is surface trapped, less than 100 m deep with a weak undercurrent below it. The undercurrent may actually be contiguous with the poleward surface flow offshore. Upwelling is extremely strong, as seen in the temperature plot (Fig. 3.15c), having already reached a core temperature of 12 °C. As expected, the upwelling is preferentially developed in the region of maximum wind stress at the coast and has adopted a filamentous form which, a time sequence of

temperature fields (not shown) shows, is advected southwest. A vertical temperature cross section taken in the middle of the domain (Fig. 3.17) illustrates the breadth of the upwelling, with the upward deformation of the isotherms extending more than 150 km offshore. Like the coastal jet, the upwelling is relatively shallow, extending to only ~ 100 m, and shows no concomitant downwelling in the vicinity of the undercurrent. The first manifestation of mesoscale eddies is seen in the u field (Fig. 3.15a) near the coast at $y \sim 360$ km and 450 km at day 40. These eddies continue to develop until, by day 85, the u (Fig. 3.18a) field shows three distinct eddies formed in the coastal region between $y \sim 384$ km to 512 km.

The experiment was terminated on day 110 (Fig. 3.19) of the model run. Little change has actually occurred in the gross structure of the domain since day 85. While the offshore flows have strengthened, the equatorward jet has weakened. However, the eddies are still present and exhibit a strong effect on the upwelling signature as the cold water is advected by the cyclonic and anticyclonic circulation of the eddies. This advection gives the temperature front a distinctive wave-like appearance. The alongshore vertical cross section (Fig. 3.20) for this day shows the coastal jet to still be relatively shallow, but shows the offshore flows to have deepened to 520 m. Current vector plots for days 40 and 110 (Fig. 3.21) illustrate the surface flow pattern. On day 40 (Fig. 3.21a), the current structure was strongly equatorward at the coast, with westward flow throughout the offshore region. By day 110 (Fig. 3.21b), the nearshore flow is both equatorward and poleward but is predominantly poleward. The offshore flow is strongest in the middle of the domain and is

equatorward. The appearance of two gyre-like circulations at the southern and northern regions of the model can also be seen.

These results can be compared to those obtained by Batteen *et al.* (1989). Although the eddies were more densely grouped and more numerous in Batteen *et al.*, they otherwise compare closely to those generated in this experiment. The primary difference in the two experiments lies in the offshore region. While Batteen *et al.* had a simplistic quiescent region offshore, Experiment 4 developed a strong, well-defined equatorward flow, with poleward flow further out. This difference is primarily due to the increased diversity of the offshore wind forcing of Experiment 4. Consistent with Batteen *et al.* (1989), both Experiments 3 and 4 reinforce the conclusion that curl-free wind stress forcing in the nearshore region leads to the development of a coastal jet and undercurrent and eddies.

3. Experiment 5

Experiment 5 is the first of the climatological wind stress forcing experiments with two dimensional forcing throughout the entire model domain. The structure in the nearshore region varies in both x and y , and there is a positive wind stress curl along the coast.

Day 10 of the model run (Fig. 3.22) is in many respects similar to day 5 of Experiment 2 (Fig. 3.2). The equatorward coastal jet is well developed, extending southward to $y \sim 200$ km, and has a maximum speed of 10 cm s^{-1} . The poleward surface flow at the coast is already evident with a speed of 4 cm s^{-1} . The alongshore averaged velocity plot (Fig. 3.23) depicts an equatorward jet overlaying a poleward undercurrent in the nearshore region. The undercurrent is weak ($\sim 2 \text{ cm s}^{-1}$) and

relatively small. Offshore Ekman transport due to the wind stress is seen on day 10 (Fig. 3.22a) and a cold water region is present in the coastal region (Fig. 3.22c). The position of maximum upwelling at $y \sim 300$ km coincides with the region of maximum wind stress near the coast (refer to Fig. 2.4). The pressure field similarly exhibits a negative perturbation in this same region (Fig. 3.22d). The vertical cross shore plot of temperature (Fig. 3.24) exhibits the upward bending of isotherms in the coastal region, consistent with upwelling. However, a noticeable bending downwards of the isotherms in the region of the undercurrent is not seen, indicative of the weakness of this current.

By day 20 (Fig. 3.25), the poleward surface flow (Fig. 3.25b) is well established and has moved up the coast to $y \sim 300$ km. Additionally, the speed of the flow has increased to 8 cm s^{-1} . The equatorward jet shows the opposite trend, having been pushed back up the domain decreasing to 4 cm s^{-1} . The offshore equatorward flow is beginning to develop in the region ~ 100 km to 190 km off the coast. The coolest temperature (Fig. 3.25c), indicative of upwelling develops in the area of maximum coastal wind stress and develops a meandering filamentous form. The strong poleward flow in the southeastern corner of the domain has begun to drive offshore Ekman flow (Fig. 3.25a) and warmer temperatures indicating downwelling are seen in this area. A cross shore averaged velocity plot for this day (Fig. 3.26) and shows the poleward current dominating the coastal region. This coastal flow is well defined in the average to 520 km.

The filament continues to grow and to be advected in a southwesterly manner so that by day 40 (Fig. 3.27) it extends off the coast out to 190 km (Fig.

3.27c). The filament continues to develop in the high wind stress region nearshore as seen by the small core of $13\text{ }^{\circ}\text{C}$ at $y \sim 384$ (Fig. 3.27c). Offshore Ekman flow (Fig. 3.27a) is found throughout the model except for the downwelling region in the south where relatively strong onshore flow is discernible. The poleward coastal flow now dominates the nearshore region and has reached a speed of 14 cm s^{-1} . The equatorward flow offshore has also become more defined with a speed of 12 cm s^{-1} in the northern region.

Development of this form continues with the filament reaching its maximum extent of 240 km on day 55 (Fig. 3.28) before starting to dissipate. By day 80 (Fig. 3.29), the filament has completely disappeared and in its place is a broad band of upwelled water, as seen in the northern part of the model domain (Fig. 3.29b). The downwelling region in the south now extends to $y \sim 320\text{ km}$ and has a core of $16\text{ }^{\circ}\text{C}$. The coastal flow is poleward at 16 cm s^{-1} (Fig. 3.29b), while the offshore equatorward flow is much better defined than at day 40 with a core of 20 cm s^{-1} . The alongshore averaged velocity (Fig. 3.30) shows the poleward flow extending down to 720 m depth, while the equatorward current offshore is very broad and descends to 520 m depth. A temperature section in the middle of the domain (Fig. 3.31) upward bending of isotherms in the nearshore upwelling region as well as a clearly defined temperature anomaly offshore where the cross section cuts through an offshore protrusion of the upwelling region. This figure illustrates the strong frontal nature of the filaments in the surface region.

The simulation was run to day 110 (Fig. 3.32). The downwelling signal has advanced to $y \sim 350$ and has a strong northward propagation. The upwelling has

decreased in intensity to 13 °C and has become confined to the coast. There is a protrusion of cold water from the north which appears to be advected southward by the mean alongshore flow, but this cold water does not show signs of intensification over the last few days of the model run. A cross-sectional temperature plot (Fig. 3.33) again shows the characteristic isotherm bending in several locations in the domain. The pressure field (Fig. 3.32d) shows a small eddy starting to develop at $x \sim 256$ km and $y \sim 512$ km. This location is coincident with the boundaries of the offshore equatorward flow and a poleward flow forming further offshore. This would seem to indicate that the eddy generation is a result of the strong horizontal shear, and subsequent barotropic instability, in this region. The alongshore averaged velocity (Fig. 3.34) still shows the same pattern as on day 80 with a deepening of the poleward flow to 820 m and the offshore flow to 720 m.

The current vector sequence of Figure 3.35 shows the progression in the surface current flow. The shift from equatorward flow dominating at the coast on day 20 (Fig. 3.35a), to the strong poleward surface flow in the coastal flow with equatorward flow offshore on day 110 (Fig. 3.35d), is clearly seen. It is interesting to note the offshore flow and the development of the gyre-like circulation, which is shown to be clockwise in the bottom right portion of the model domain and counterclockwise in the upper left.

The additional diversity in the nearshore wind field of Experiment 5 has led to a cessation of cyclonic / anticyclonic eddy generation in the nearshore region, but a filament was formed. The lack of eddies is probably a result of no strong coastal jet / undercurrent structure. The equatorward wind stress is not strong enough to

maintain a coastal jet in face of the strong positive wind stress curl at the coast. The filament formation seems to be a consequence of upwelling occurring preferentially in the area of maximum equatorward wind stress at the coast with a subsequent advection of this cold water offshore.

C. TWO TENTHS DEGREE CLIMATOLOGICAL WIND FORCING

1. Experiment 6

Experiment 6 utilized two tenths degree resolution climatological wind stress forcing. This fine-scale resolution added a great deal of structure to the wind field, specifically in the nearshore region. Of particular note is the region of maximum southerly stress and negative wind stress curl at approximately 400 km (Fig. 2.6).

Experiment 6 was by far the most dynamically active and realistic simulation of the six experiments. By day 5 (Fig. 3.36), a strong equatorward jet in the nearshore region had set up (Fig. 3.36b), and an offshore Ekman transport has been established (Fig. 3.36a). The peak velocities of the equatorward surface jet, of $\sim -22 \text{ cm s}^{-1}$, coincided with the location of maximum southward stress values at the coast, which resulted in a negative wind stress curl region. It is interesting to note that while at day 5 in Experiments 2 through 5 the core of the equatorward jet extended along the entire alongshore extent of the model domain, Experiment 6 showed a preferential development and confinement of the equatorward current core to the north. As previously highlighted in the wind field description (Section I.A.3), this area is located at the climatologically maximum wind stress values found at Cape Mendocino (Nelson, 1977). As expected, examination of the u (Fig. 3.36a) field also shows a maximum

offshore transport at the coast at $y \sim 400$ km. The temperature field for day 5 (Fig. 3.36c) depicts the first development of a cold core filament at $y \sim 400$ km, just south of the equatorward flow maximum.

Day 10 (Fig. 3.37) delineates the continued development of offshore transport (Fig. 3.37a) and a strengthening of the equatorward jet to ~ 26 cm s⁻¹ (Fig. 3.37b). The jet is confined to a region within approximately 40 km of the coast, while the core is located only a few kilometers from the shore. As seen in previous experiments, a coastal surface poleward flow has developed and has progressed southward in the southern portion of the domain. An alongshore average of the v field (Fig. 3.38) shows that the dominant flow pattern is that of an equatorward jet overlying a weak but well defined undercurrent. These locations represent areas of potential baroclinic instability due to the vertical shear exhibited. A filament has also developed and has a core temperature at day 10 of -13 °C, with an offshore extent of 48 km (Fig. 3.37c). Two opposing surface currents have formed as a result of the diversity in the wind field and the resulting convergence has advected the cold upwelled water offshore. Figure 3.39 shows a vertical cross section of the instantaneous temperature contours for a location approximately equal to the filament core ($y \sim 390$ km). The bending upward of the temperature contours is clearly indicative of an upwelling regime. The upwelling is confined to a region within 150 meters of the surface which agrees well with the vertical extent and influence of the equatorward jet at this time and location (Fig. 3.40). Day 10 marks the beginning of strong, observable eddy development in the nearshore region. The pressure field (Fig. 3.37d), shows a cyclonic eddy forming at approximately 420 km. By day 10, there is both poleward and

equatorward flow at the surface in the nearshore region, with some manifestation of an undercurrent at various locations throughout the domain. Additionally, there is strong evidence of both filament and eddy developments. By day 20, the alongshore averaged velocity field (Fig. 3.41) shows no evidence of an undercurrent. A poleward surface flow dominates the nearshore region. Although some evidence can be found for a weak undercurrent in the northern portion of the model domain (Fig. 3.42), the model as a whole is developing predominantly surface intensified features.

The pressure field of day 25 (Fig. 3.43d) shows four eddies. There is a dipole eddy with an axis at $y \sim 384$ km, an anticyclonic eddy at $y \sim 176$ km offshore, and a cyclonic eddy at $y \sim 448$ km. These offshore eddies have been formed in areas of strong horizontal shear between opposing surface currents, as seen in a comparison of the pressure (Fig. 3.43d) and meridional velocity (Fig. 3.43b) fields for day 25. The cold core filament (Fig. 3.43c) now extends to 160 km offshore and exhibits a hammerhead shape coincident with the axis of the dipole eddies.

By day 40 (Fig. 3.44) the nearshore poleward flow extends along the entire coast (Fig. 3.44b). Equatorward flow is still manifested in the alongshore region from $y \sim 384$ km to 520 km. The equatorward jet is clearly defined, extending offshore to ~ 60 km and having a peak velocity of 25 cm s^{-1} . An undercurrent is very weakly seen in the region under the equatorward jet, but strong poleward surface flow is seen in the nearshore region (Fig. 3.45). The filament now extends offshore to 192 km as a result of advection a southwest direction (Fig. 3.44c). The core temperature of the filament remains at 13°C with a location at $y \sim 400$ km in the alongshore direction. A vertical temperature section (Fig. 3.46) still shows shallow upwelling at the coast,

but offshore there is evidence of the filament at $x \sim 125$ and 210 km. The eddies that developed earlier are still present, but an additional cyclonic eddy has formed just north of the anticyclonic eddy that formed at $y \sim 176$ km offshore (Fig. 3.44d).

By day 45 (not shown) there is no evidence of an undercurrent below the equatorward jet. The model flow field exhibits strong alternating poleward / equatorward surface flow. This pattern persists through the remainder of the 120 days of the model run. The anticyclonic nearshore eddy remains stationary and well-defined. The cyclonic eddy in the nearshore region is slowly absorbed by the nearshore large scale pattern and has lost its identity by day 55 (not shown). The nearshore region has two large cyclonic gyres with anticyclonic eddy located near the shore at $y \sim 440$ km. The offshore eddies are advected to the southwest. Their size and structure, as well as the structure in the nearshore region, is seen in the pressure field of day 80 (Fig. 3.47d). Day 80 (Fig. 3.47) also illustrates the flow pattern that is characteristic of the remainder of the model run. From the coast to approximately 128 km offshore, poleward surface flow dominates (Fig. 3.47b). However, within this poleward current is a pocket of strong equatorward with speeds of 25 cm s^{-1} from 128 km to 190 km. The offshore equatorward flow has a speed of 20 cm s^{-1} . The filament has reached an offshore extent of 288 km (Fig. 3.47c).

The pressure field at day 100 (Fig. 3.48d) shows another anticyclonic eddy developing at $y \sim 512$ km and approximately 320 km offshore. Again this is an area of strong horizontal shear between two opposing surface currents (Fig. 3.48b).

The model was run to day 120 (Fig. 3.49). The equatorward coastal flow has increased in speed to 40 cm s^{-1} , but is confined to ~ 45 km from the coast (Fig.

3.49b). The poleward surface flow near shore is relatively weak with only isolated pockets exceeding 20 cm s^{-1} . The offshore equatorward flow has also weakened to less than 15 cm s^{-1} throughout most of its extent. The extremities of the cold core filament have fragmented and been absorbed, while the offshore limit of the filament (Fig. 3.49c) has regressed to 256 km from its maximum extent of 320 km at day 95. Six eddies are present in the domain, three cyclonic and three anticyclonic, in an area extending from the coast to 320 km offshore (Fig. 3.49d). These eddies continue to develop in areas of strong horizontal shear.

In summary, the development of a confined equatorward jet with an undercurrent is initially seen in Experiment 6. The remaining nearshore region has poleward surface flow. The offshore region is primarily equatorward, with various regions of poleward surface flows. Eddies develop first in the area of the negative curl near the coast and later in the areas of horizontal shear offshore. The temperature structure exhibits a cold core filament which develops at the convergence of negative and positive curl near the coast. Throughout the experiment the eddies continue to develop, the filament continues to grow, and the surface currents become more defined. The undercurrent disappears so that the current regime has surface currents only.

Whereas in Experiment 5 the filament appeared to be the result of preferential upwelling and strong offshore advection, in Experiment 6 the filament forms and grows as a result of a surface current convergence. The diversity of the wind structure causes the formation of these opposing surface currents. These currents converge and advect the cold, upwelled water offshore in a plume. Once offshore the plume is advected southwesterly by the mean flow. The strong filament formation emphasizes

the importance of fine scale diversity in the wind field for the development of both current and mesoscale features in the CCS.

D. STABILITY ANALYSIS

One of the primary motivations of this research was to investigate the energetics of eddy formation in the CCS. Both baroclinic and barotropic instability mechanisms have been shown to be instrumental in the production of eddies (Robinson, 1983). Evidence for both baroclinic and barotropic instability has been given for the northeast Pacific (Wright, 1980). Evidence for baroclinic instability alone has been given for the northern portion of the CCS (Emery and Mysak, 1980; Thomson, 1984; Freitag and Halpern, 1981). The baroclinic instability which occurs as a result of the equatorward jet over the undercurrent has been hypothesized by Ikeda and Emery (1984) to be the primary mechanism for meander growth and eddy development. The importance of barotropic instability is less clearly documented with only a few studies showing evidence in support of this mechanism operating in the CCS (Robinson *et al.*, 1985; Thomson, 1984).

There are many ways to both qualitatively and quantitatively describe the energy transfer processes which lead to the development and growth of mesoscale phenomena. On the most basic level, the velocity shear in the region of development is indicative of the form of instability occurring. As a first approximation, areas of strong horizontal shear are considered to have the potential for barotropic instability, while areas of strong vertical shear are considered to have the potential for baroclinic instability (Pond and Pickard, 1983). Beyond the simple qualitative shear observations, instability is also characterized in the potential vorticity patterns of the flow fields.

Watts (1983) and Watts and John (1982) were able to characterize the instability of the Gulf Stream region through analysis of the potential vorticity fields of the area. Two necessary conditions of baroclinic instability are that the cross stream derivative of potential vorticity change sign in the domain and that the mean velocity times the potential vorticity gradient be positive somewhere in the model field. A final method of analysis involves actual computation of the energy transfer terms. This method has been used extensively by Semtner and Mintz (1977) in their Gulf Stream study and by Han (1975) in his study of mesoscale eddies. This latter technique is particularly helpful in quantifying the relative contributions of the two instability processes.

Of the four experiments (Exps. 3-6) which showed eddy development, Experiments 5 and 6 were chosen for more in-depth energy analyses. Since Experiments 3 and 4 closely followed the energy analyses as discussed by Batteen *et al.* (1989), they will not be discussed here.

1. Experiment 5

Eddy development occurred very late in Experiment 5 at ~ day 110. These eddies developed far offshore and were relatively small. Horizontal shear was prevalent in the area of the initial development leading to the hypothesis that a barotropic instability process was the dominant mechanism.

In accordance with the work done by Watts (1983), potential vorticity was computed in the cross shore direction using the following equation:

$$q \sim (f + \zeta) \frac{\partial T}{\partial z} - \frac{\partial T}{\partial x} \frac{\partial v}{\partial z}, \quad (3.1)$$

where
$$\zeta = \frac{\partial v}{\partial x} - \frac{\partial u}{\partial y} . \quad (3.2)$$

Utilizing the above formulations, the time-averaged cross-stream derivative of potential vorticity ($\partial\zeta / \partial x$) was calculated and plotted for the period 90 to 99 days (Fig. 3.50). This time period was chosen as the period during which generation occurred. From the plot, one can see that sign changes occur both in the vertical in the nearshore region and in the horizontal in the offshore region. Although this shows that eddy generation is possible in the coastal region due to baroclinic instability, no such eddies are seen in that area. The forcing is not strong enough to produce the eddies which are seen in Experiments 3 and 4. In the region of offshore eddy generation, barotropic instability is in evidence (Fig. 3.50).

2. Experiment 6

Eddy development in this experiment appears to fall into more than one spatial and temporal frame. Initially, the nearshore eddies in the location of the equatorward jet occurred at day 10, early in the model run. Somewhat later in the model development at day 25 and much later at day 100, offshore eddies developed. For simplicity, these two classes of nearshore and offshore eddies will be addressed separately.

As described previously (Section III.C.1), strong vertical shear persists in the region of the equatorward jet up until day 45. This vertical shear is located in a region coincident with the formation of the first anticyclonic eddy ($y \sim 420$ km). This characterizes the nearshore eddy generation during the early portion of the experiment as being due to baroclinic instability.

The time-averaged cross-stream derivative of potential vorticity ($\partial\zeta / \partial x$) was calculated and plotted for the period 5 to 15 days (Fig. 3.51). This time frame was chosen to coincide with the period of initial nearshore eddy development. Examination of Figure 3.51 clearly reveals a vertical sign change of the potential vorticity gradient in the region of the nearshore coastal jet and the underlying undercurrent ($z \sim 75$ m). A sign change is also seen in the horizontal in the boundary region between opposing currents just offshore ($x \sim 75$ km). Visual comparison of the potential vorticity gradient with the average alongshore velocity (Fig. 3.24), shows several areas in both the nearshore and offshore regions noted above where the product of the two fields is greater than zero. It should be noted that the vertical v field in Experiment 6 is extremely diverse so that different instantaneous cross sections of v varied tremendously throughout the domain. In particular, there are many areas of positive products of the fields of v and vorticity which fail to show up when alongshore averaged velocity fields are used. Nonetheless, based on this method of analysis, the necessary conditions for baroclinic instability are well satisfied. Barotropic instability as denoted by the horizontal sign change in vorticity gradient is also evident, but to a lesser extent.

A time series of kinetic energy for Experiment 6 is shown in Figure 3.52. It is seen from this figure that there are three phases to the kinetic energy development in the model. There is an initial period of change in the kinetic energy from the start of the experiment to day 12. This period coincides with the development of the initial eddies in the nearshore region. A second period of change in the kinetic energy occurs between 12 and 100 days. This period is demarcated by a strong near linear increase

in kinetic energy throughout the model domain. A final period is illustrated in the leveling off of kinetic energy after day 100 until the completion of the experiment on day 120. If it is assumed that the level periods at the start and end of the experiment represent quasi-steady state situations, actual values for the energy transfer process can be computed (Semtner and Mintz, 1977; Han, 1975).

Utilizing analysis techniques formulated by Rutherford (1989) based on Han (1975) and Semtner and Mintz (1977), the energetics were computed for the period of 1 to 12 days. The computed values along with the directions of energy transfer are shown in Figure 3.53. Transfer of energy from eddy potential energy (EPE) to eddy kinetic energy (EKE) represents baroclinic instability, while mean kinetic energy (MKE) transfer to EKE indicates a barotropically unstable process (Semtner and Mintz, 1977). While both processes are illustrated in Figure 3.53, the baroclinic instability term is nearly twice as large as the barotropic term so that it is the dominate instability mechanism over the first 12 days. It should be noted that these calculations were made over the entire model domain, including the relatively inactive offshore region, which account for the seemingly low energy and transfer values in Figure 3.53.

It is clearly seen that the initial period of Experiment 6 is dominated by baroclinic instability. This is shown by the vertical shear in the velocity field, by the sign change in the cross shore potential vorticity derivative, and by these energy calculations. All of these indicators are strongest in the area of eddy generation in the nearshore region. Barotropic instability is also seen, but it does not appear to be as strong as baroclinic instability during the beginning phases of the experiment.

The offshore eddies which appear later in the experiment at ~ days 25 and 100 exhibit different instability characteristics. As mentioned in the results section (Section III.C.1), these eddies initially appeared in areas of strong horizontal shear, specifically at the boundary between the offshore equatorward flow and the poleward surface currents. Horizontal shear indicates a barotropic instability process. Figure 3.54, $\partial q / \partial x$, shows a horizontal change in the potential vorticity gradient. However, a vertical sign change seen is not discernible. An energy analysis was made for this quasi-steady period of 100 to 120 days, and the results are shown in Figure 3.55. It is seen in this figure that not only has the barotropic instability component increased, but the baroclinic component has decreased by a whole order of magnitude. Clearly a change in instability processes has occurred with a shift to the dominance of barotropic instability.

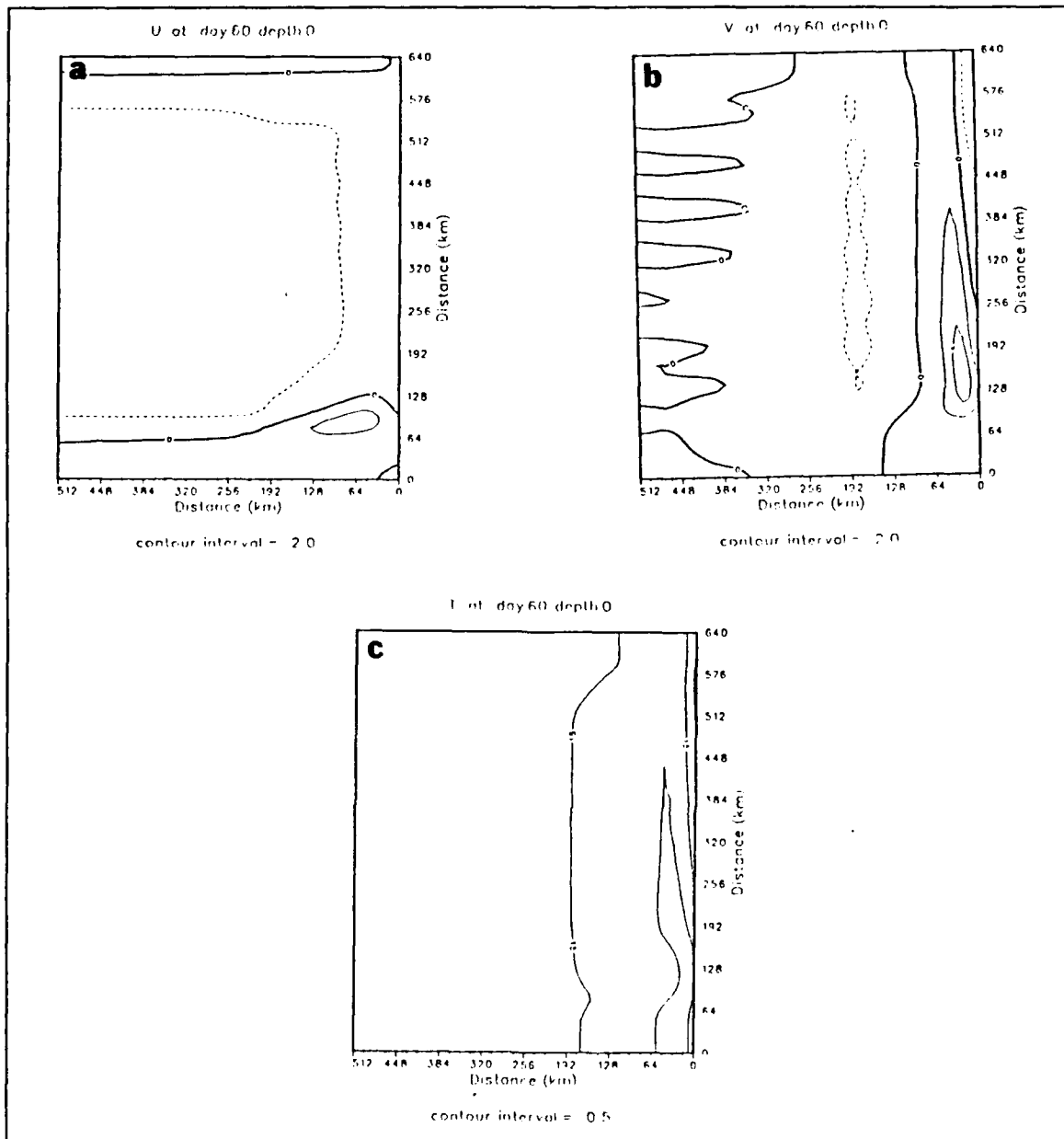


Figure 3.1 Surface isopleths of (a) zonal (u) velocity (cm s^{-1}), (b) meridional (v) velocity (cm s^{-1}), and (c) temperature ($^{\circ}\text{C}$) for Experiment 1 at day 60. Contour interval is 2.0 cm s^{-1} for (a) and (b), and $0.5 \text{ }^{\circ}\text{C}$ for (c). Dashed contours denote offshore velocities in (a) and equatorward velocities in (b).

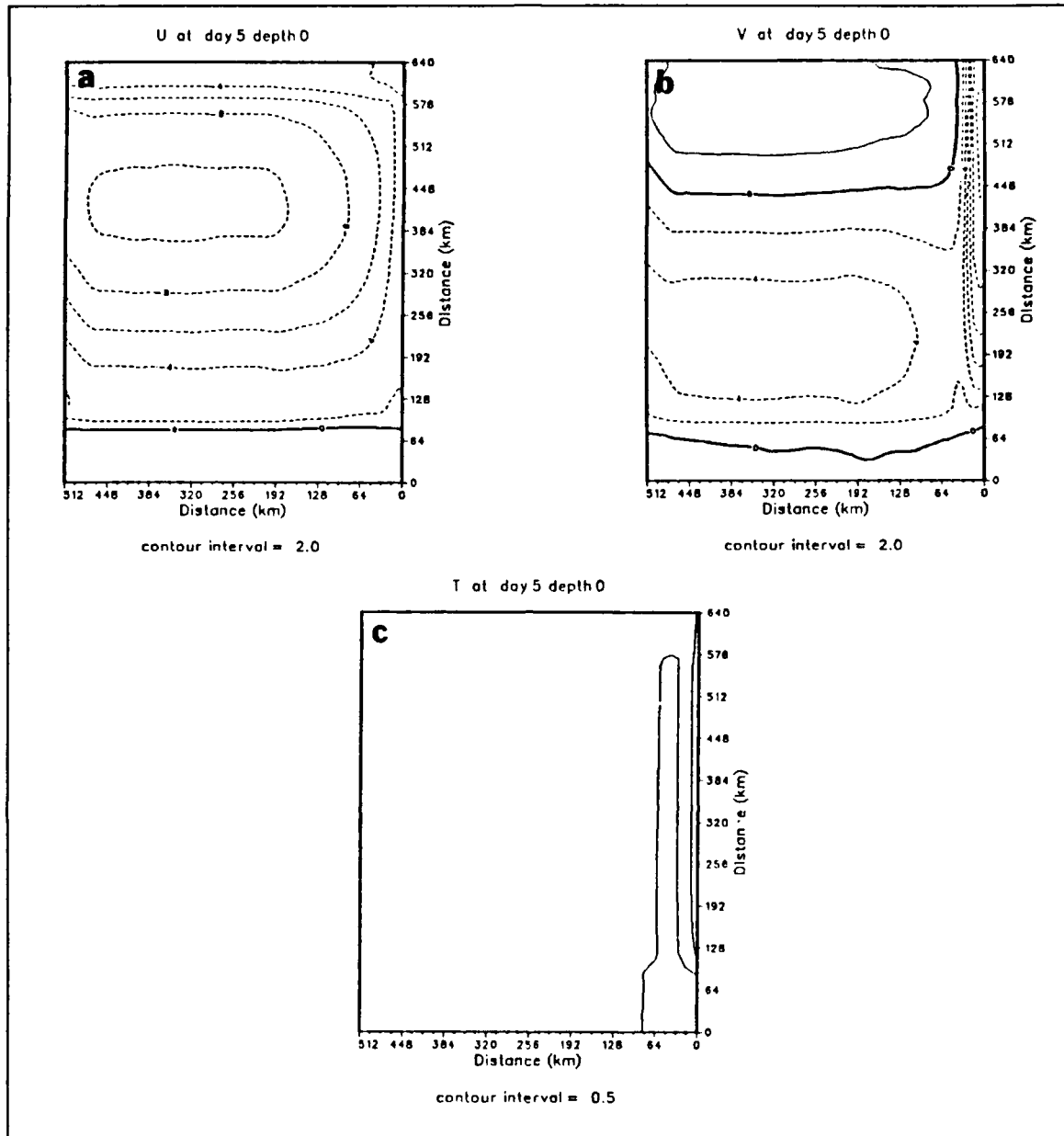


Figure 3.2 Surface isopleths of (a) zonal (u) velocity (cm s^{-1}), (b) meridional (v) velocity (cm s^{-1}), and (c) temperature ($^{\circ}\text{C}$) for Experiment 2 at day 5. Contour interval is 2.0 cm s^{-1} for (a) and (b), and $0.5 \text{ }^{\circ}\text{C}$ for (c). Dashed contours denote offshore velocities in (a) and equatorward velocities in (b).

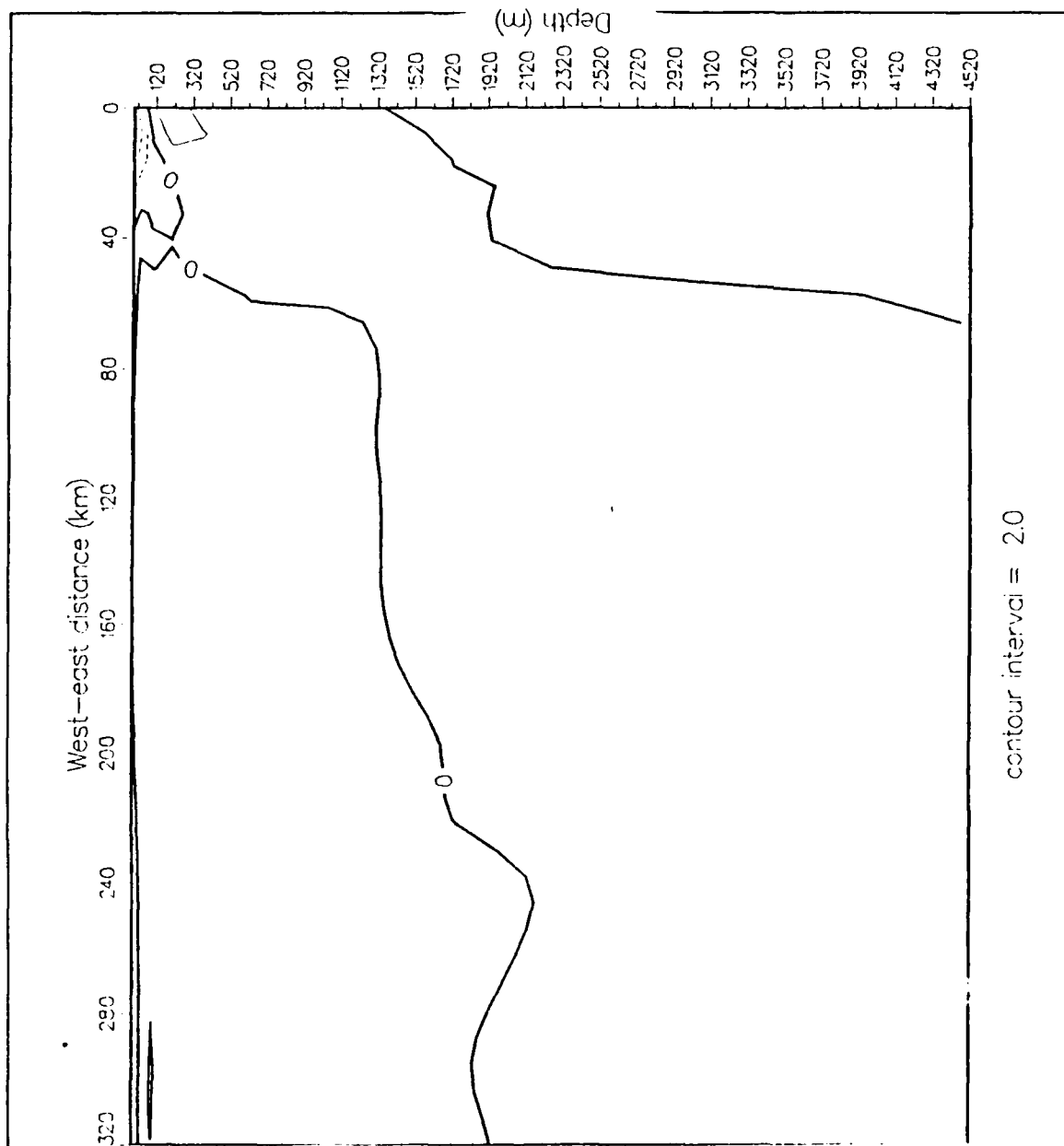


Figure 3.3 Vertical cross-shore section of meridional (v) velocity (cm s^{-1}) for Experiment 2 at day 10. Contour interval is 2.0 cm s^{-1} . Dashed contours denote equatorward velocities. The vertical cross section was alongshore-averaged.

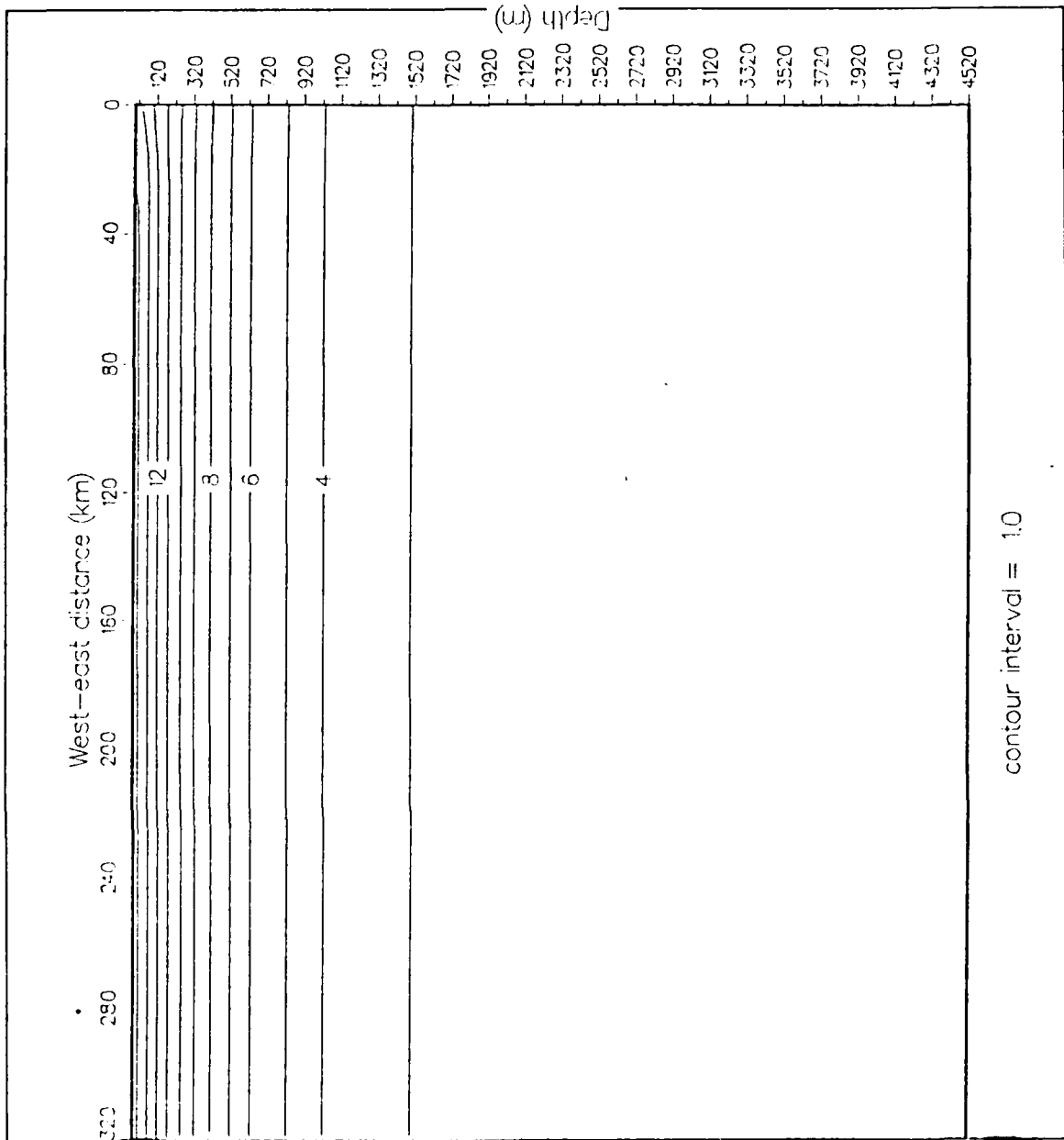


Figure 3.4 Vertical cross-shore section of temperature ($^{\circ}\text{C}$) for Experiment 2 at day 10. Contour interval is 1.0°C . The vertical cross-section was taken at $y = 290$ km.

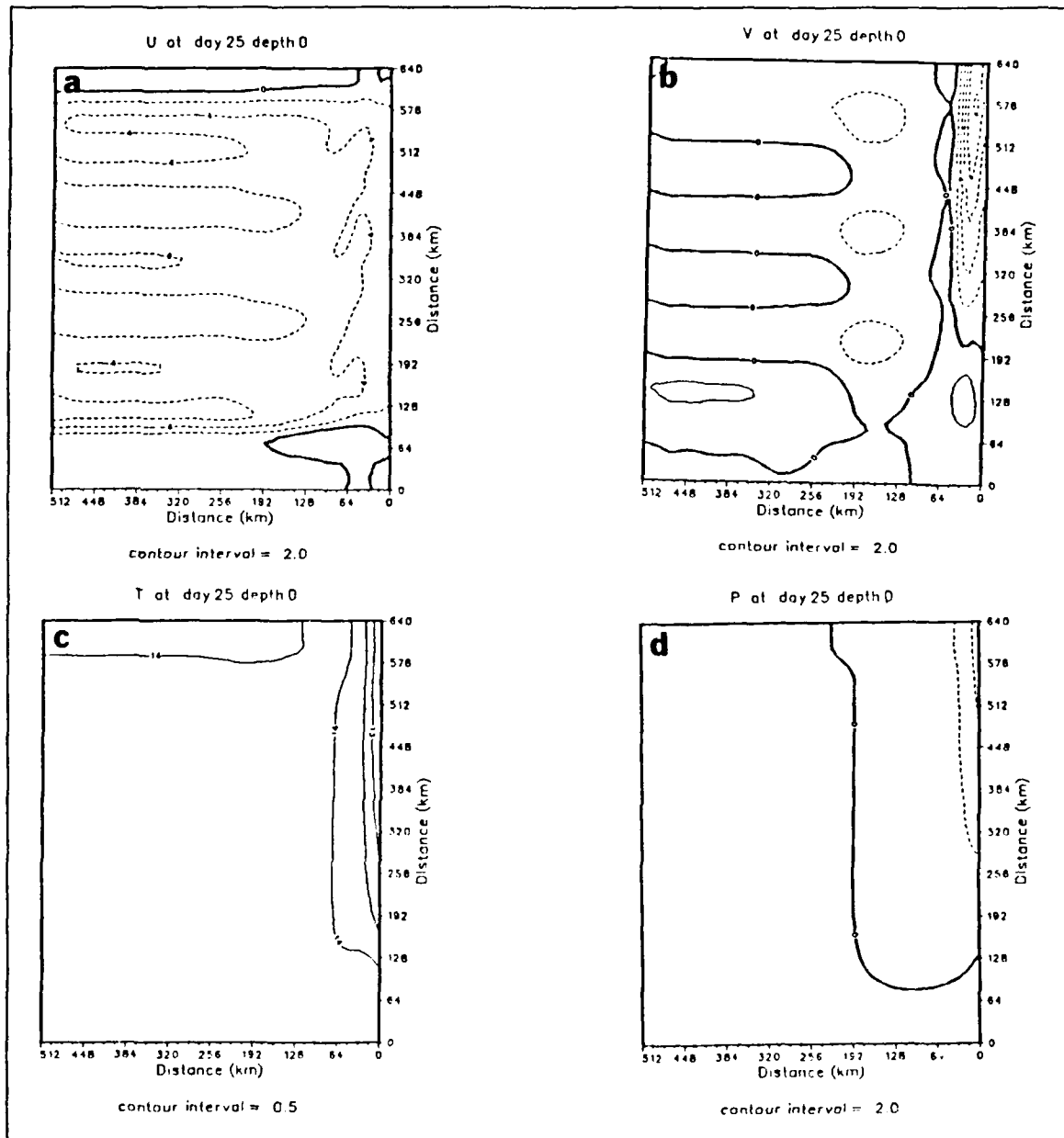


Figure 3.5 Surface isopleths of (a) zonal (u) velocity (cm s^{-1}), (b) meridional (v) velocity (cm s^{-1}), (c) temperature ($^{\circ}\text{C}$), and (d) dynamic height (cm) relative to 2400 m for Experiment 2 at day 25. Contour interval is 2.0 cm s^{-1} for (a) and (b), 0.5 $^{\circ}\text{C}$ for (c) and 2.0 cm for (d). Dashed contours denote offshore velocities in (a), equatorward velocities in (b) and negative values relative to 2400 m in (d).

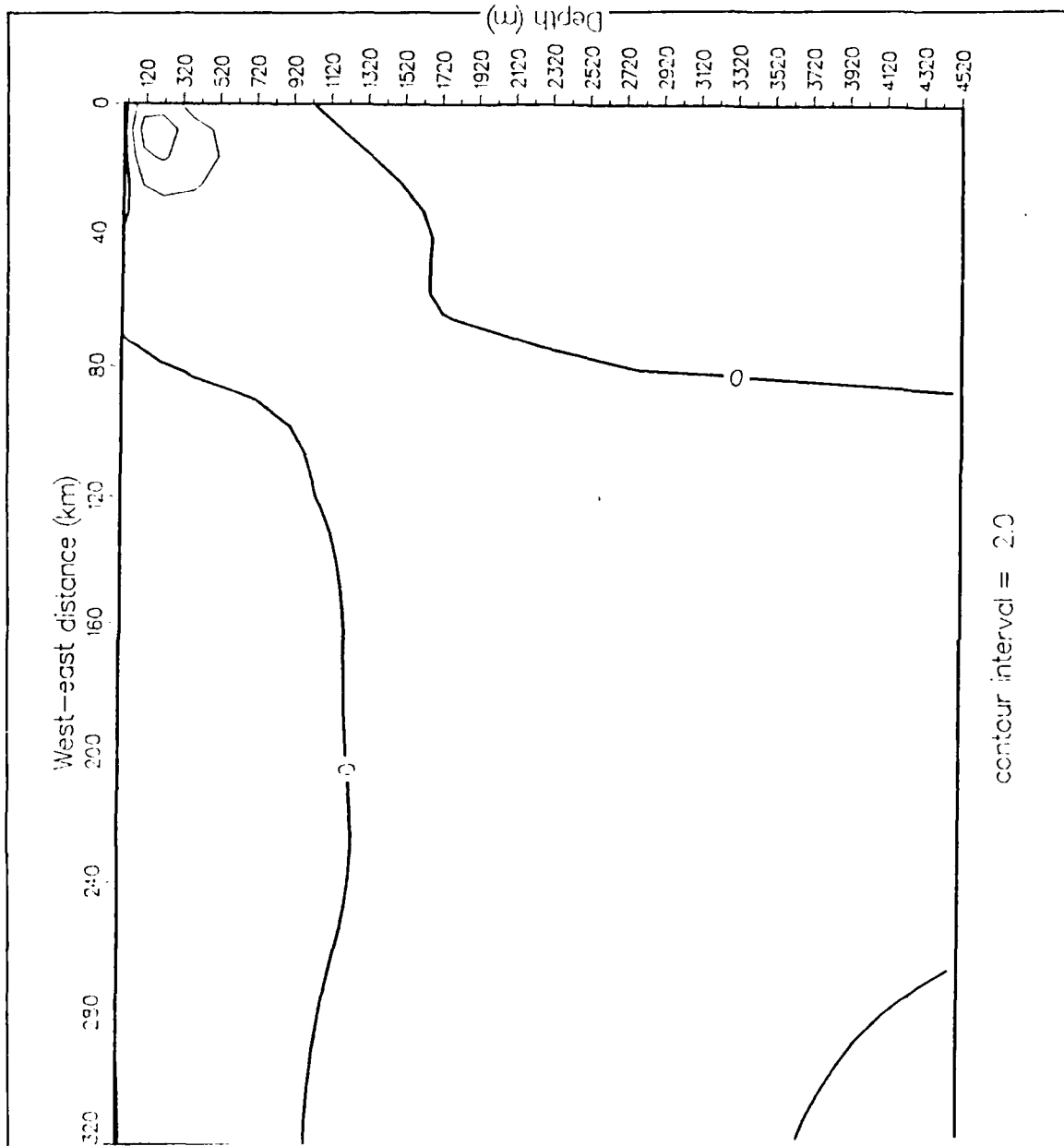


Figure 3.6 Vertical cross-shore section of meridional (v) velocity (cm s^{-1}) for Experiment 2 at day 30. Contour interval is 2.0 cm s^{-1} . Dashed contours denote equatorward velocities. The vertical cross section was alongshore-averaged.

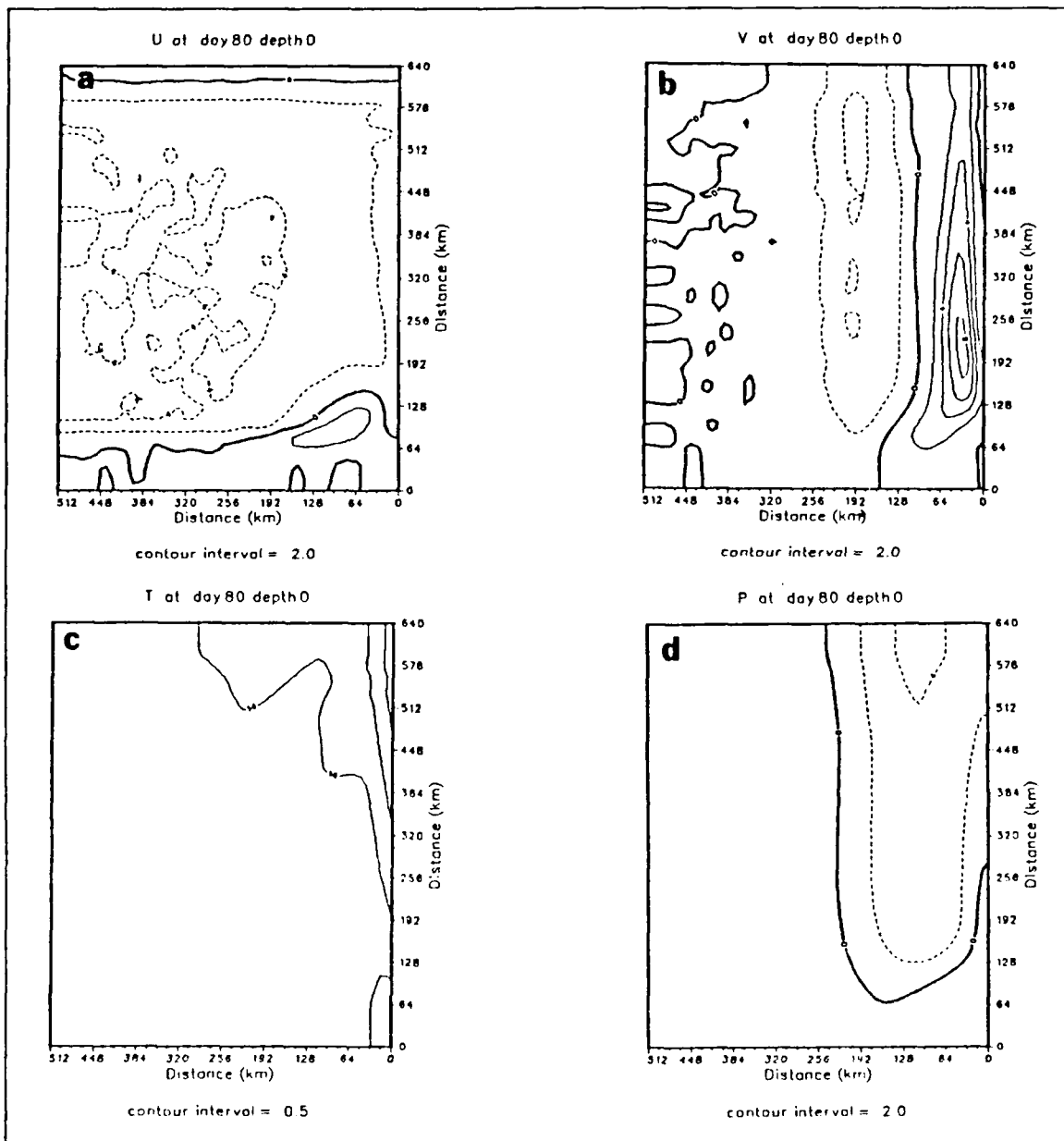


Figure 3.7 Surface isopleths of (a) zonal (u) velocity (cm s^{-1}), (b) meridional (v) velocity (cm s^{-1}), (c) temperature ($^{\circ}\text{C}$), and (d) dynamic height (cm) relative to 2400 m for Experiment 2 at day 80. Contour interval is 2.0 cm s^{-1} for (a) and (b), 0.5 $^{\circ}\text{C}$ for (c) and 2.0 cm for (d). Dashed contours denote offshore velocities in (a), equatorward velocities in (b) and negative values relative to 2400 m in (d).

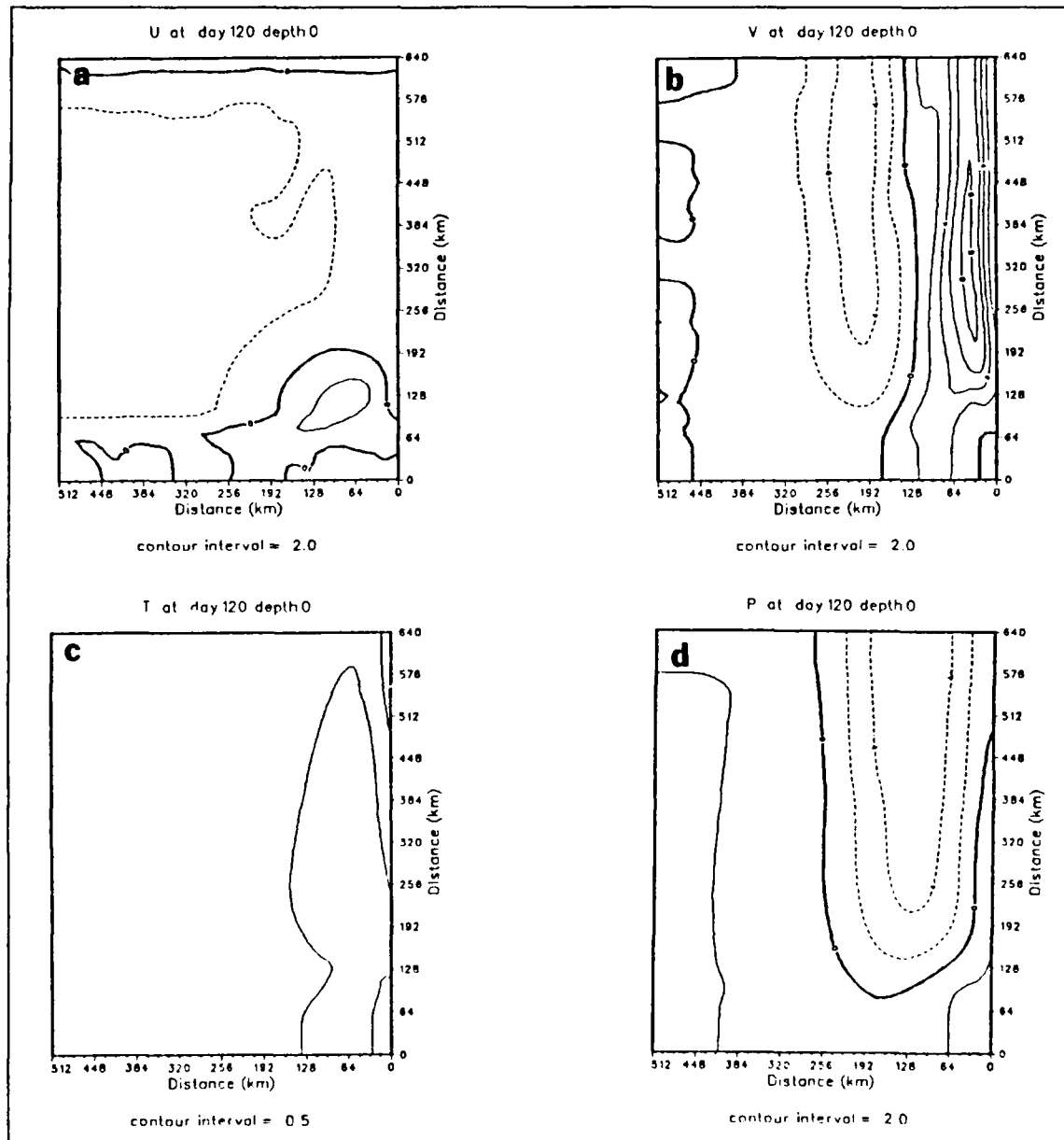


Figure 3.8 Surface isopleths of (a) zonal (u) velocity (cm s^{-1}), (b) meridional (v) velocity (cm s^{-1}), (c) temperature ($^{\circ}\text{C}$), and (d) dynamic height (cm) relative to 2400 m for Experiment 2 at day 120. Contour interval is 2.0 cm s^{-1} for (a) and (b), $0.5 \text{ }^{\circ}\text{C}$ for (c) and 2.0 cm for (d). Dashed contours denote offshore velocities in (a), equatorward velocities in (b) and negative values relative to 2400 m in (d).

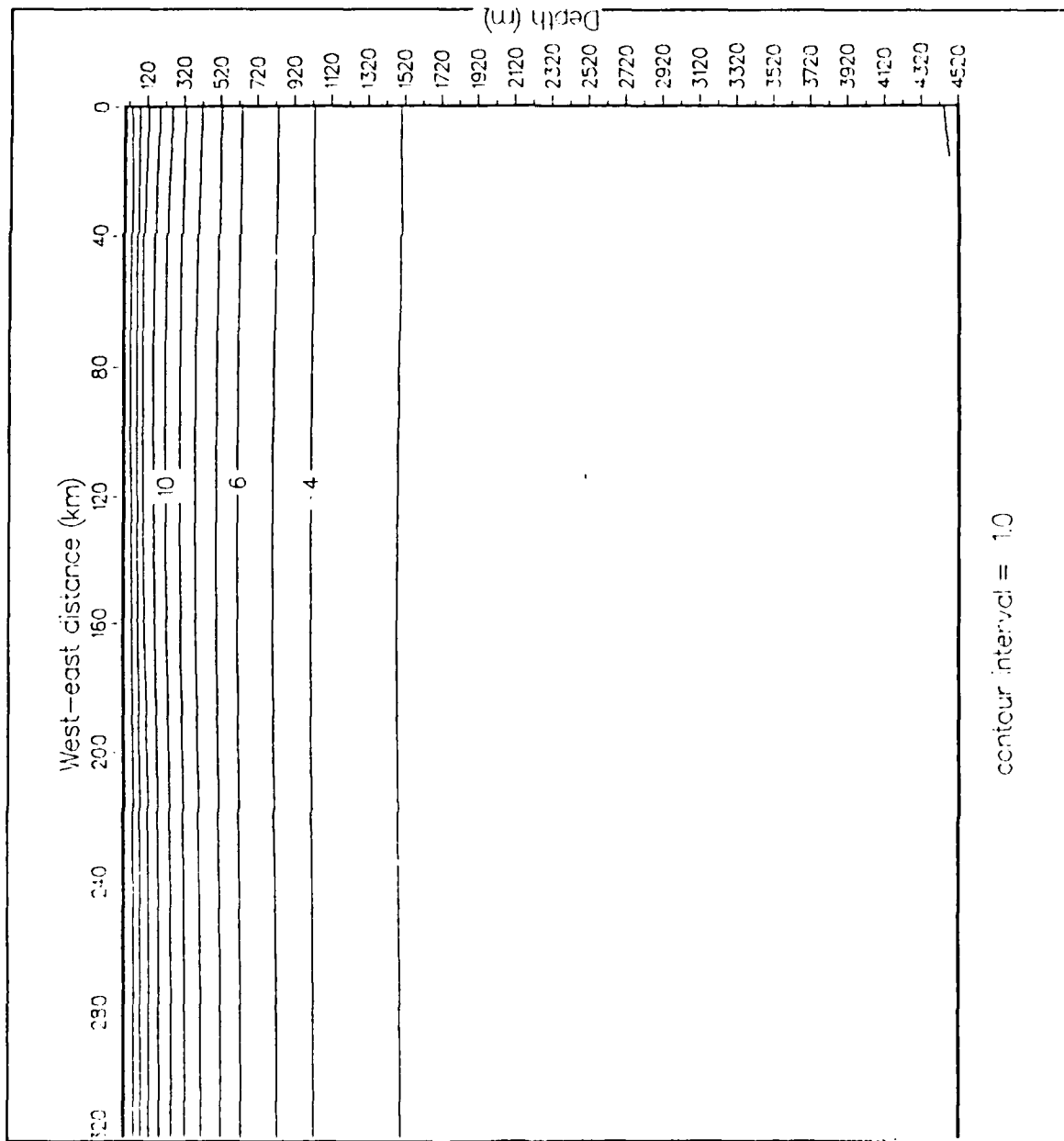


Figure 3.9 Vertical cross-shore section of temperature ($^{\circ}\text{C}$) for Experiment 2 at day 120. Contour interval is 1.0°C . The vertical cross-section was taken at $y = 290$ km.

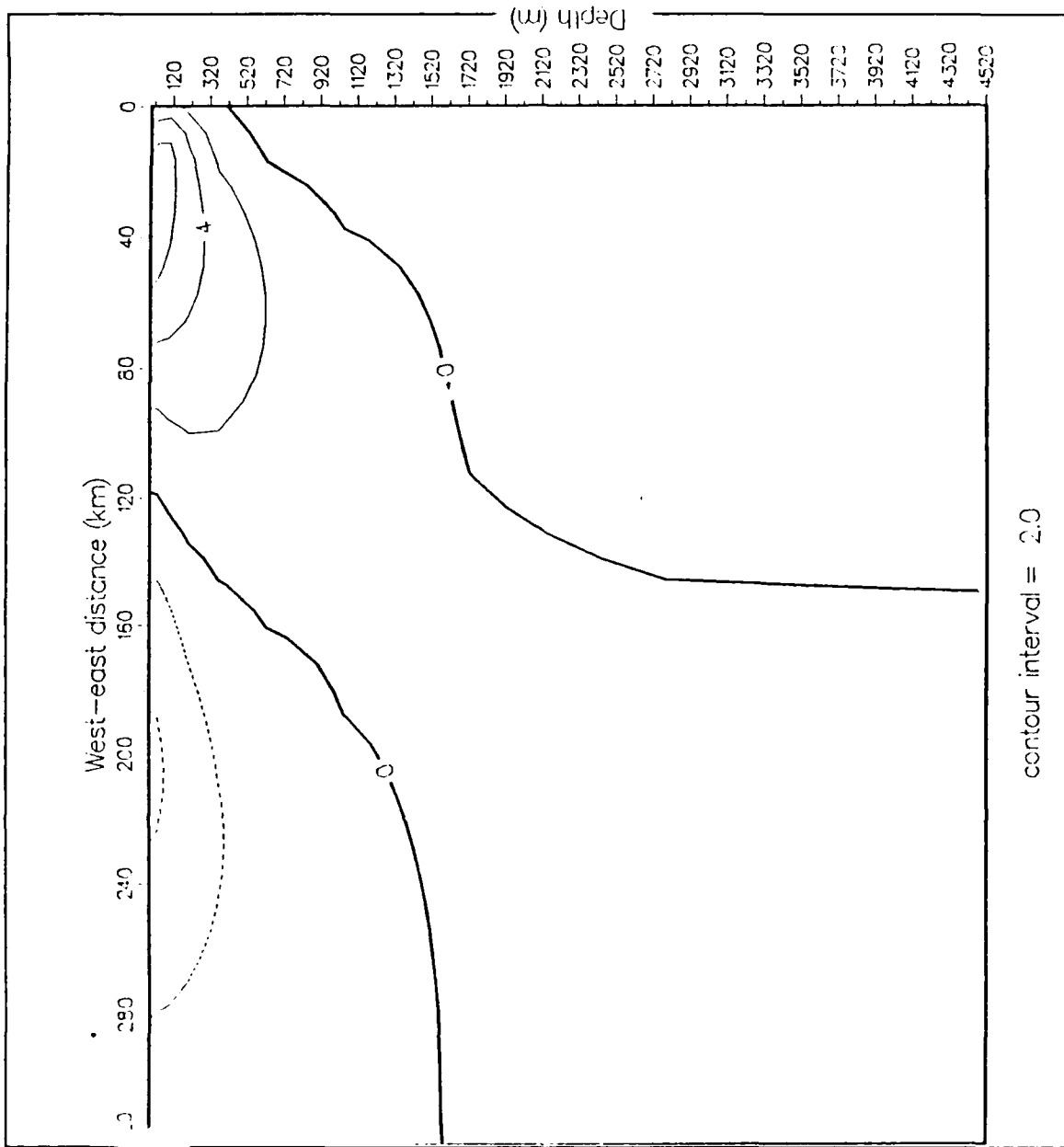


Figure 3.10 Vertical cross-shore section of meridional (v) velocity (cm s^{-1}) for Experiment 2 at day 120. Contour interval is 2.0 cm s^{-1} . Dashed contours denote equatorward velocities. The vertical cross section was alongshore-averaged.

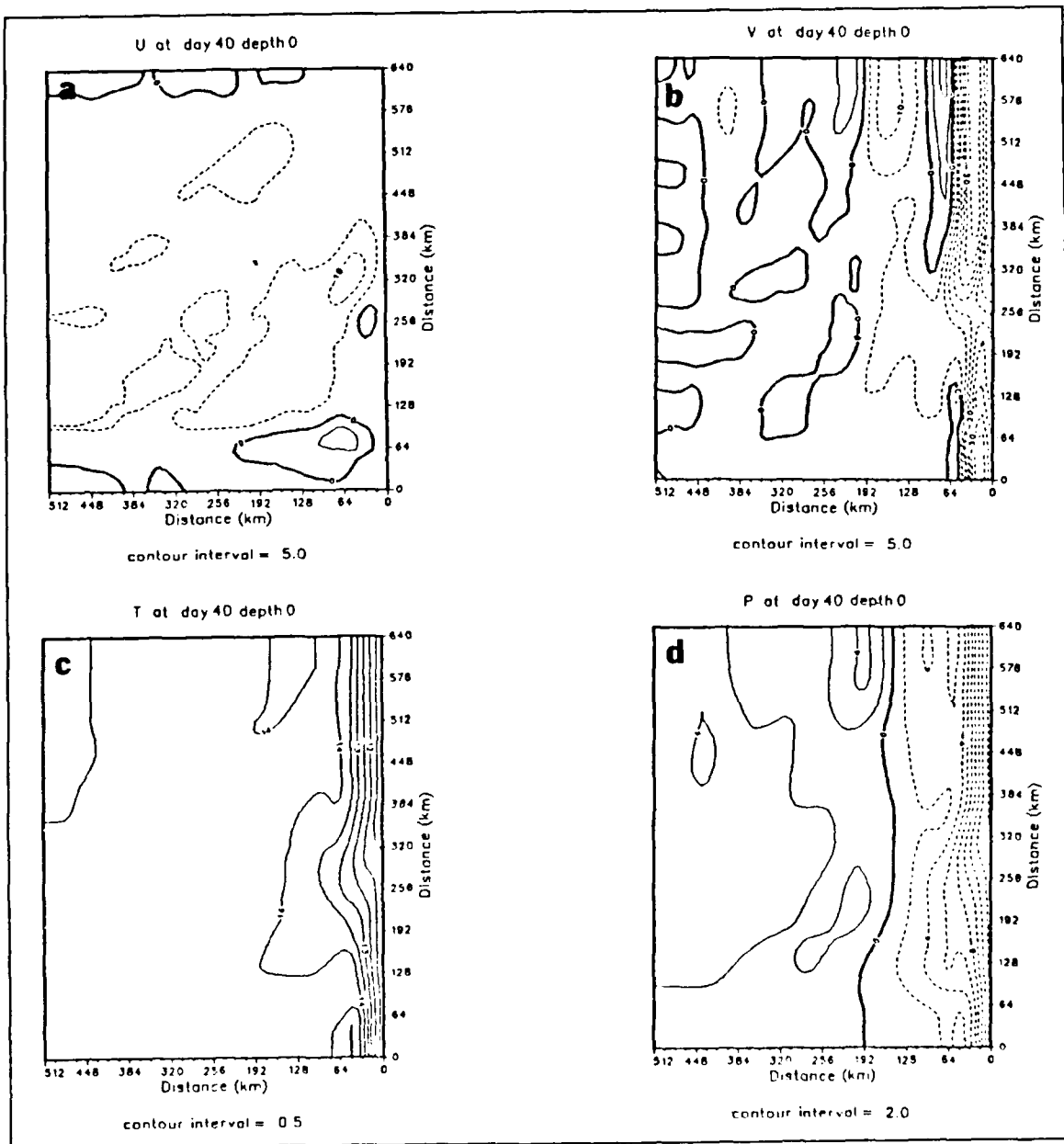


Figure 3.11 Surface isopleths of (a) zonal (u) velocity (cm s^{-1}), (b) meridional (v) velocity (cm s^{-1}), (c) temperature ($^{\circ}\text{C}$), and (d) dynamic height (cm) relative to 2400 m for Experiment 3 at day 40. Contour interval is 5.0 cm s^{-1} for (a) and (b), 0.5 $^{\circ}\text{C}$ for (c) and 2.0 cm for (d). Dashed contours denote offshore velocities in (a), equatorward velocities in (b) and negative values relative to 2400 m in (d).

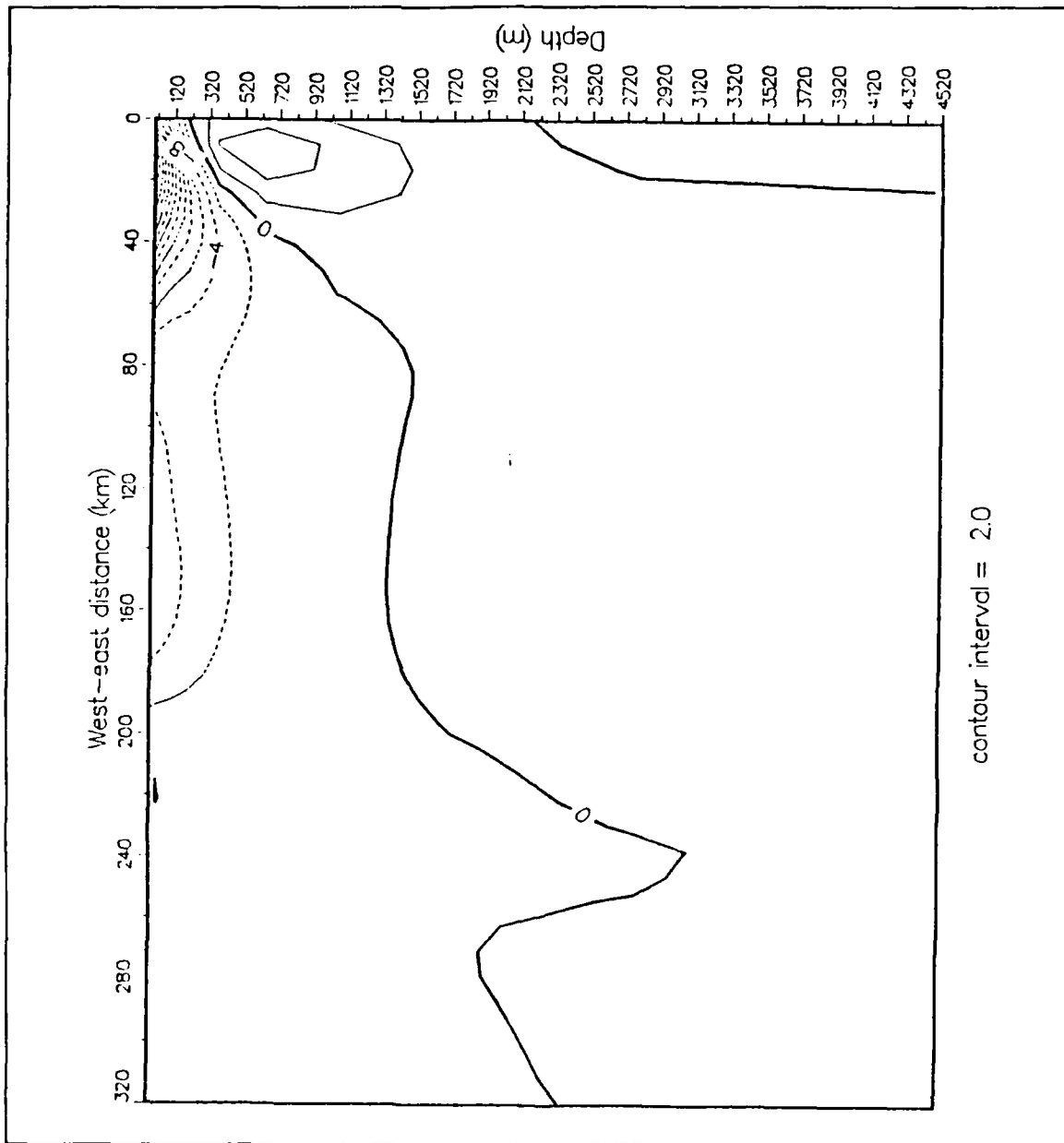


Figure 3.12 Vertical cross-shore section of meridional (v) velocity (cm s^{-1}) for Experiment 3 at day 40. Contour interval is 2.0 cm s^{-1} . Dashed contours denote equatorward velocities. The vertical cross section was alongshore-averaged.

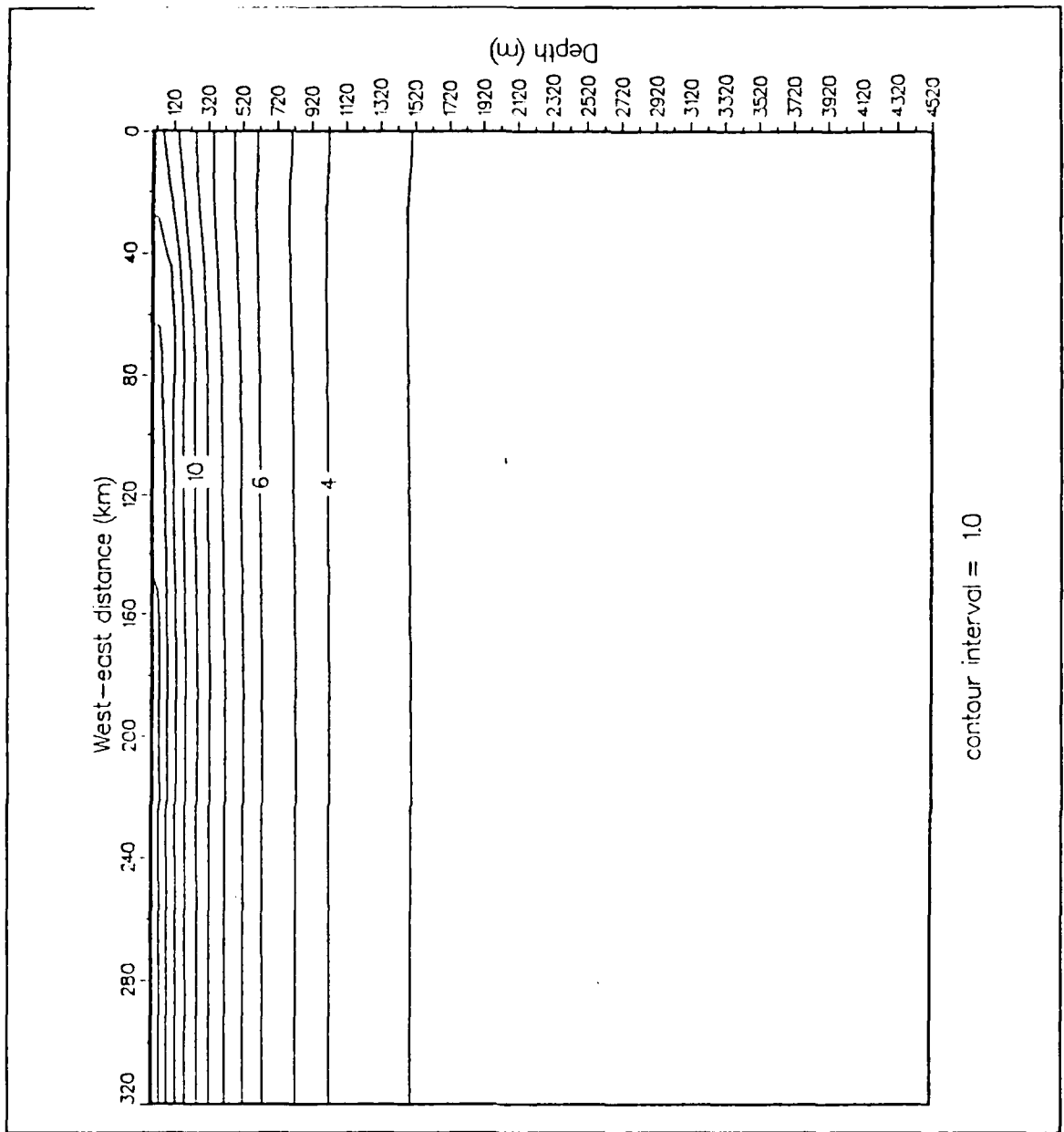


Figure 3.13 Vertical cross-shore section of temperature ($^{\circ}\text{C}$) for Experiment 3 at day 40. Contour interval is 1.0°C . The vertical cross-section was taken at $y = 290$ km.

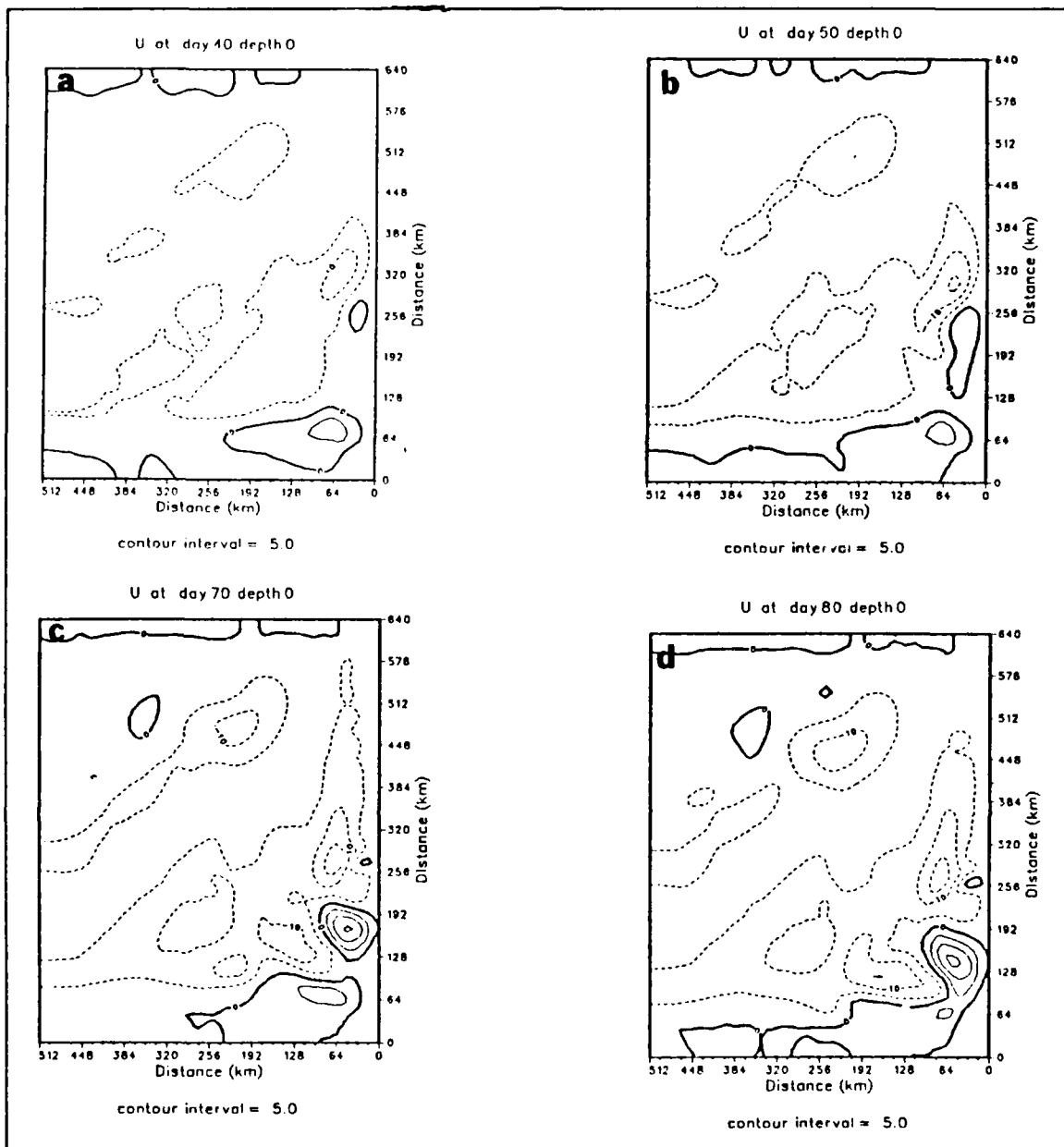


Figure 3.14 Surface isopleths of zonal (u) velocity (cm s^{-1}) for Experiment 3 at (a) day 40, (b) day 50, (c) day 70 and (d) day 80. Contour interval is 5.0 cm s^{-1} . Dashed contours denote offshore velocities.

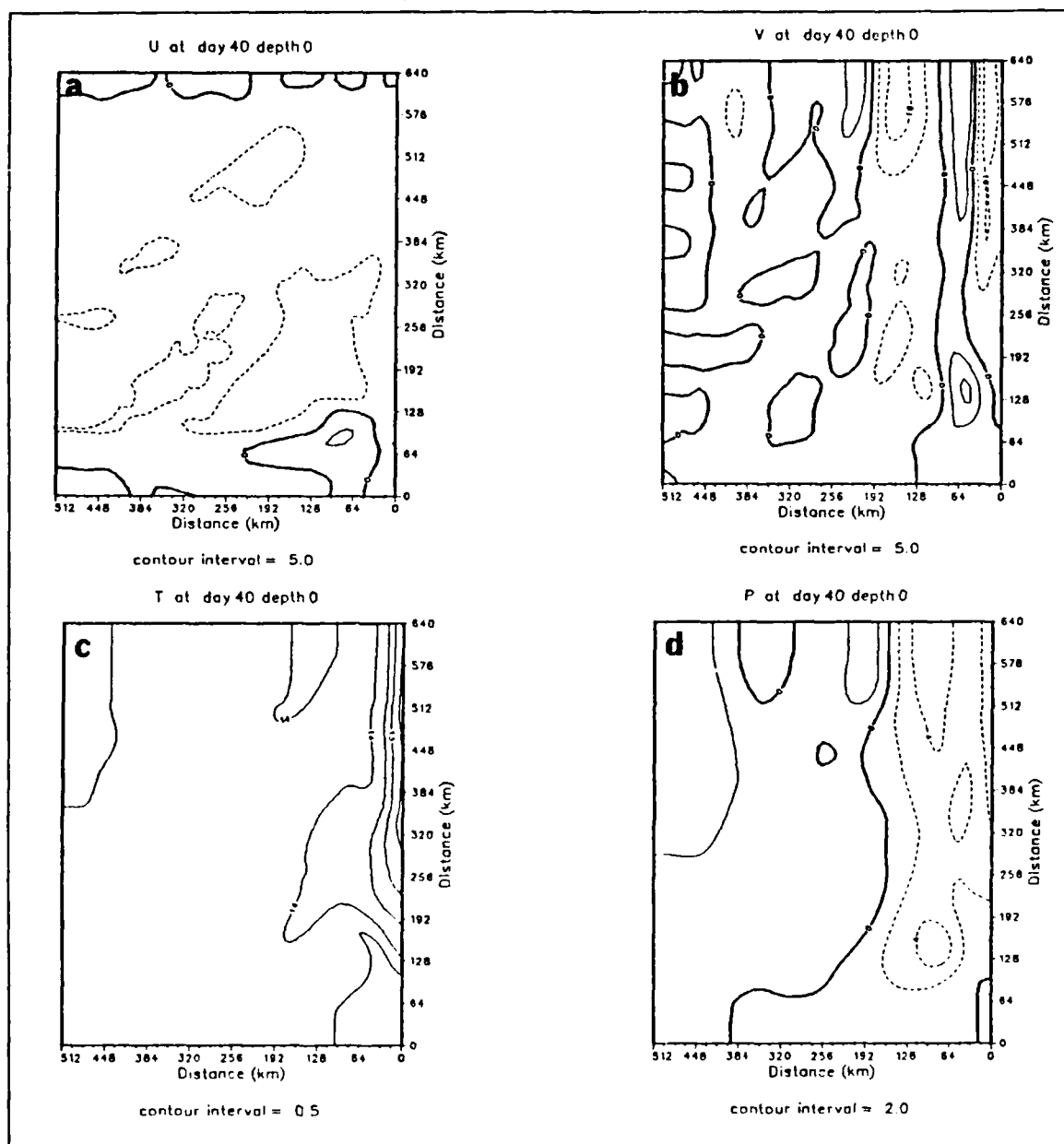


Figure 3.15 Surface isopleths of (a) zonal (u) velocity (cm s^{-1}), (b) meridional (v) velocity (cm s^{-1}), (c) temperature ($^{\circ}\text{C}$), and (d) dynamic height (cm) relative to 2400 m for Experiment 4 at day 40. Contour interval is 5.0 cm s^{-1} for (a) and (b), $0.5 \text{ }^{\circ}\text{C}$ for (c) and 2.0 cm for (d). Dashed contours denote offshore velocities in (a), equatorward velocities in (b) and negative values relative to 2400 m in (d).

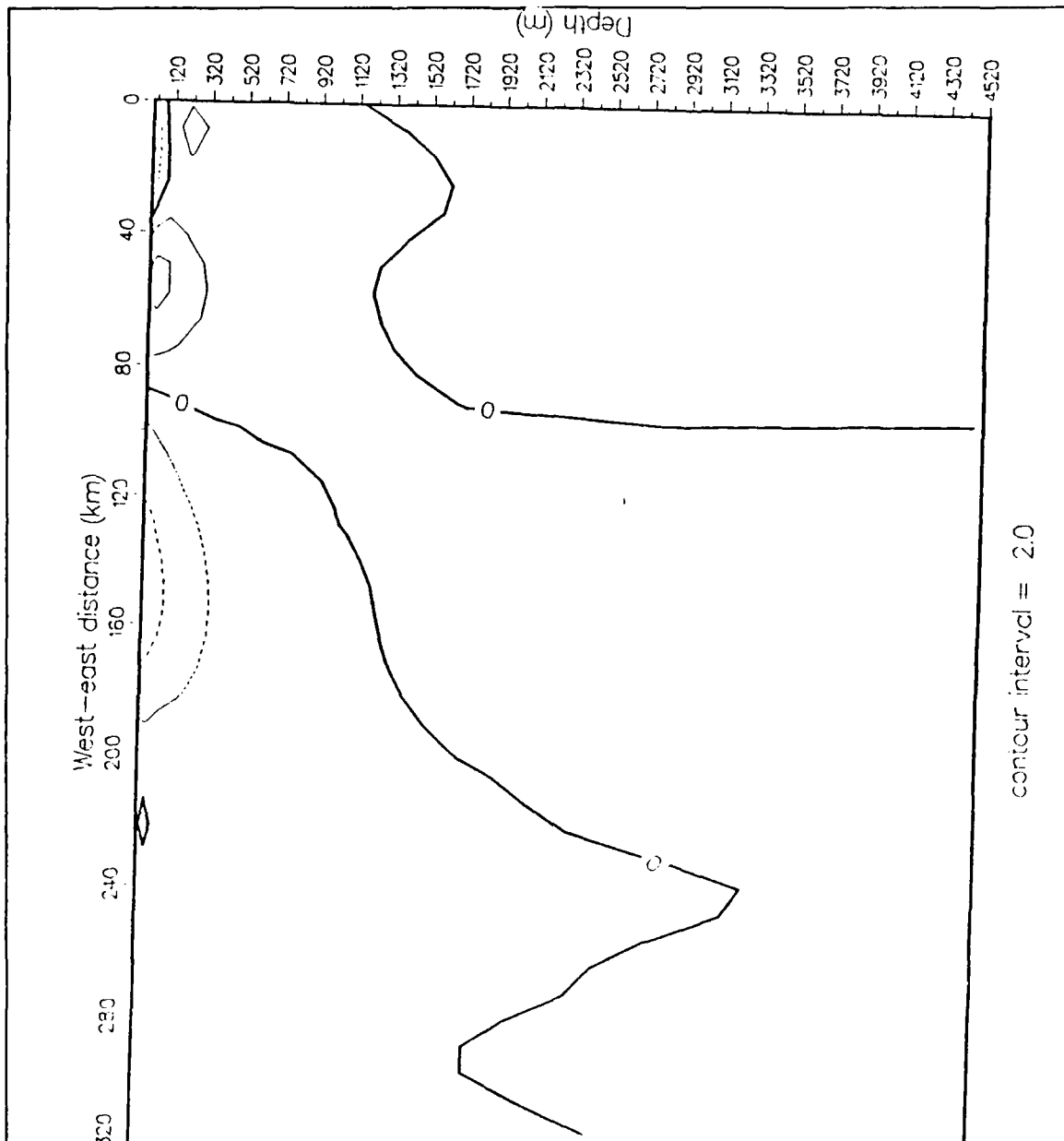


Figure 3.16 Vertical cross-shore section of meridional (v) velocity (cm s^{-1}) for Experiment 4 at day 40. Contour interval is 2.0 cm s^{-1} . Dashed contours denote equatorward velocities. The vertical cross section was alongshore-averaged.

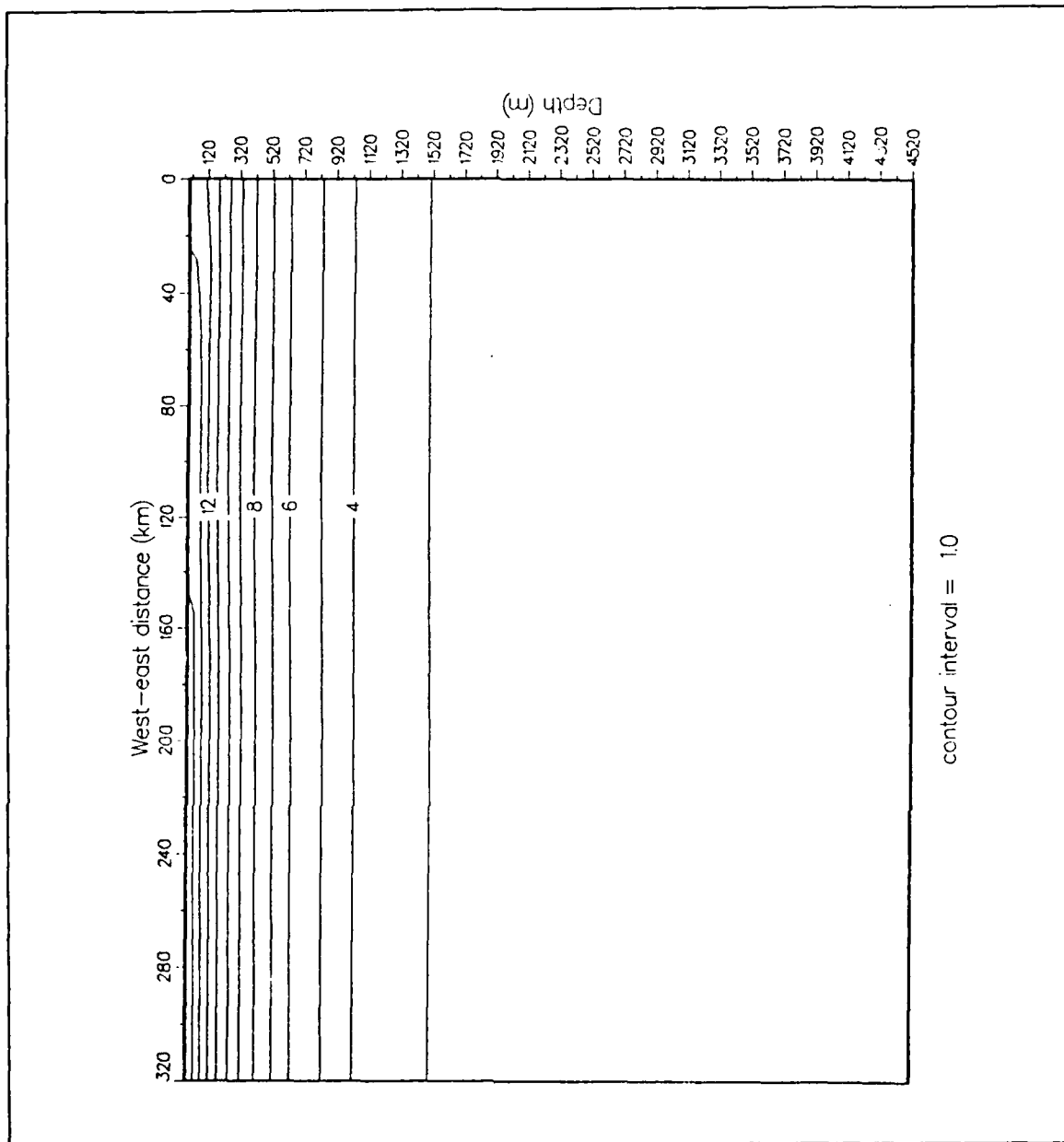


Figure 3.17 Vertical cross-shore section of temperature ($^{\circ}\text{C}$) for Experiment 4 at day 40. Contour interval is 1.0°C . The vertical cross-section was taken at $y = 290$ km.

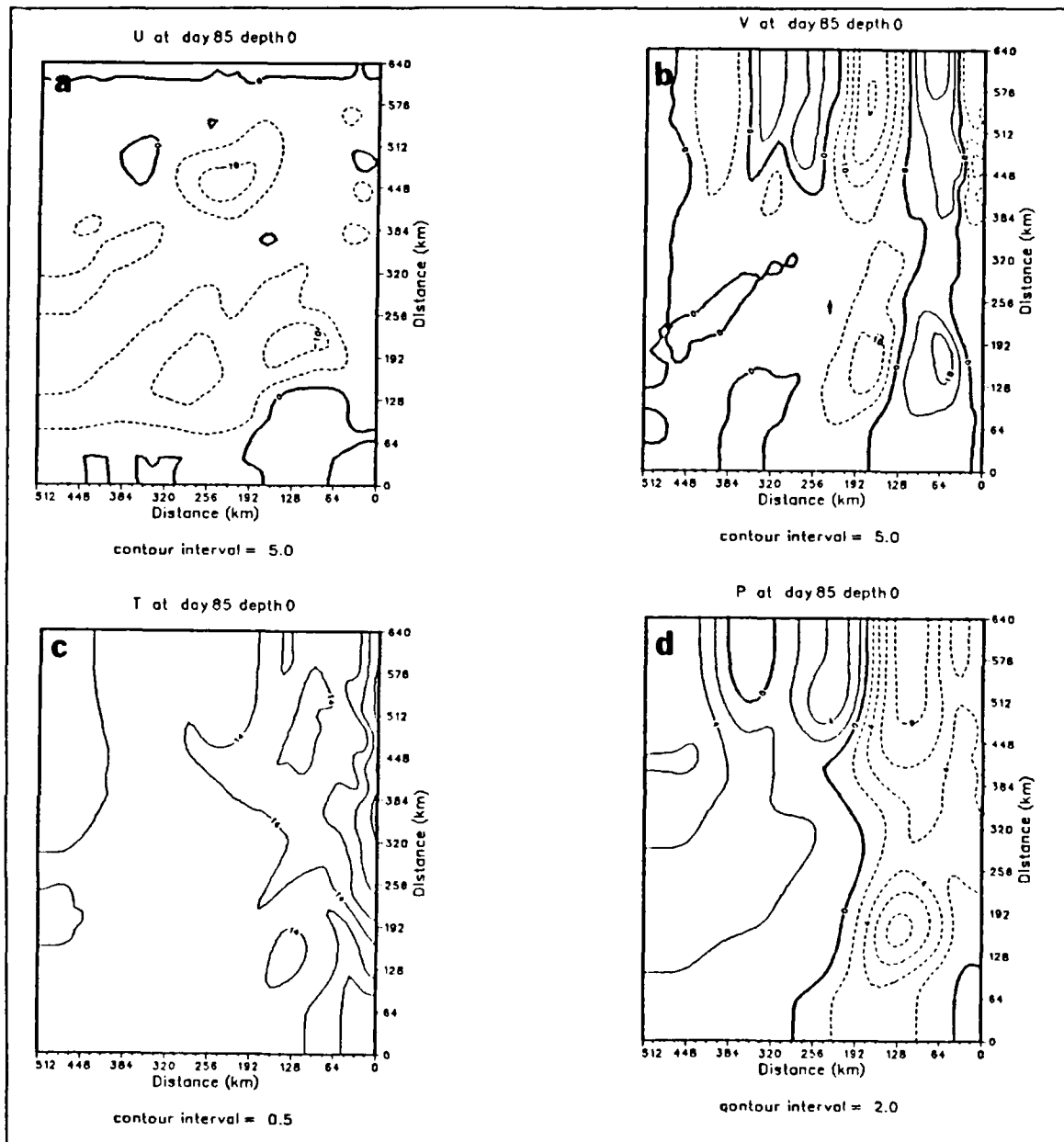


Figure 3.18 Surface isopleths of (a) zonal (u) velocity (cm s^{-1}), (b) meridional (v) velocity (cm s^{-1}), (c) temperature ($^{\circ}\text{C}$), and (d) dynamic height (cm) relative to 2400 m for Experiment 4 at day 85. Contour interval is 5.0 cm s^{-1} for (a) and (b), $0.5 \text{ }^{\circ}\text{C}$ for (c) and 2.0 cm for (d). Dashed contours denote offshore velocities in (a), equatorward velocities in (b) and negative values relative to 2400 m in (d).

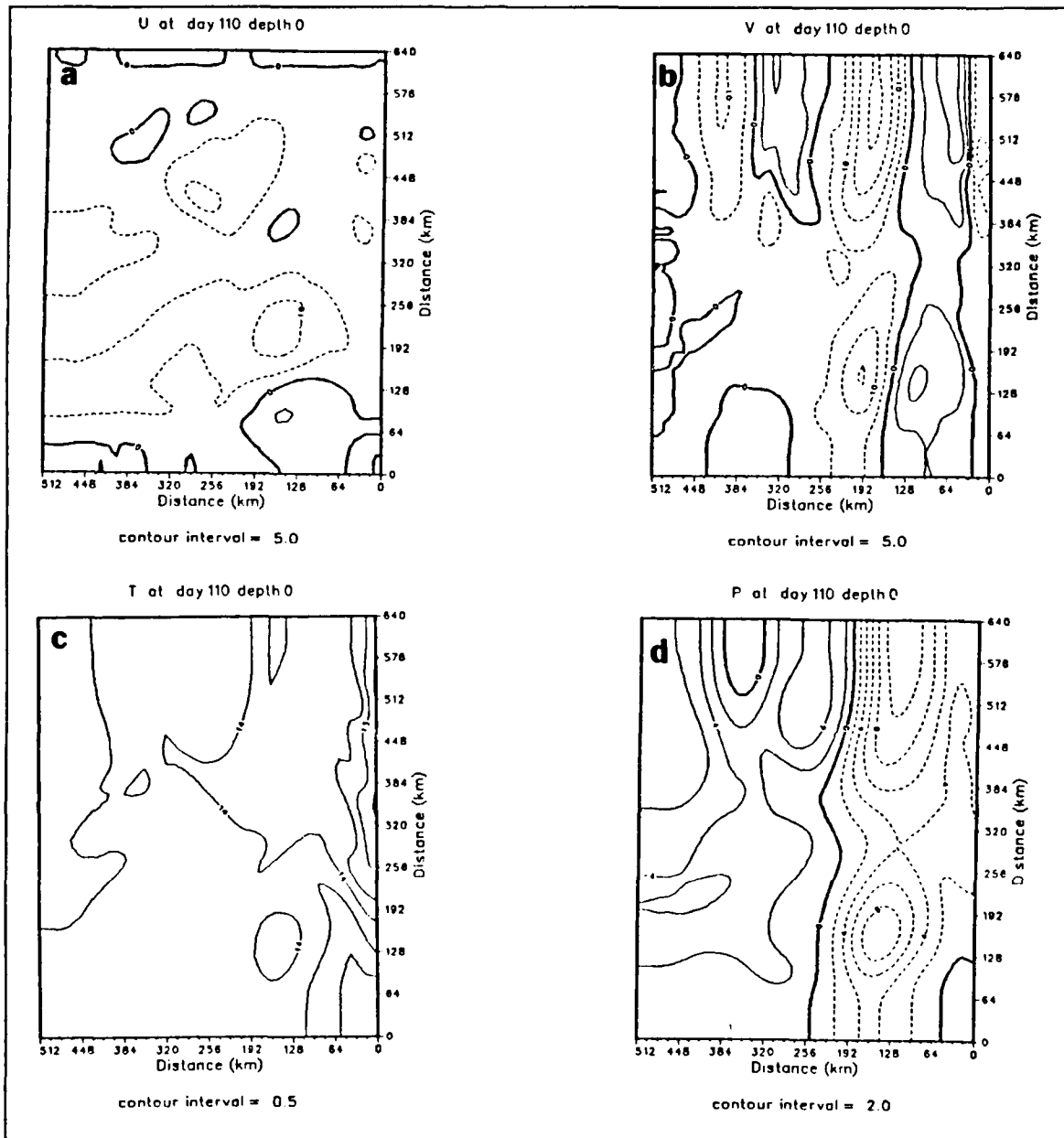


Figure 3.19 Surface isopleths of (a) zonal (u) velocity (cm s^{-1}), (b) meridional (v) velocity (cm s^{-1}), (c) temperature ($^{\circ}\text{C}$), and (d) dynamic height (cm) relative to 2400 m for Experiment 4 at day 110. Contour interval is 5.0 cm s^{-1} for (a) and (b), $0.5 \text{ }^{\circ}\text{C}$ for (c) and 2.0 cm for (d). Dashed contours denote offshore velocities in (a), equatorward velocities in (b) and negative values relative to 2400 m in (d).

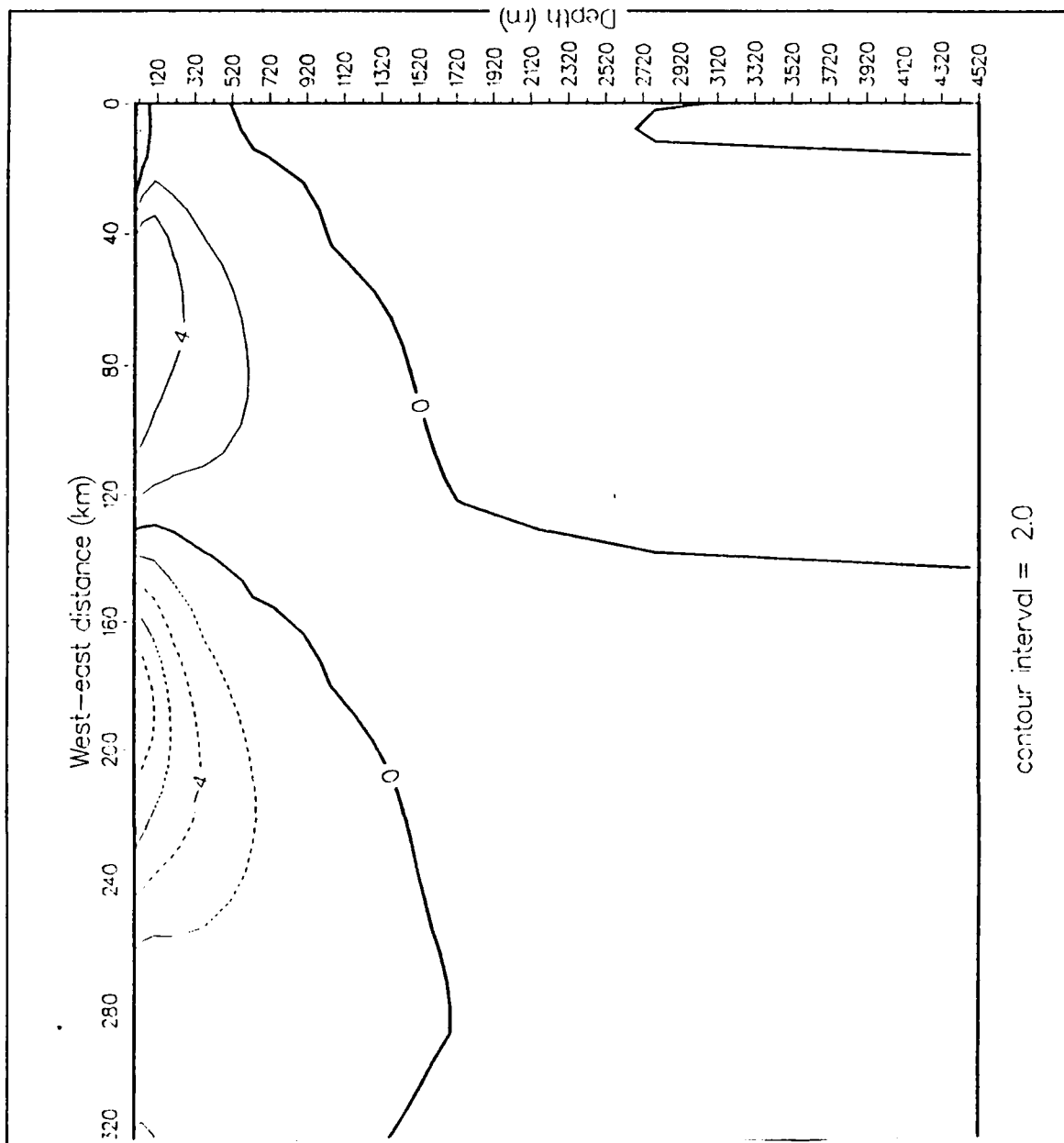


Figure 3.20 Vertical cross-shore section of meridional (v) velocity (cm s^{-1}) for Experiment 4 at day 110. Contour interval is 2.0 cm s^{-1} . Dashed contours denote equatorward velocities. The vertical cross section was alongshore-averaged.

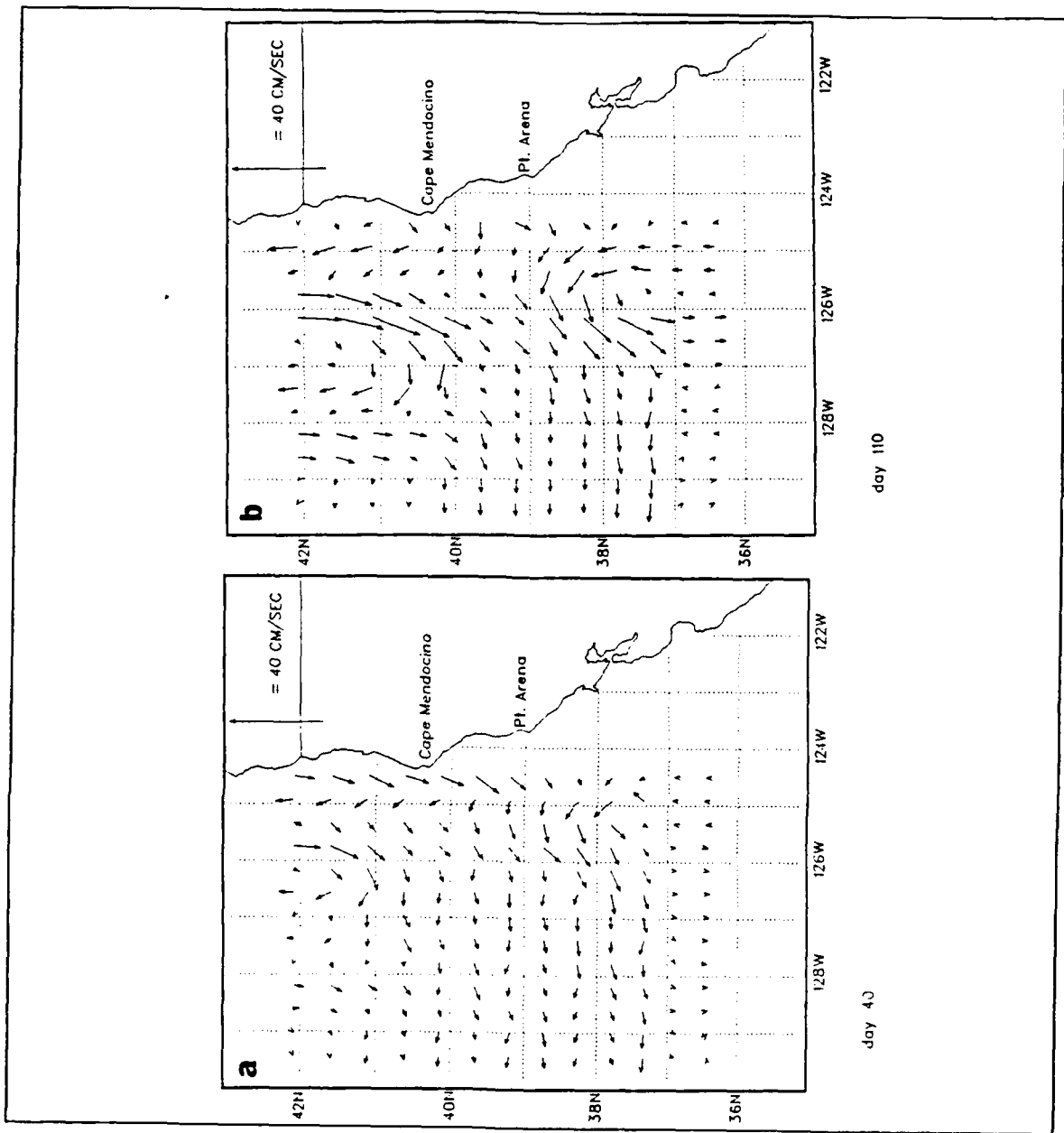


Figure 3.21 Surface current vectors for Experiment 4 at (a) day 40, (b) day 110.

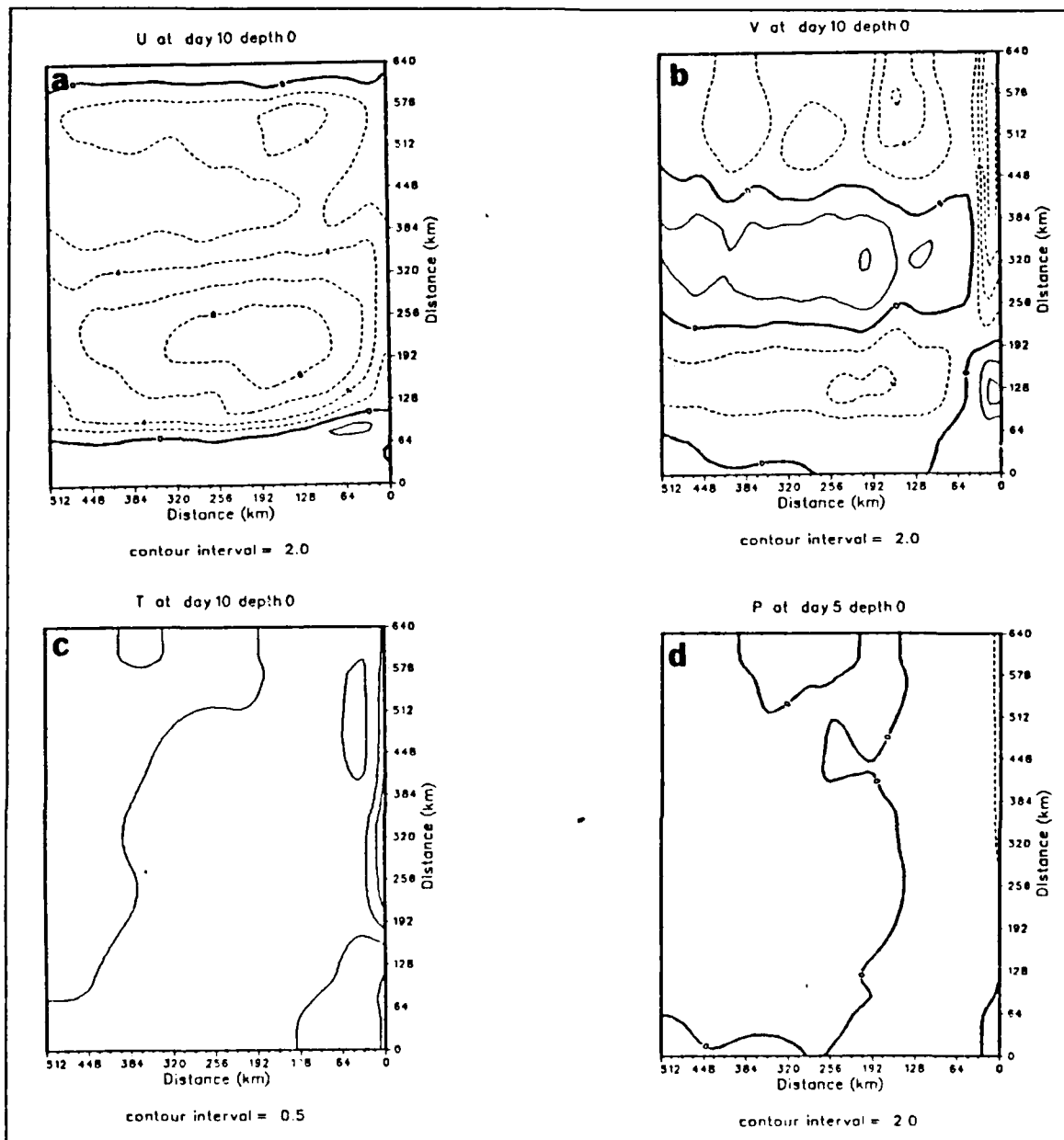


Figure 3.22 Surface isopleths of (a) zonal (u) velocity (cm s^{-1}), (b) meridional (v) velocity (cm s^{-1}), (c) temperature ($^{\circ}\text{C}$), and (d) dynamic height (cm) relative to 2400 m for Experiment 5 at day 10. Contour interval is 2.0 cm s^{-1} for (a) and (b), $0.5 \text{ }^{\circ}\text{C}$ for (c) and 2.0 cm for (d). Dashed contours denote offshore velocities in (a), equatorward velocities in (b) and negative values relative to 2400 m in (d).

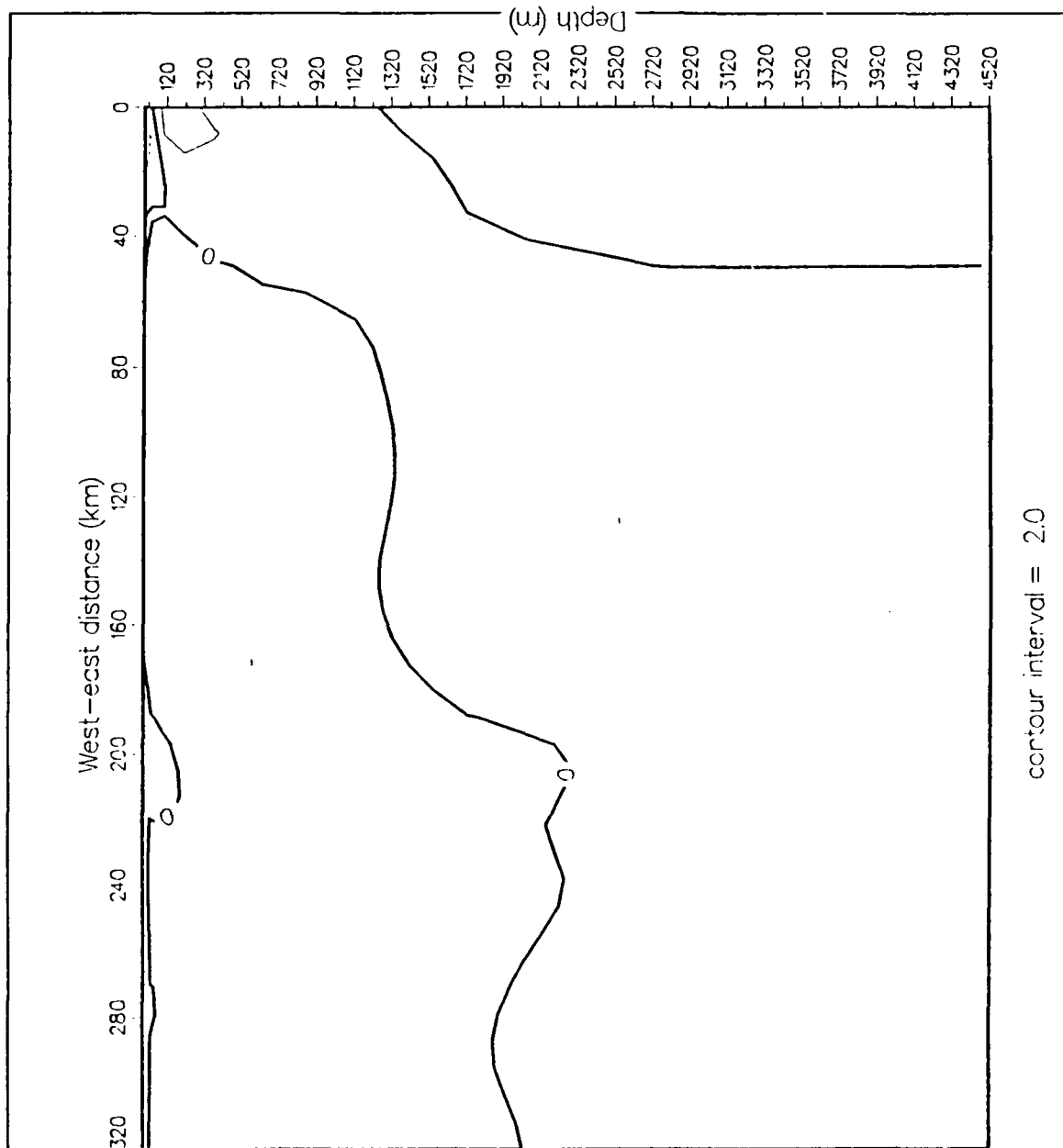


Figure 3.23 Vertical cross-shore section of meridional (v) velocity (cm s^{-1}) for Experiment 5 at day 10. Contour interval is 2.0 cm s^{-1} . Dashed contours denote equatorward velocities. The vertical cross section was alongshore-averaged.

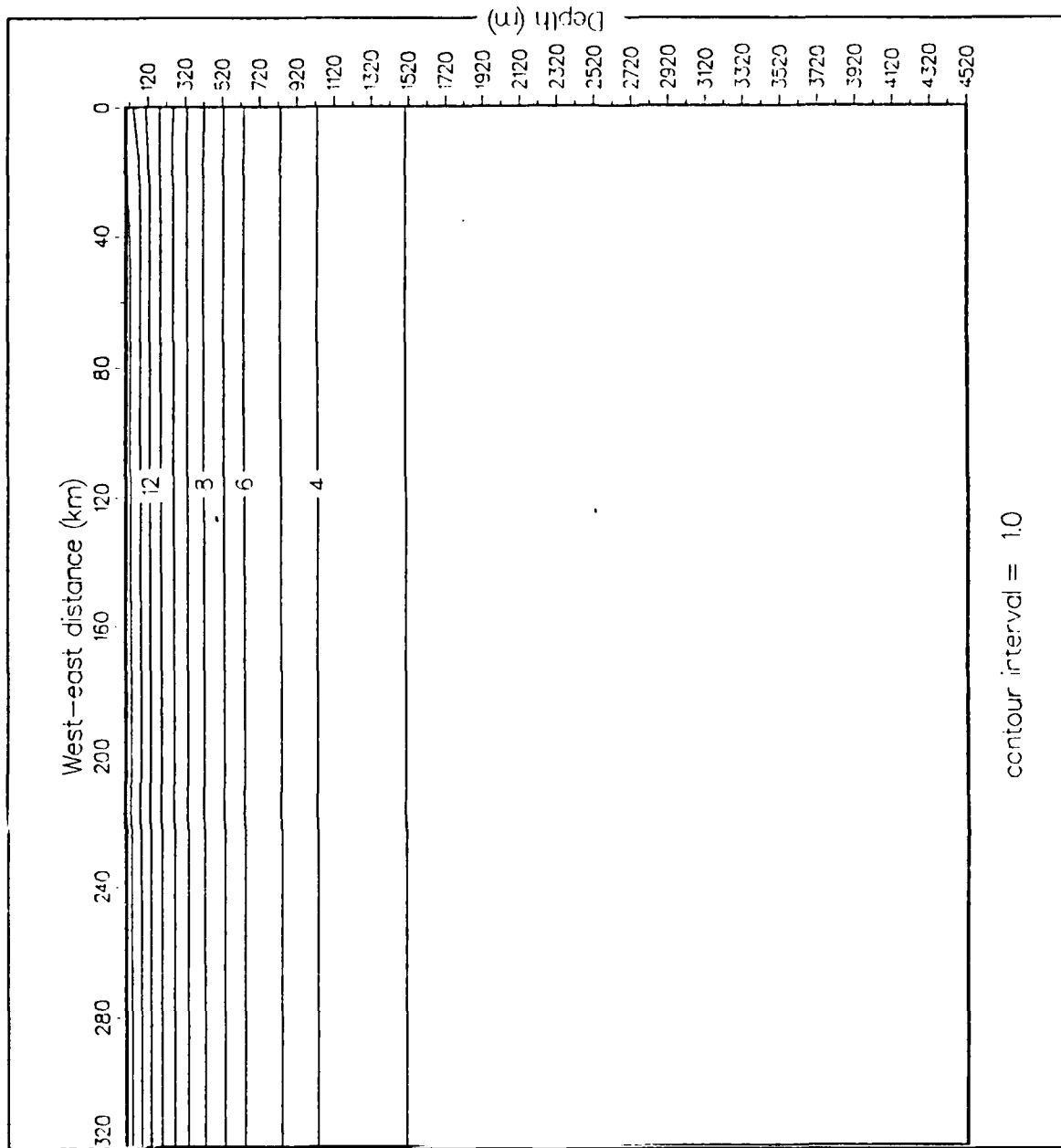


Figure 3.24 Vertical cross-shore section of temperature ($^{\circ}\text{C}$) for Experiment 5 at day 10. Contour interval is 1.0°C . The vertical cross-section was taken at $y = 290$ km.

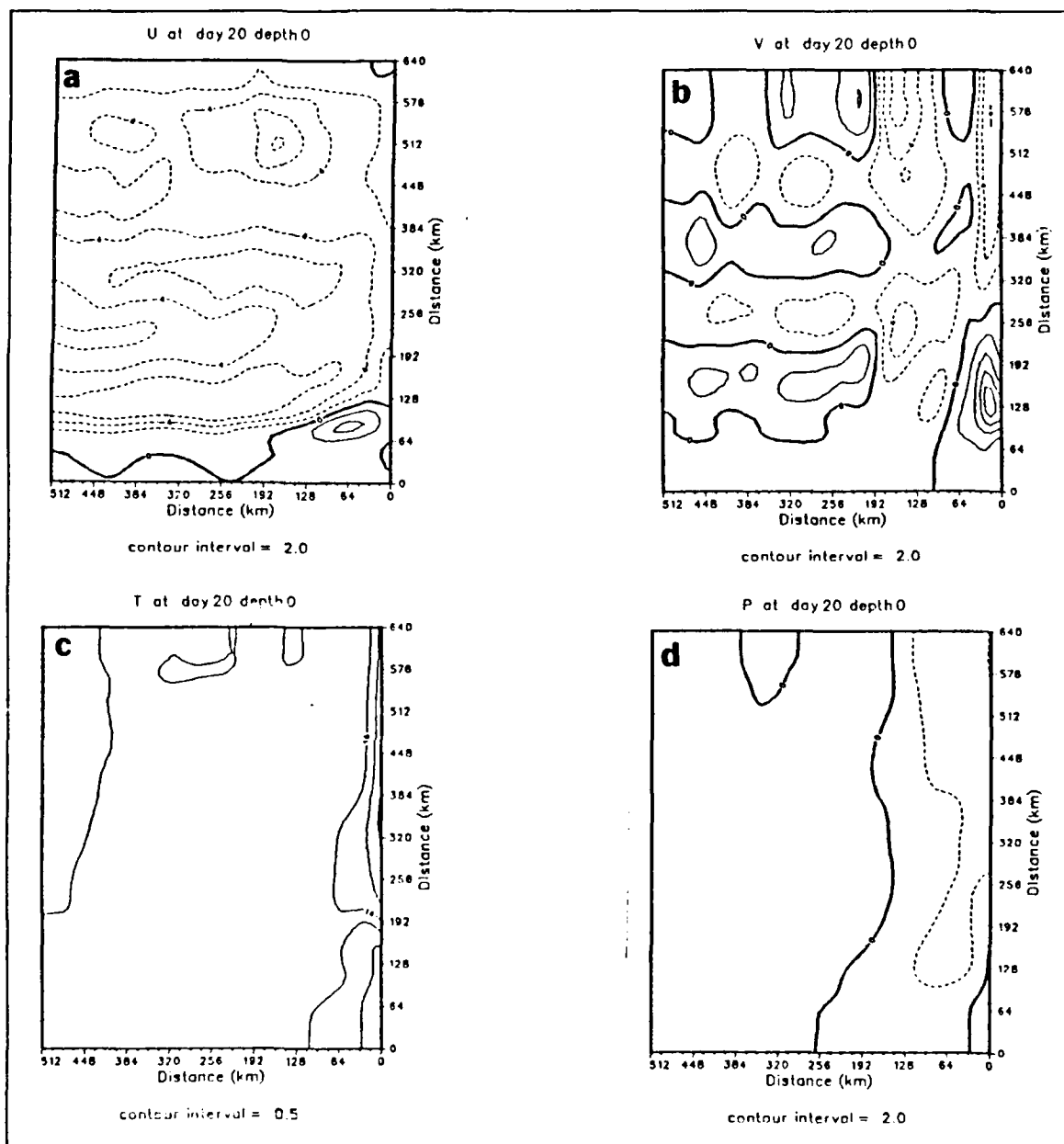


Figure 3.25 Surface isopleths of (a) zonal (u) velocity (cm s^{-1}), (b) meridional (v) velocity (cm s^{-1}), (c) temperature ($^{\circ}\text{C}$), and (d) dynamic height (cm) relative to 2400 m for Experiment 5 at day 20. Contour interval is 2.0 cm s^{-1} for (a) and (b), 0.5 $^{\circ}\text{C}$ for (c) and 2.0 cm for (d). Dashed contours denote offshore velocities in (a), equatorward velocities in (b) and negative values relative to 2400 m in (d).

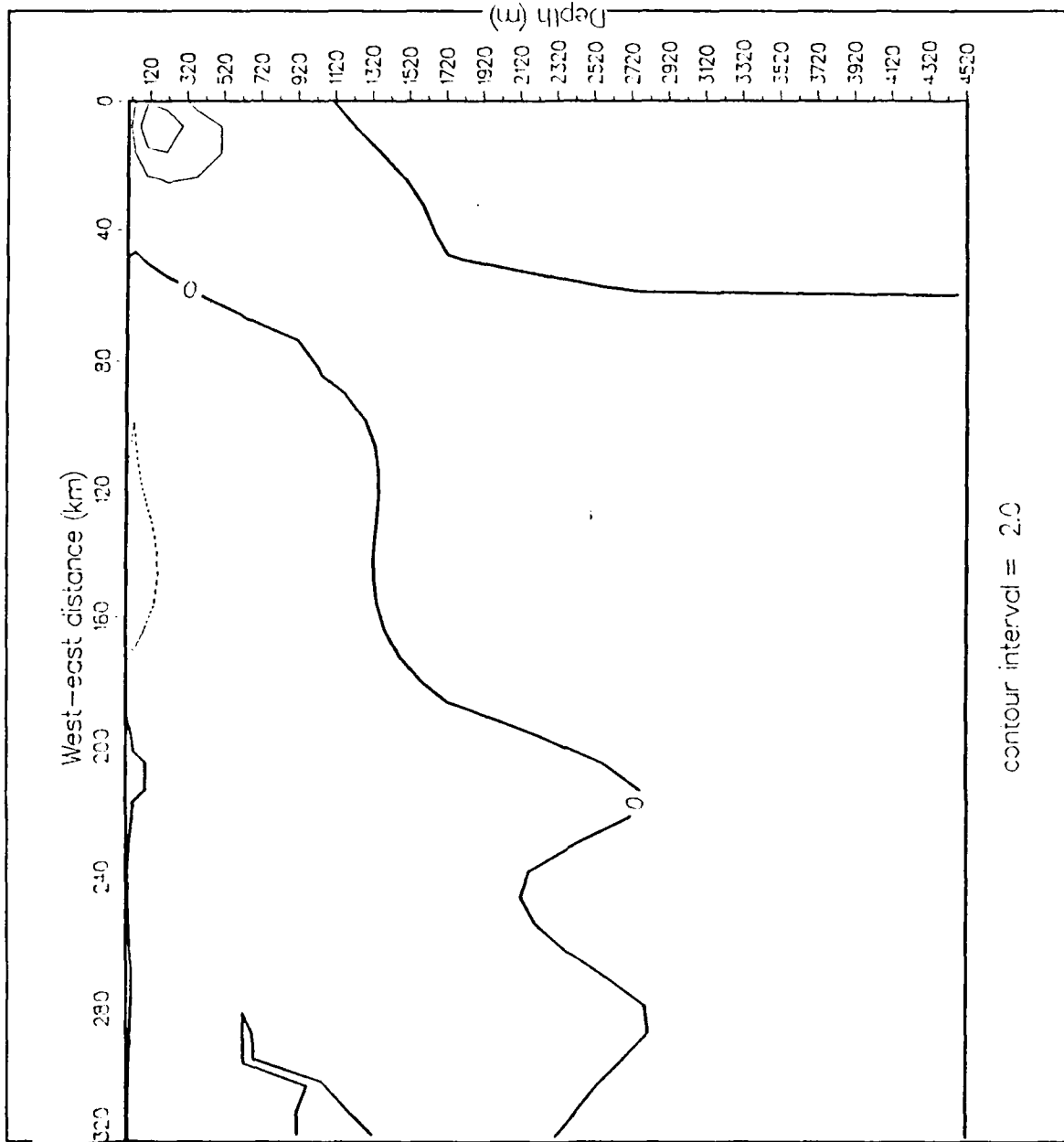


Figure 3.26 Vertical cross-shore section of meridional (v) velocity (cm s^{-1}) for Experiment 5 at day 20. Contour interval is 2.0 cm s^{-1} . Dashed contours denote equatorward velocities. The vertical cross section was alongshore-averaged.

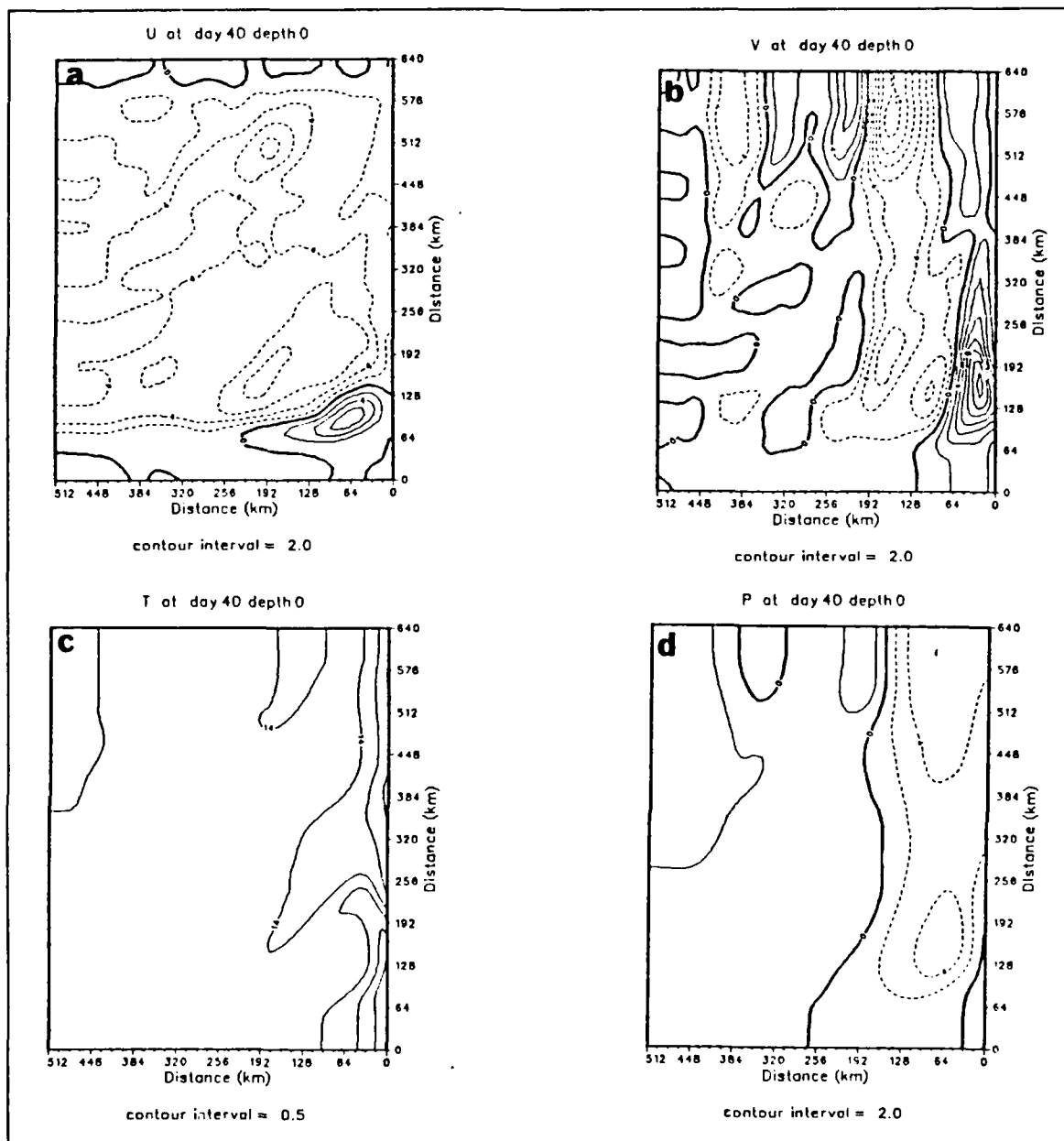


Figure 3.27 Surface isopleths of (a) zonal (u) velocity (cm s^{-1}), (b) meridional (v) velocity (cm s^{-1}), (c) temperature ($^{\circ}\text{C}$), and (d) dynamic height (cm) relative to 2400 m for Experiment 5 at day 40. Contour interval is 2.0 cm s^{-1} for (a) and (b), 0.5 $^{\circ}\text{C}$ for (c) and 2.0 cm for (d). Dashed contours denote offshore velocities in (a), equatorward velocities in (b) and negative values relative to 2400 m in (d).

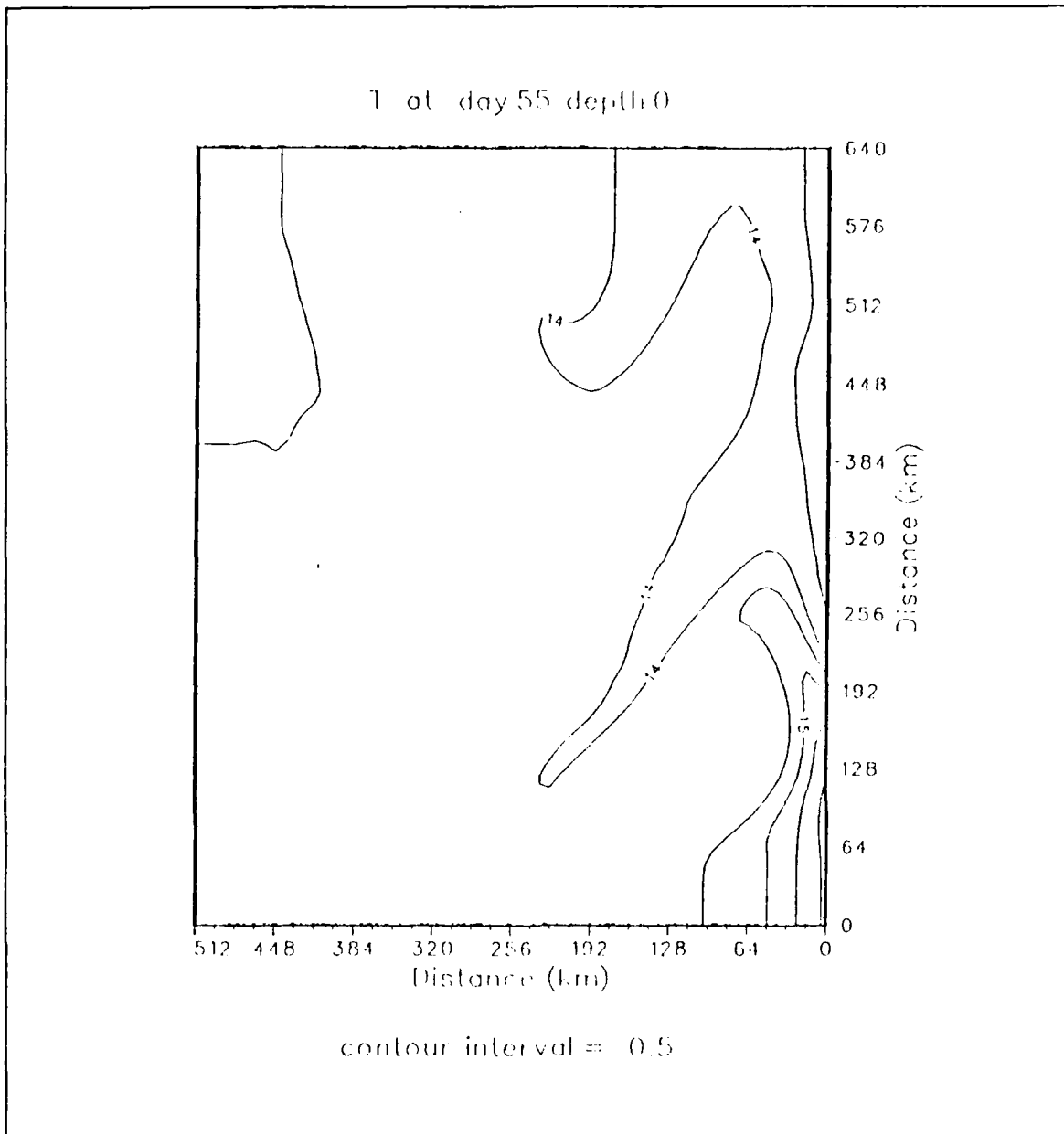


Figure 3.28 Surface isopleths temperature ($^{\circ}\text{C}$) Experiment 5 at day 55. Contour interval is 0.5°C .

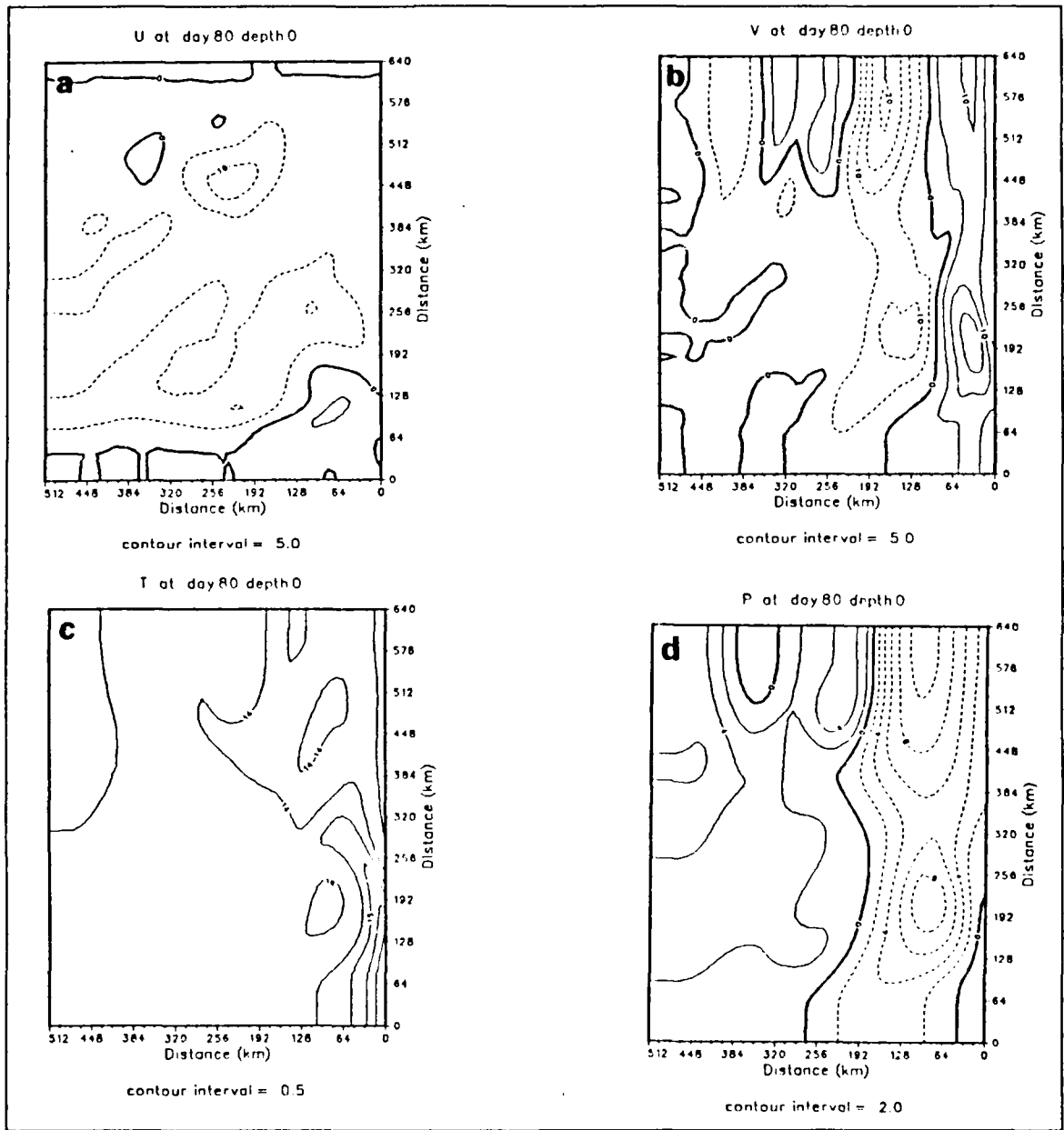


Figure 3.29 Surface isopleths of (a) zonal (u) velocity (cm s^{-1}), (b) meridional (v) velocity (cm s^{-1}), (c) temperature ($^{\circ}\text{C}$), and (d) dynamic height (cm) relative to 2400 m for Experiment 5 at day 80. Contour interval is 5.0 cm s^{-1} for (a) and (b), $0.5 \text{ }^{\circ}\text{C}$ for (c) and 2.0 cm for (d). Dashed contours denote offshore velocities in (a), equatorward velocities in (b) and negative values relative to 2400 m in (d).

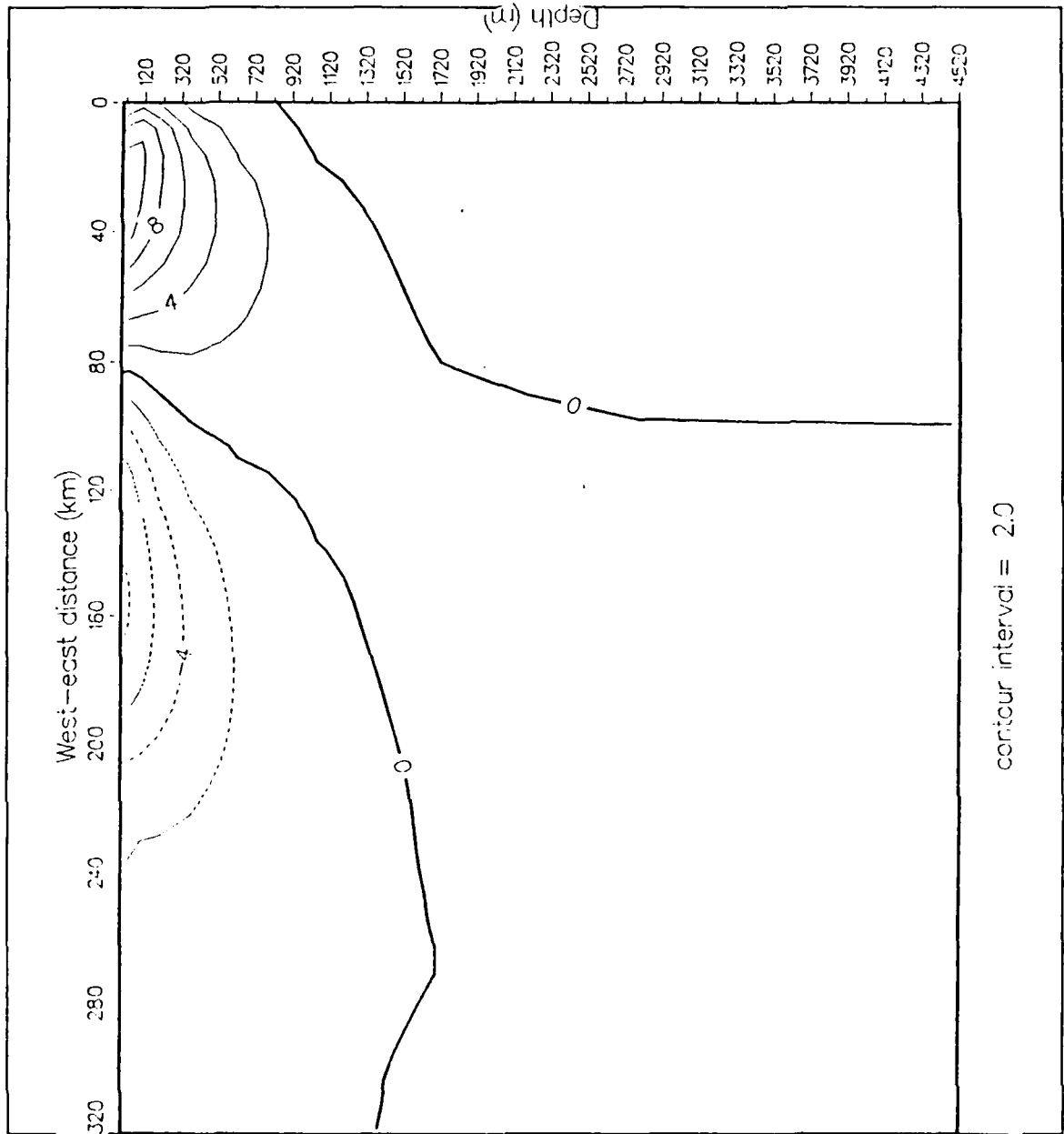


Figure 3.30 Vertical cross-shore section of meridional (v) velocity (cm s^{-1}) for Experiment 5 at day 80. Contour interval is 2.0 cm s^{-1} . Dashed contours denote equatorward velocities. The vertical cross section was alongshore-averaged.

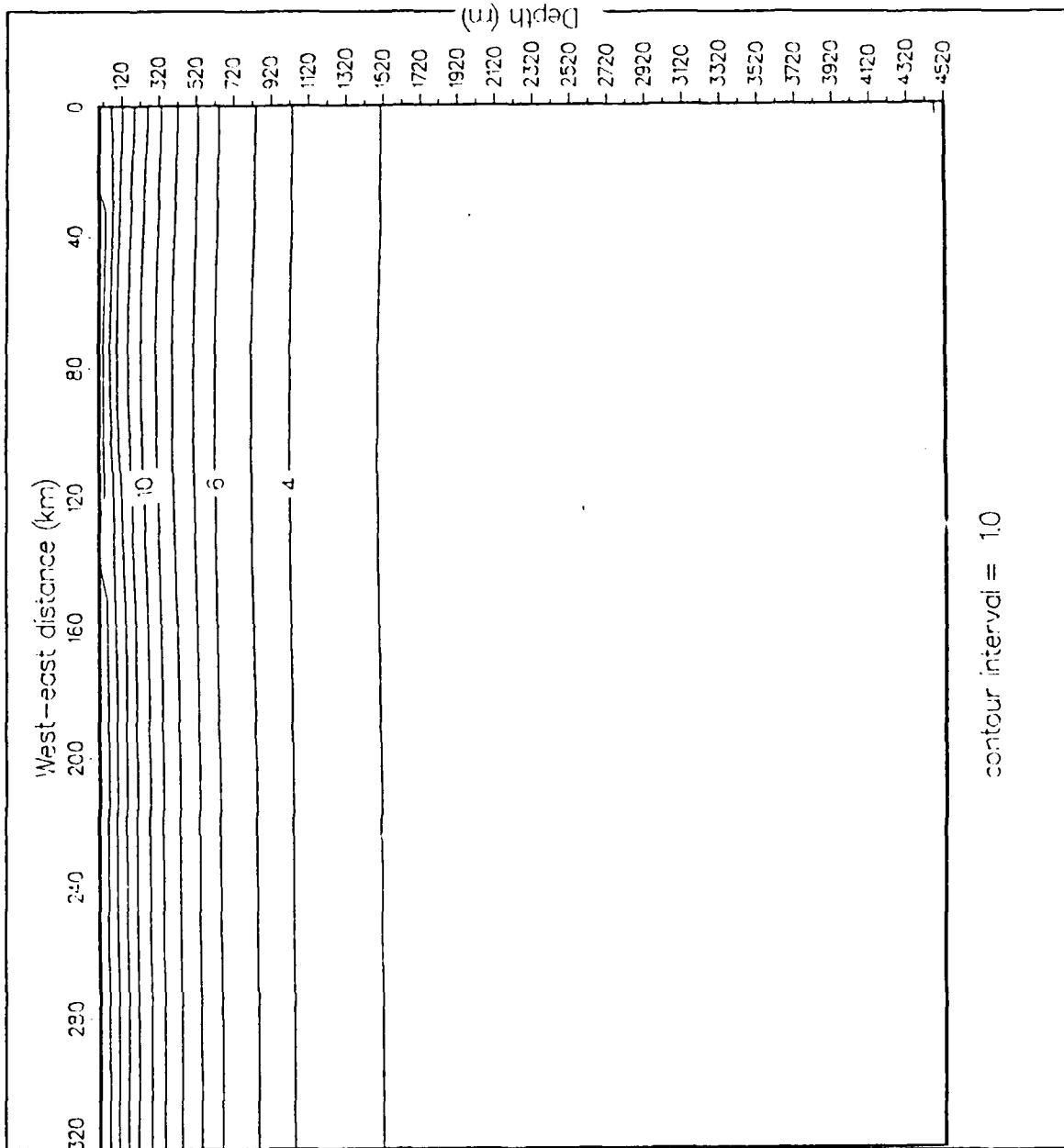


Figure 3.31 Vertical cross-shore section of temperature ($^{\circ}\text{C}$) for Experiment 5 at day 80. Contour interval is 1.0°C . The vertical cross-section was taken at $y = 290$ km.

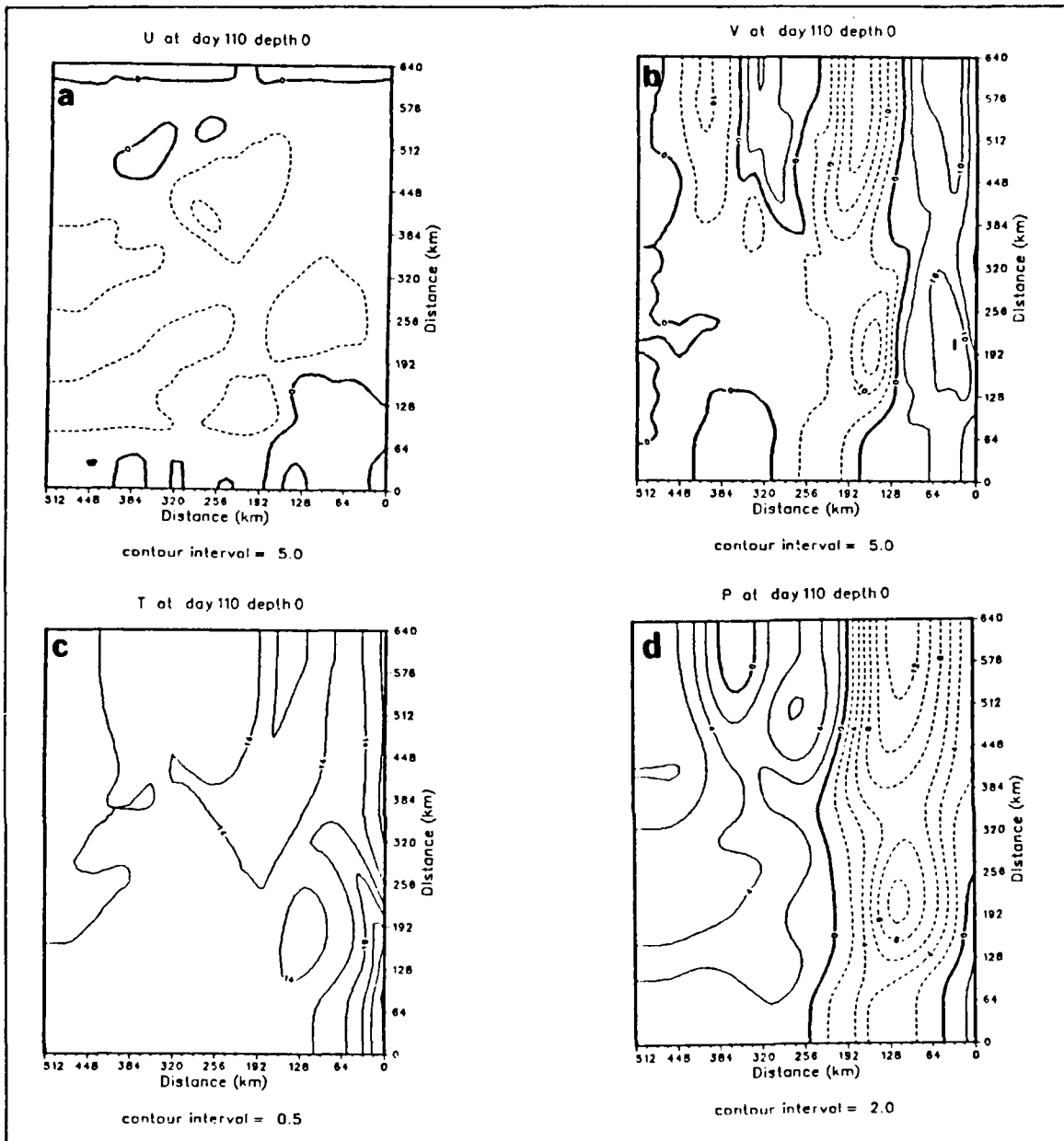


Figure 3.32 Surface isopleths of (a) zonal (u) velocity (cm s^{-1}), (b) meridional (v) velocity (cm s^{-1}), (c) temperature ($^{\circ}\text{C}$), and (d) dynamic height (cm) relative to 2400 m for Experiment 5 at day 110. Contour interval is 5.0 cm s^{-1} for (a) and (b), $0.5 \text{ }^{\circ}\text{C}$ for (c) and 2.0 cm for (d). Dashed contours denote offshore velocities in (a), equatorward velocities in (b) and negative values relative to 2400 m in (d).

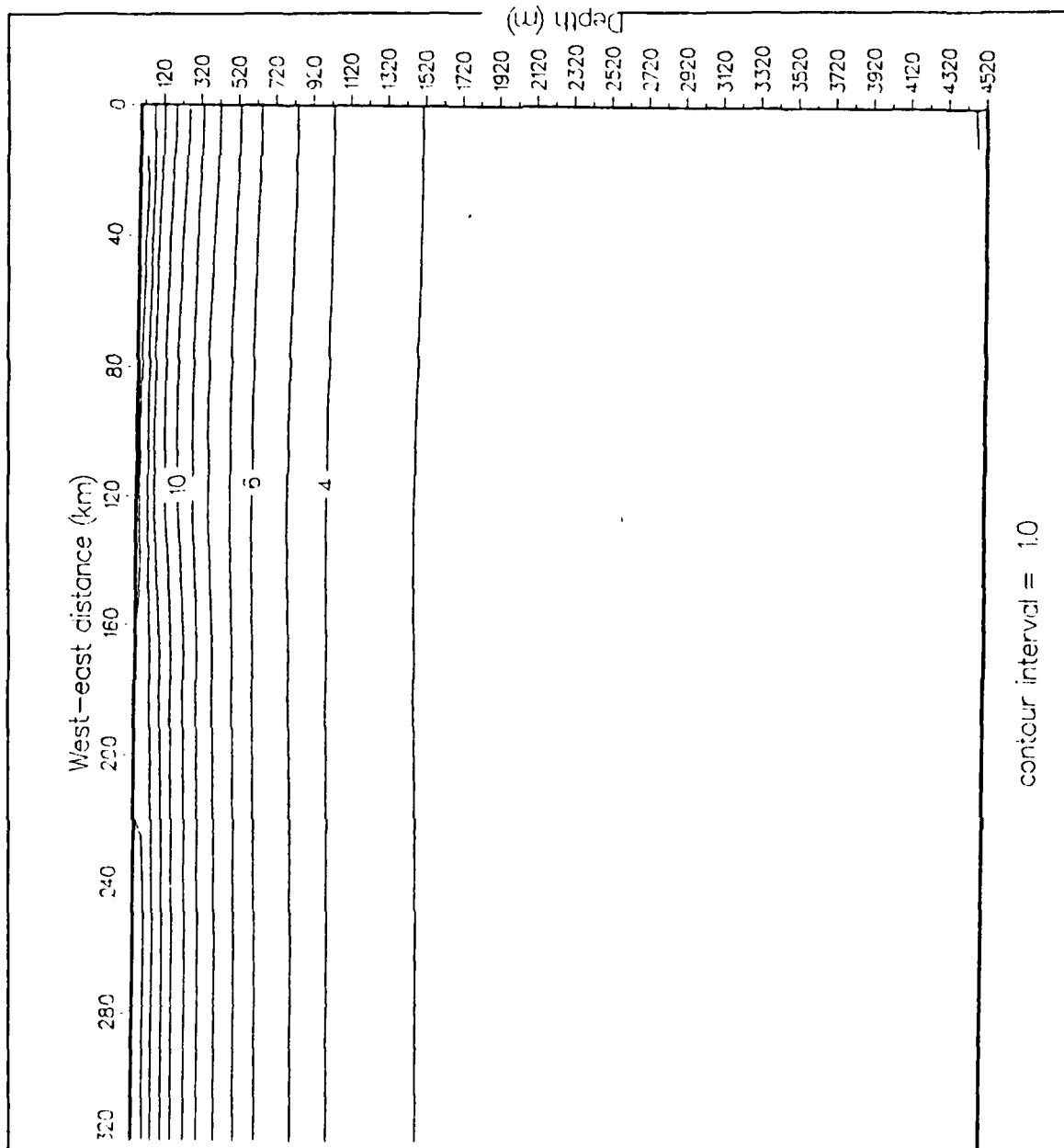


Figure 3.33 Vertical cross-shore section of temperature ($^{\circ}\text{C}$) for Experiment 5 at day 110. Contour interval is 1.0°C . The vertical cross-section was taken at $y = 290$ km.

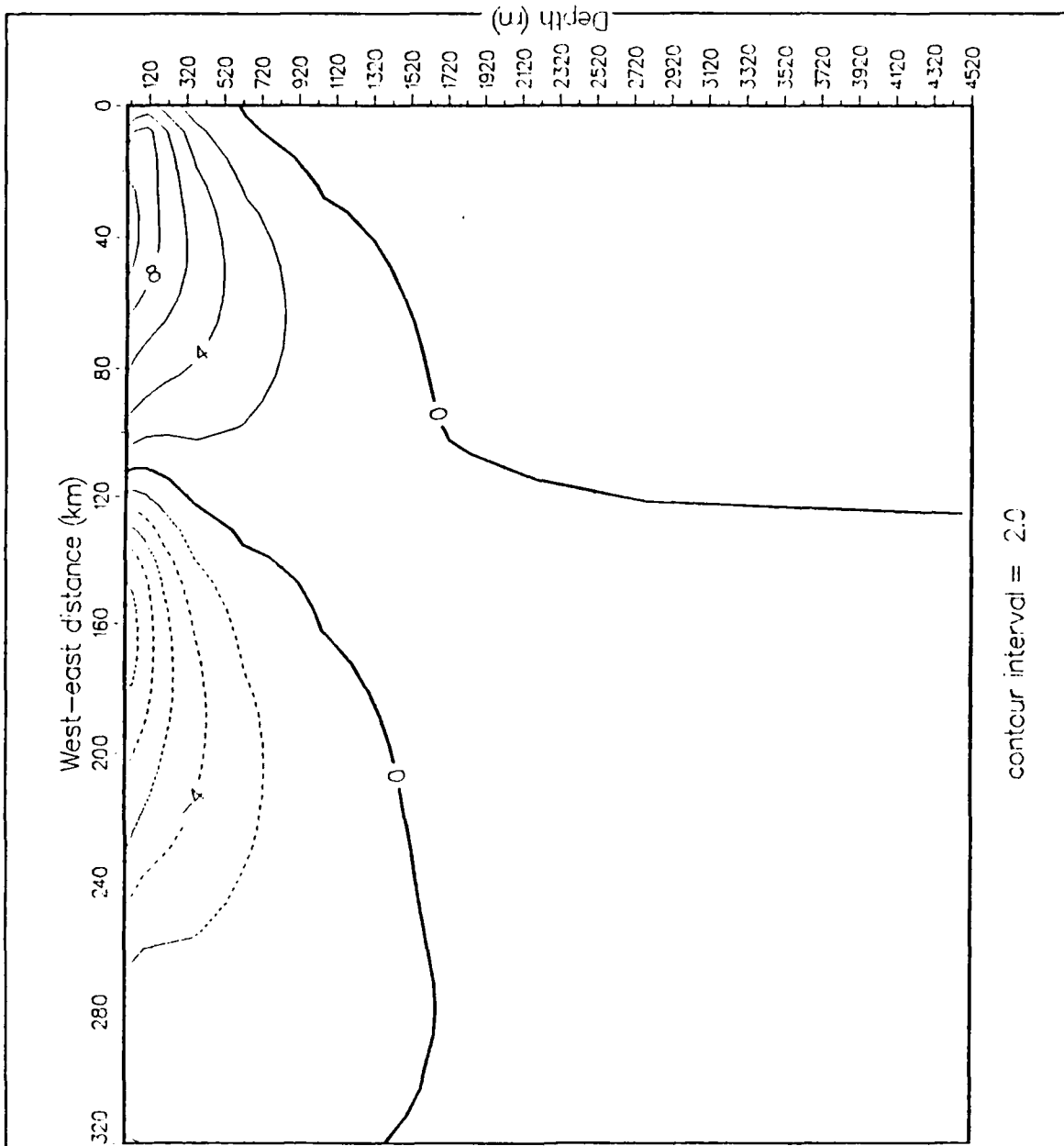


Figure 3.34 Vertical cross-shore section of meridional (v) velocity (cm s^{-1}) for Experiment 5 at day 110. Contour interval is 2.0 cm s^{-1} . Dashed contours denote equatorward velocities. The vertical cross section was alongshore-averaged.

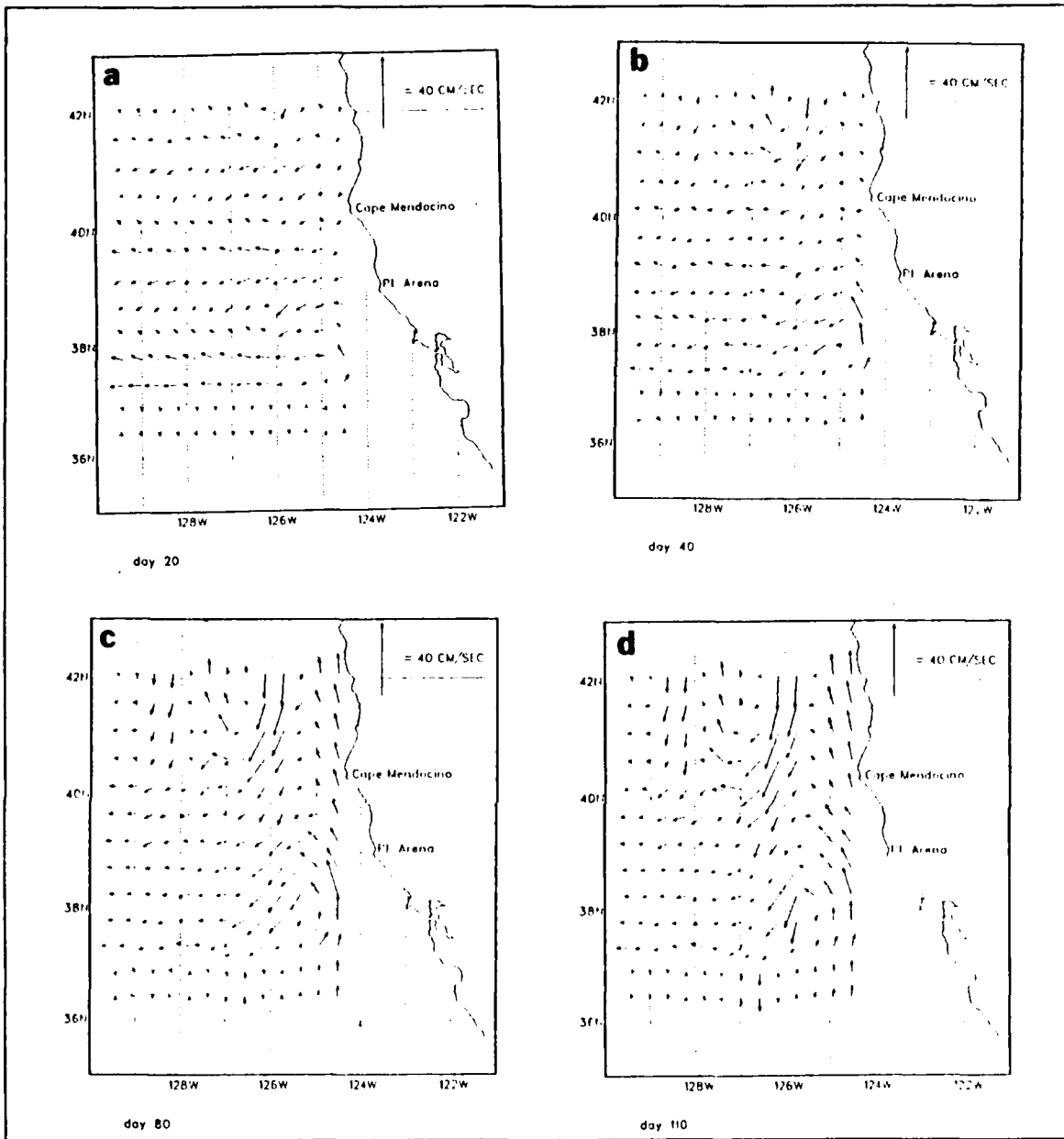


Figure 3.35 Surface current vectors for Experiment 5 at (a) day 20, (b) day 40, (c) day 80, and (d) day 110.

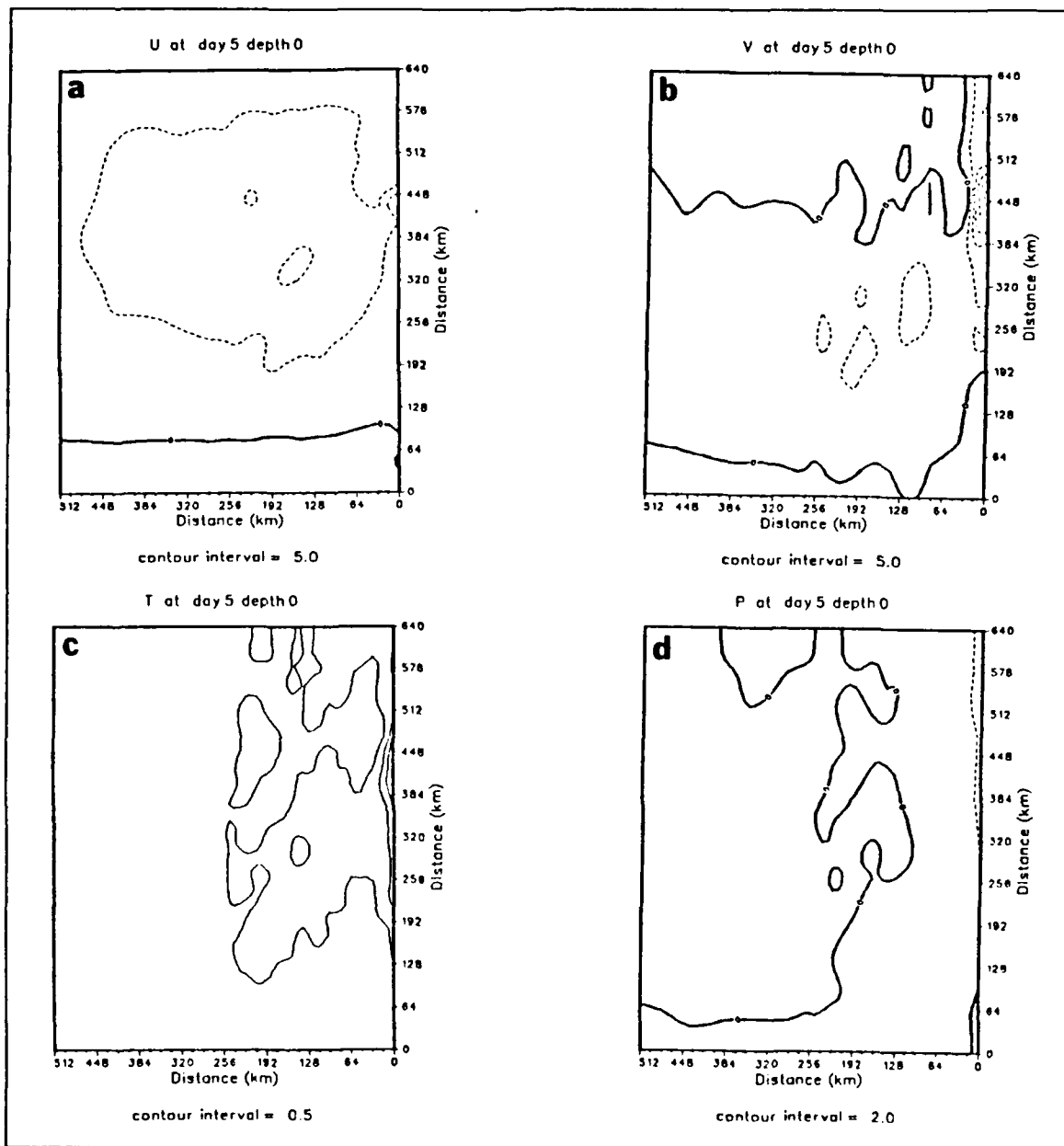


Figure 3.36 Surface isopleths of (a) zonal (u) velocity (cm s^{-1}), (b) meridional (v) velocity (cm s^{-1}), (c) temperature ($^{\circ}\text{C}$), and (d) dynamic height (cm) relative to 2400 m for Experiment 6 at day 5. Contour interval is 5.0 cm s^{-1} for (a) and (b), $0.5 \text{ }^{\circ}\text{C}$ for (c) and 2.0 cm for (d). Dashed contours denote offshore velocities in (a), equatorward velocities in (b) and negative values relative to 2400 m in (d).

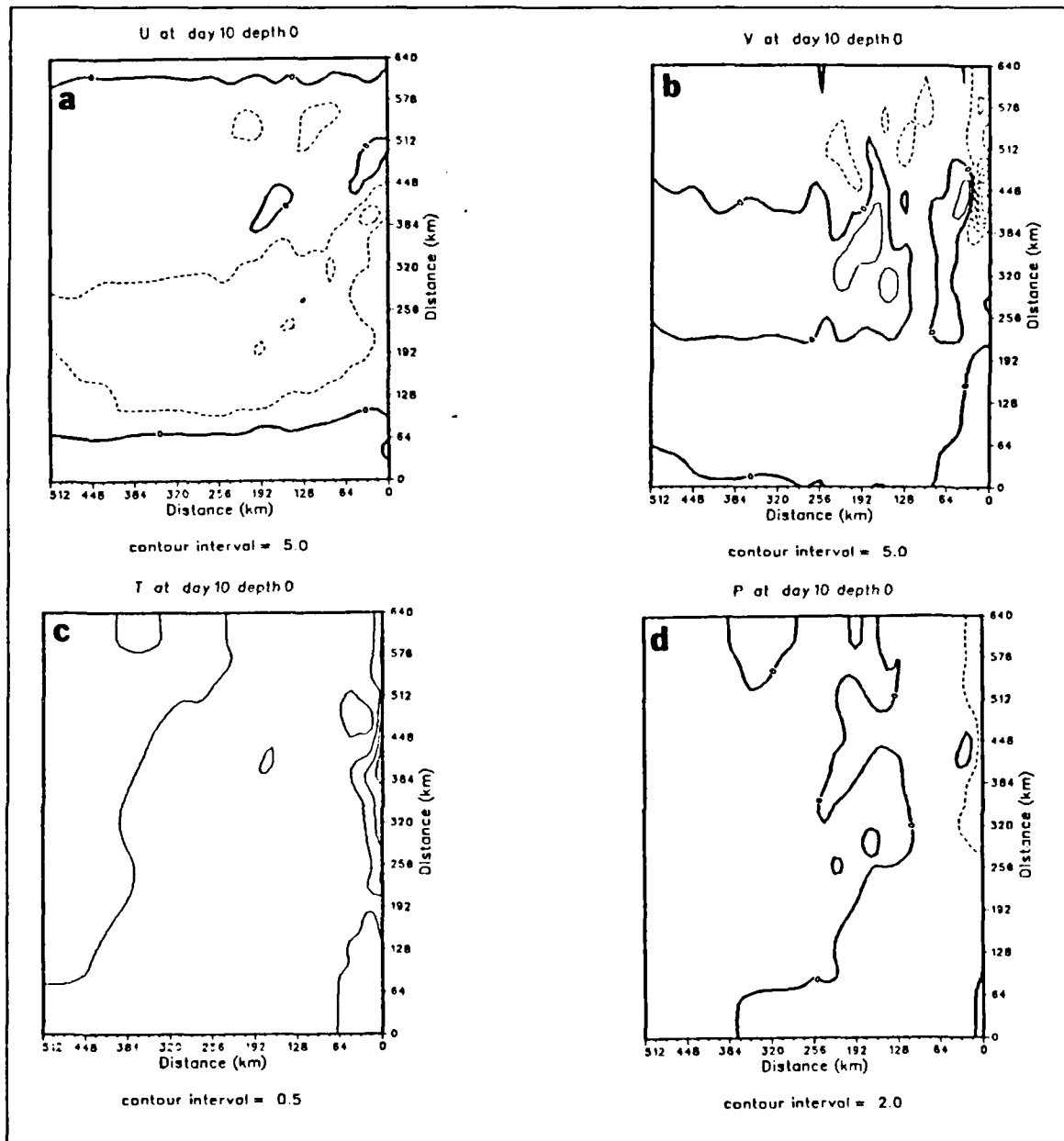


Figure 3.37 Surface isopleths of (a) zonal (u) velocity (cm s^{-1}), (b) meridional (v) velocity (cm s^{-1}), (c) temperature ($^{\circ}\text{C}$), and (d) dynamic height (cm) relative to 2400 m for Experiment 6 at day 10. Contour interval is 5.0 cm s^{-1} for (a) and (b), $0.5 \text{ }^{\circ}\text{C}$ for (c) and 2.0 cm for (d). Dashed contours denote offshore velocities in (a), equatorward velocities in (b) and negative values relative to 2400 m in (d).

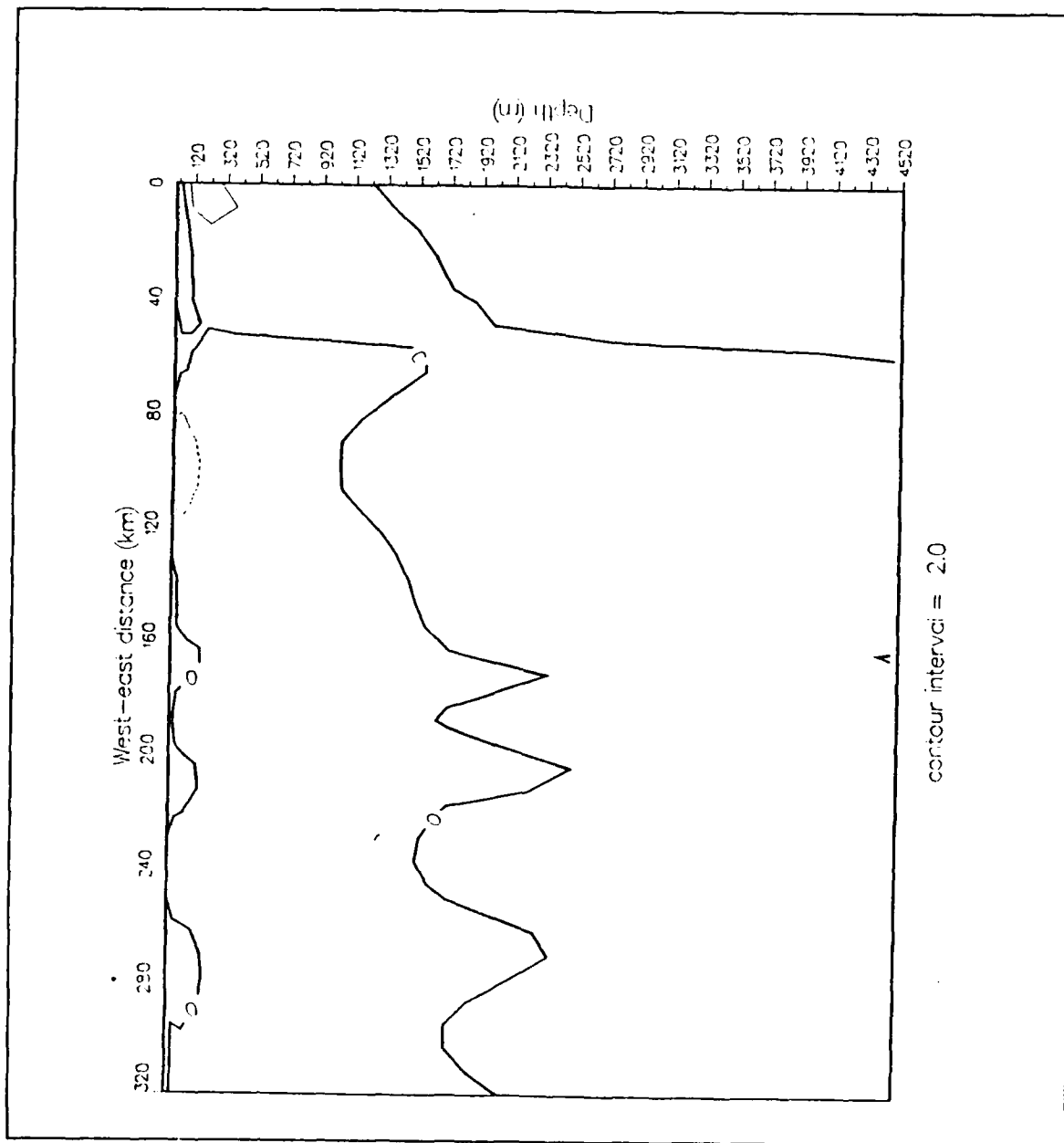


Figure 3.38 Vertical cross-shore section of meridional (v) velocity (cm s^{-1}) for Experiment 6 at day 10. Contour interval is 2.0 cm s^{-1} . Dashed contours denote equatorward velocities. The vertical cross section was alongshore-averaged.

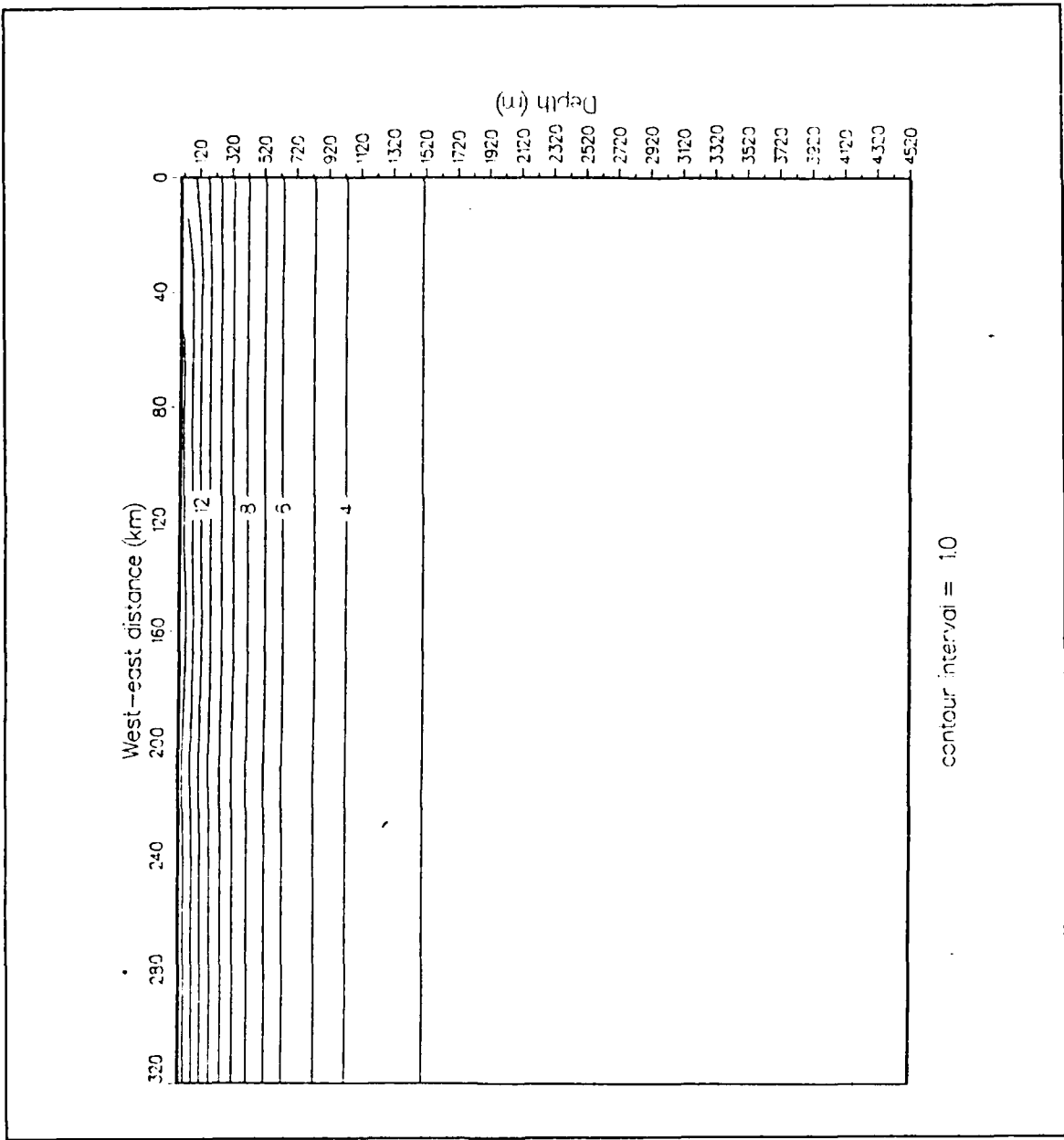


Figure 3.39 Vertical cross-shore section of temperature (°C) for Experiment 6 at day 10. Contour interval is 1.0 °C. The vertical cross-section was taken at $y = 390$ km.

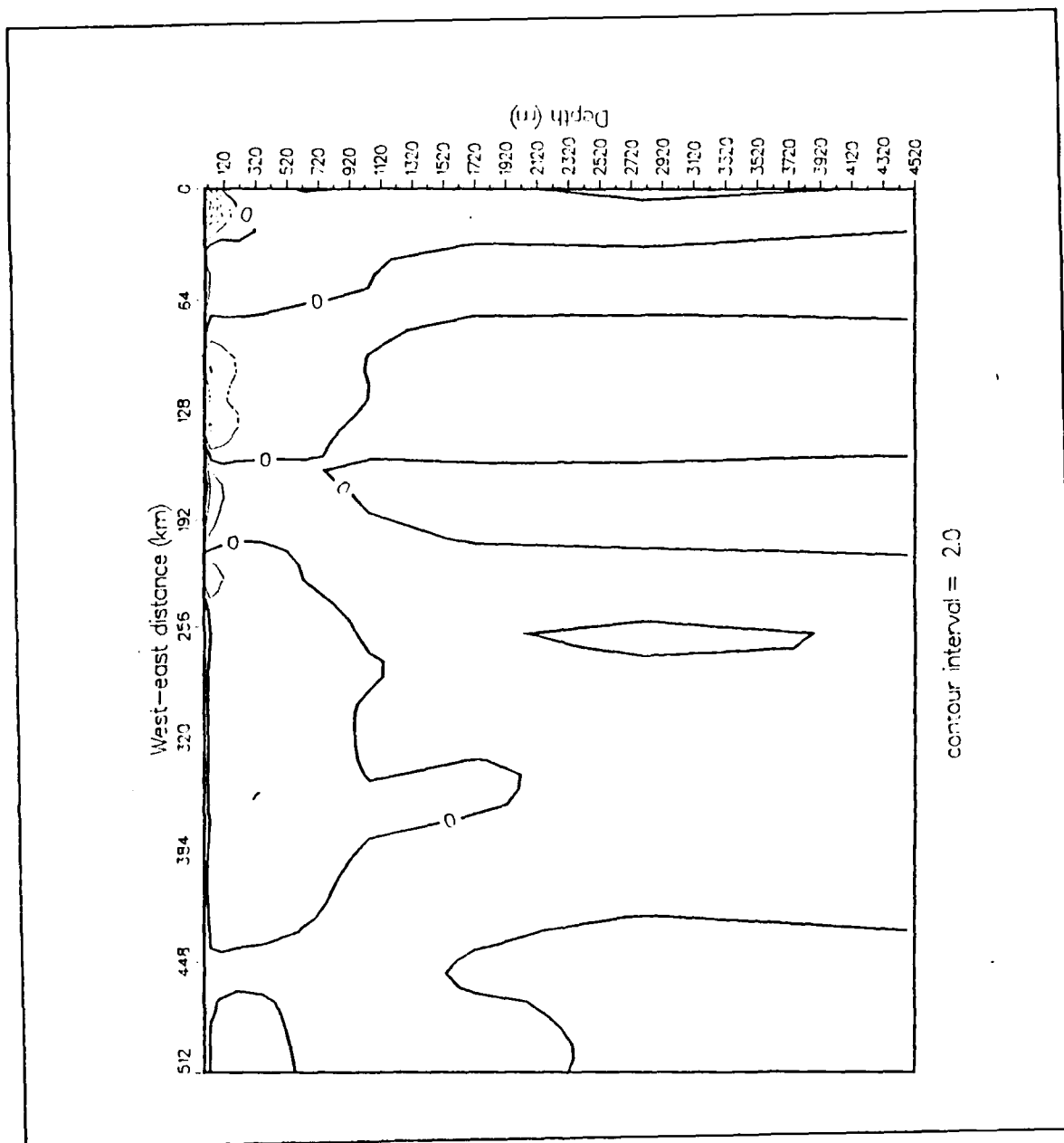


Figure 3.40 Vertical cross-shore section of meridional (v) velocity (cm s^{-1}) for Experiment 6 at day 10. Contour interval is 2.0 cm s^{-1} . Dashed contours denote equatorward velocities. The vertical cross section was taken at $y = 390$ km.

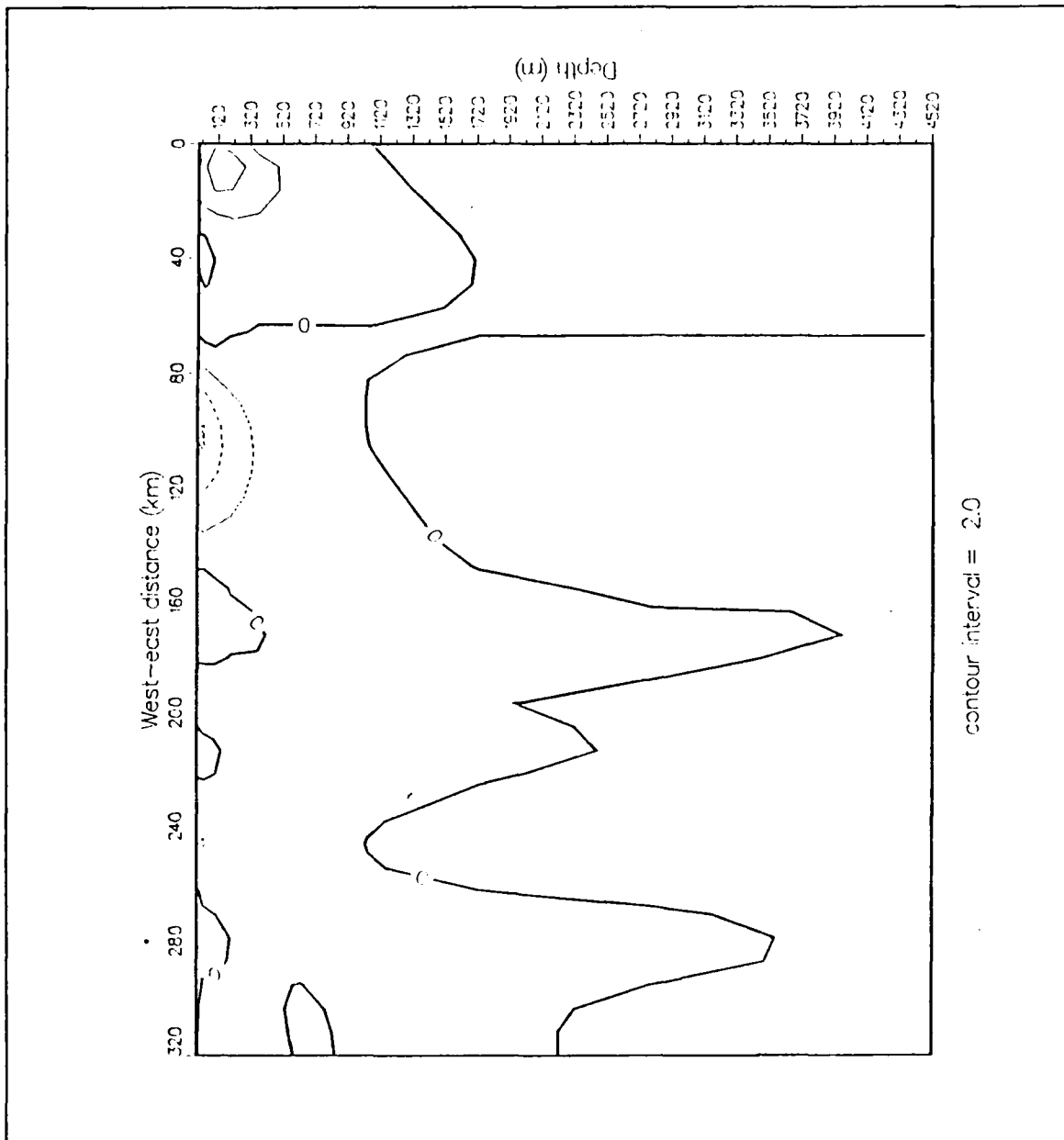


Figure 3.41 Vertical cross-shore section of meridional (v) velocity (cm s^{-1}) for Experiment 6 at day 20. Contour interval is 2.0 cm s^{-1} . Dashed contours denote equatorward velocities. The vertical cross section was alongshore-averaged.

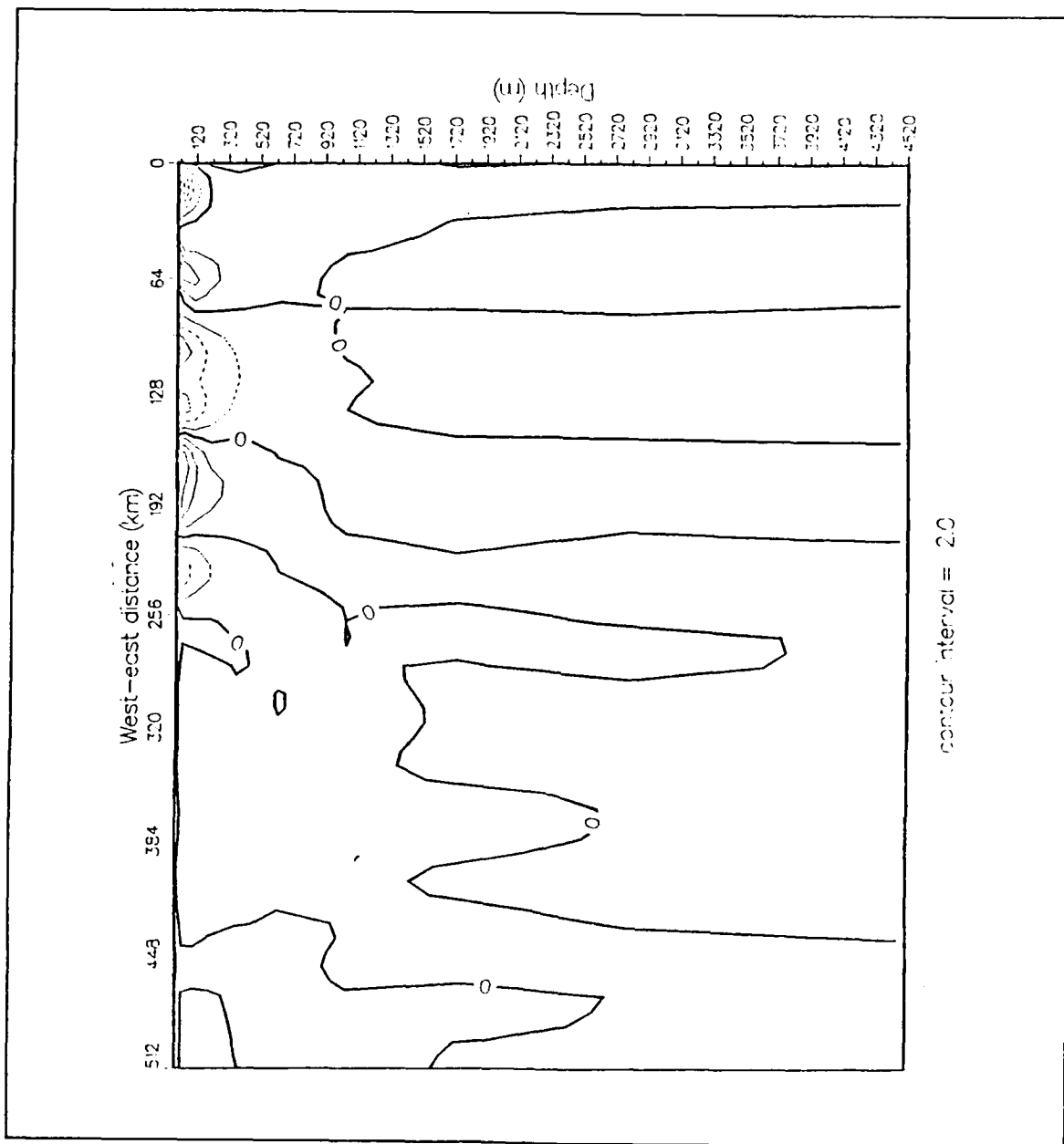


Figure 3.42 Vertical cross-shore section of meridional (v) velocity (cm s^{-1}) for Experiment 6 at day 20. Contour interval is 2.0 cm s^{-1} . Dashed contours denote equatorward velocities. The vertical cross section was taken at $y = 390 \text{ km}$.

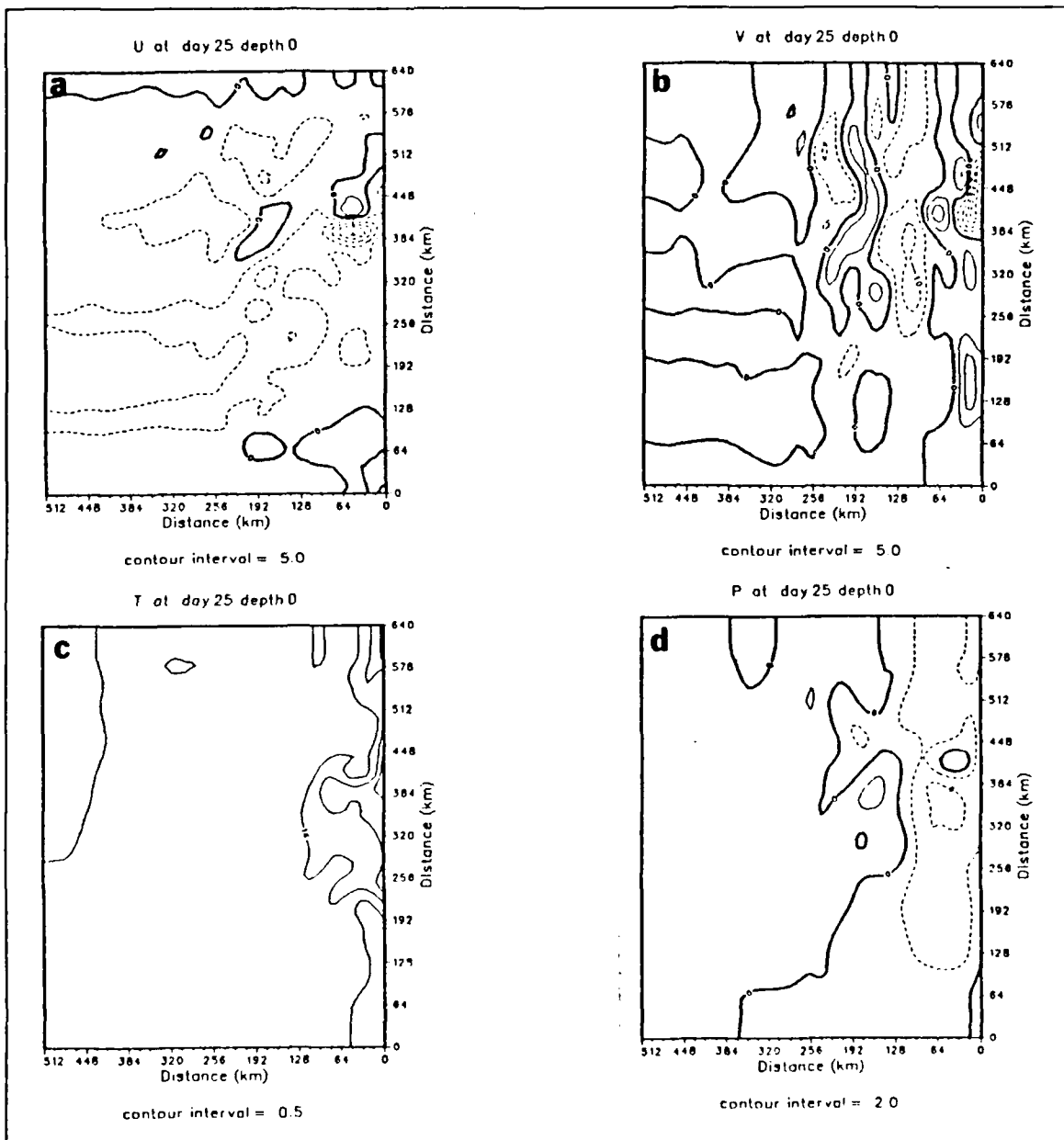


Figure 3.43 Surface isopleths of (a) zonal (u) velocity (cm s^{-1}), (b) meridional (v) velocity (cm s^{-1}), (c) temperature ($^{\circ}\text{C}$), and (d) dynamic height (cm) relative to 2400 m for Experiment 6 at day 25. Contour interval is 5.0 cm s^{-1} for (a) and (b), $0.5 \text{ }^{\circ}\text{C}$ for (c) and 2.0 cm for (d). Dashed contours denote offshore velocities in (a), equatorward velocities in (b) and negative values relative to 2400 m in (d).

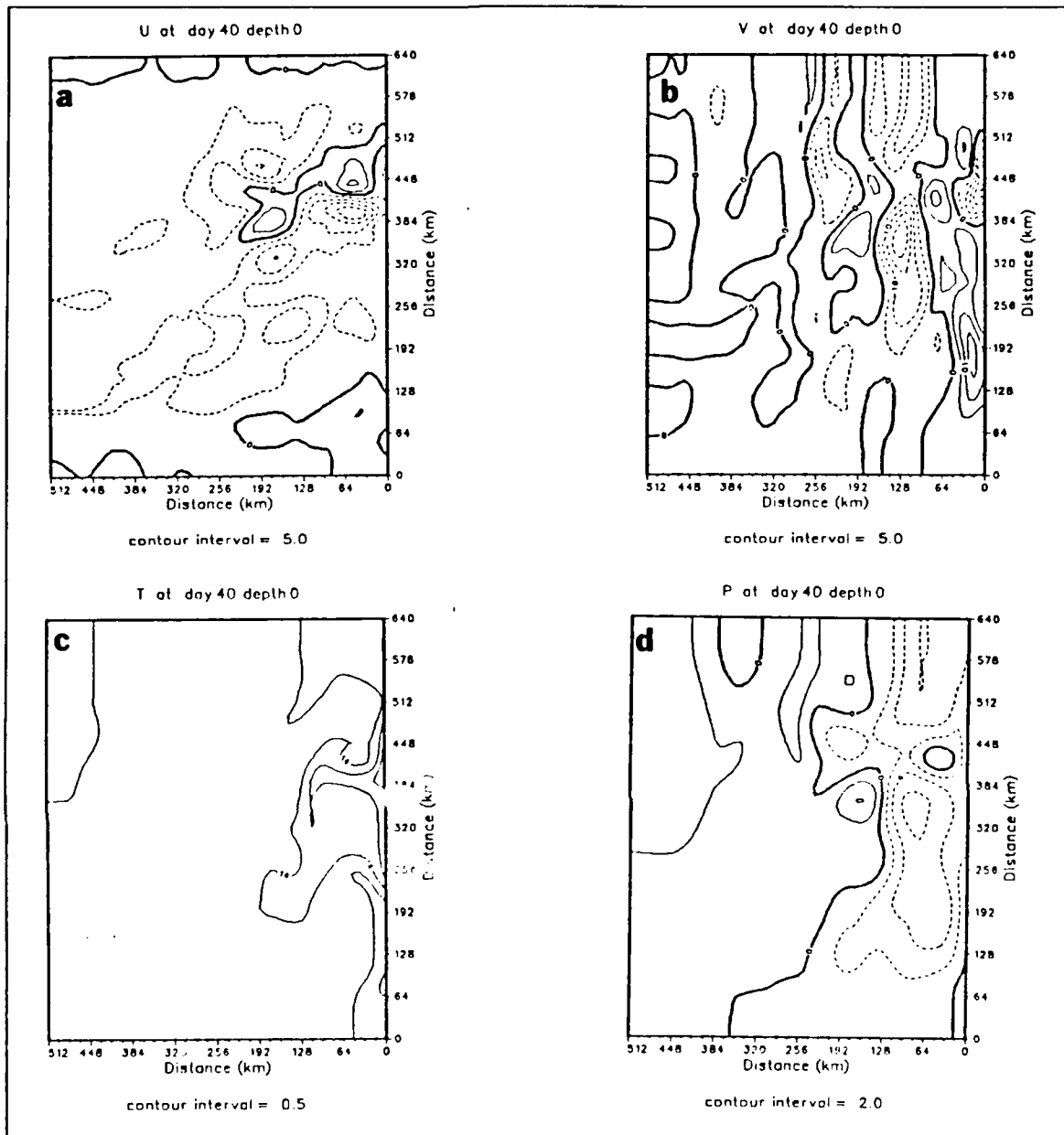


Figure 3.44 Surface isopleths of (a) zonal (u) velocity (cm s^{-1}), (b) meridional (v) velocity (cm s^{-1}), (c) temperature ($^{\circ}\text{C}$), and (d) dynamic height (cm) relative to 2400 m for Experiment 6 at day 40. Contour interval is 5.0 cm s^{-1} for (a) and (b), $0.5 \text{ }^{\circ}\text{C}$ for (c) and 2.0 cm for (d). Dashed contours denote offshore velocities in (a), equatorward velocities in (b) and negative values relative to 2400 m in (d).

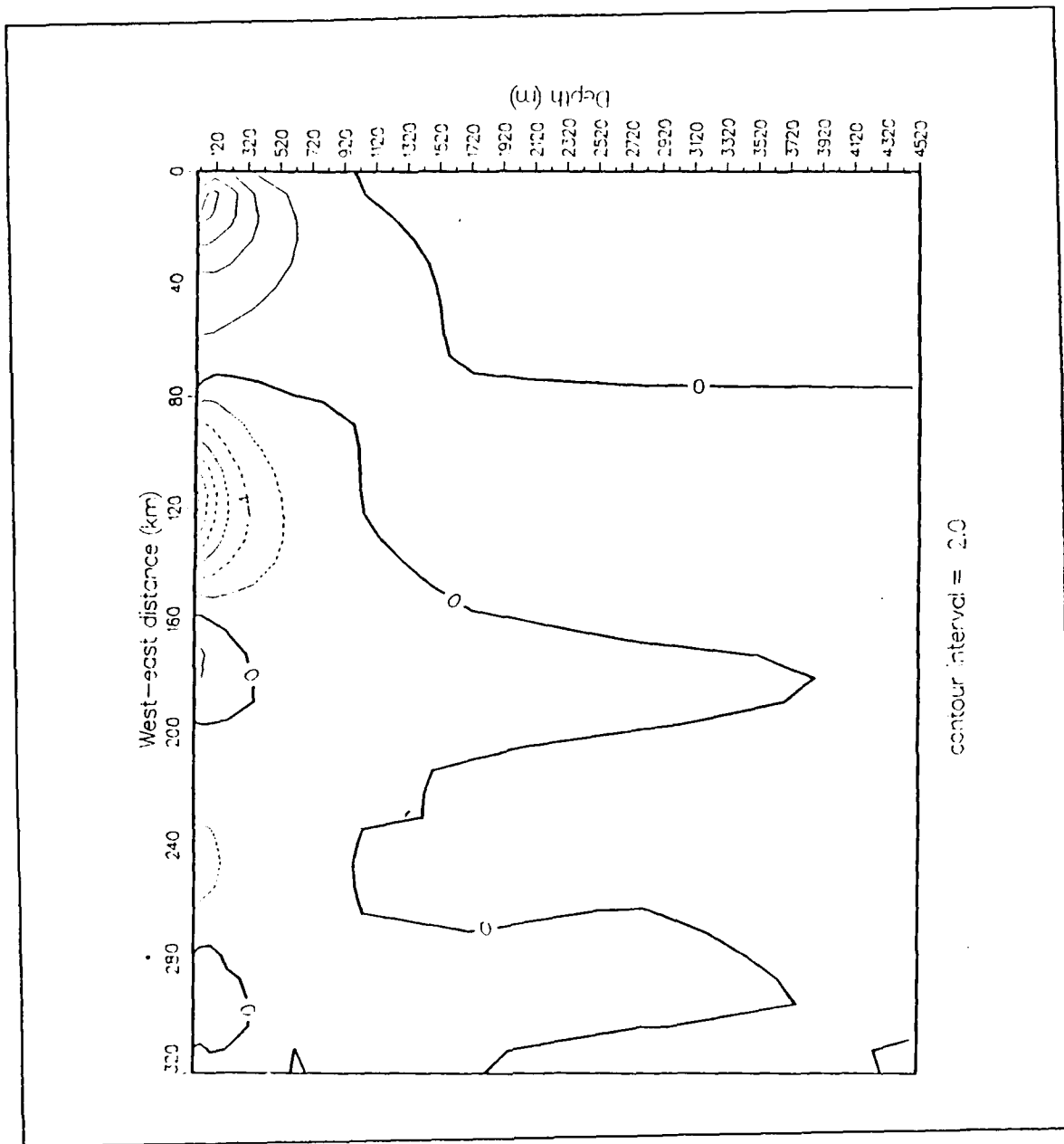


Figure 3.45 Vertical cross-shore section of meridional (v) velocity (cm s^{-1}) for Experiment 6 at day 40. Contour interval is 2.0 cm s^{-1} . Dashed contours denote equatorward velocities. The vertical cross section was alongshore-averaged.

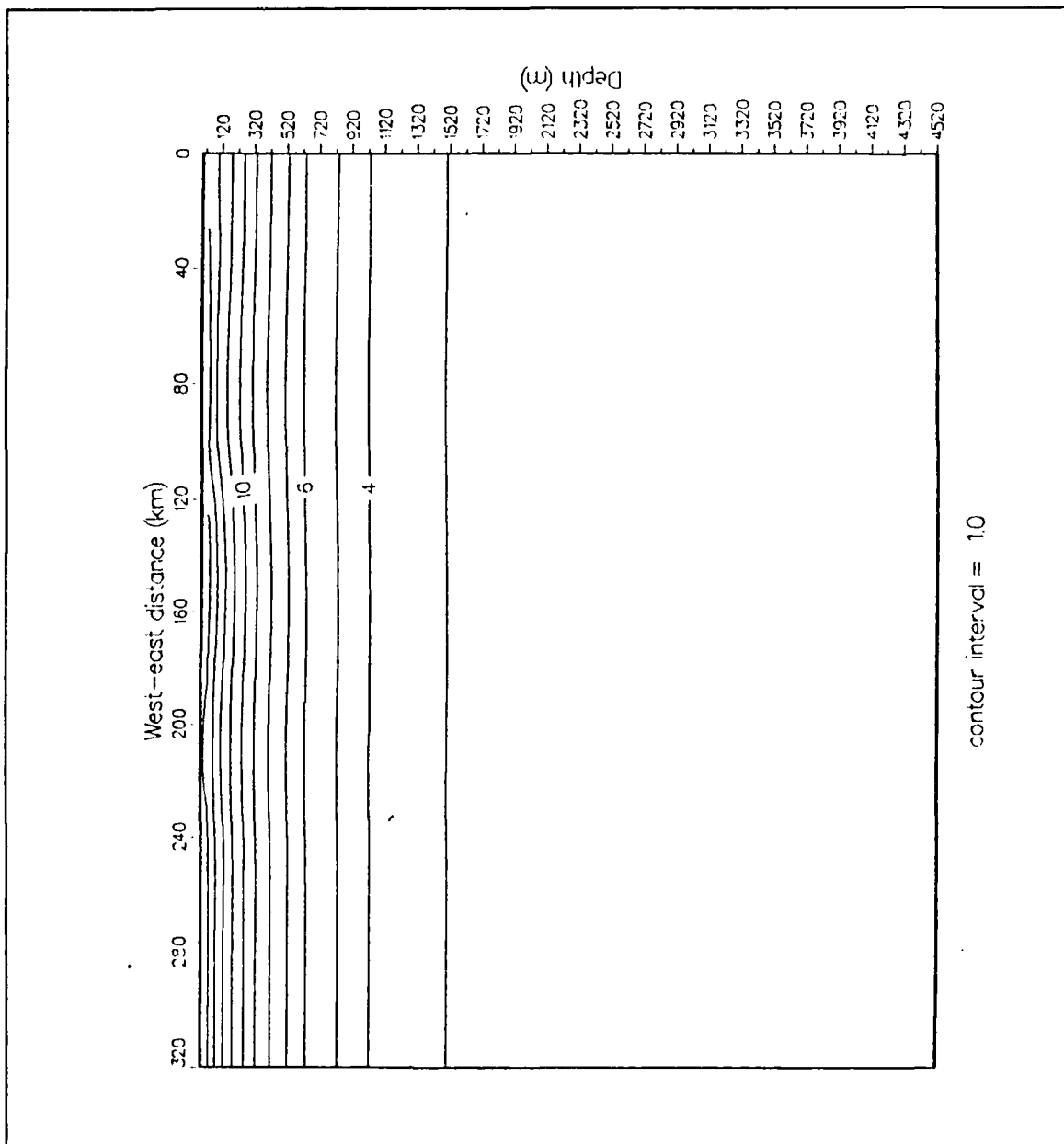


Figure 3.46 Vertical cross-shore section of temperature ($^{\circ}\text{C}$) for Experiment 6 at day 40. Contour interval is 1.0°C . The vertical cross-section was taken at $y = 390\text{ km}$.

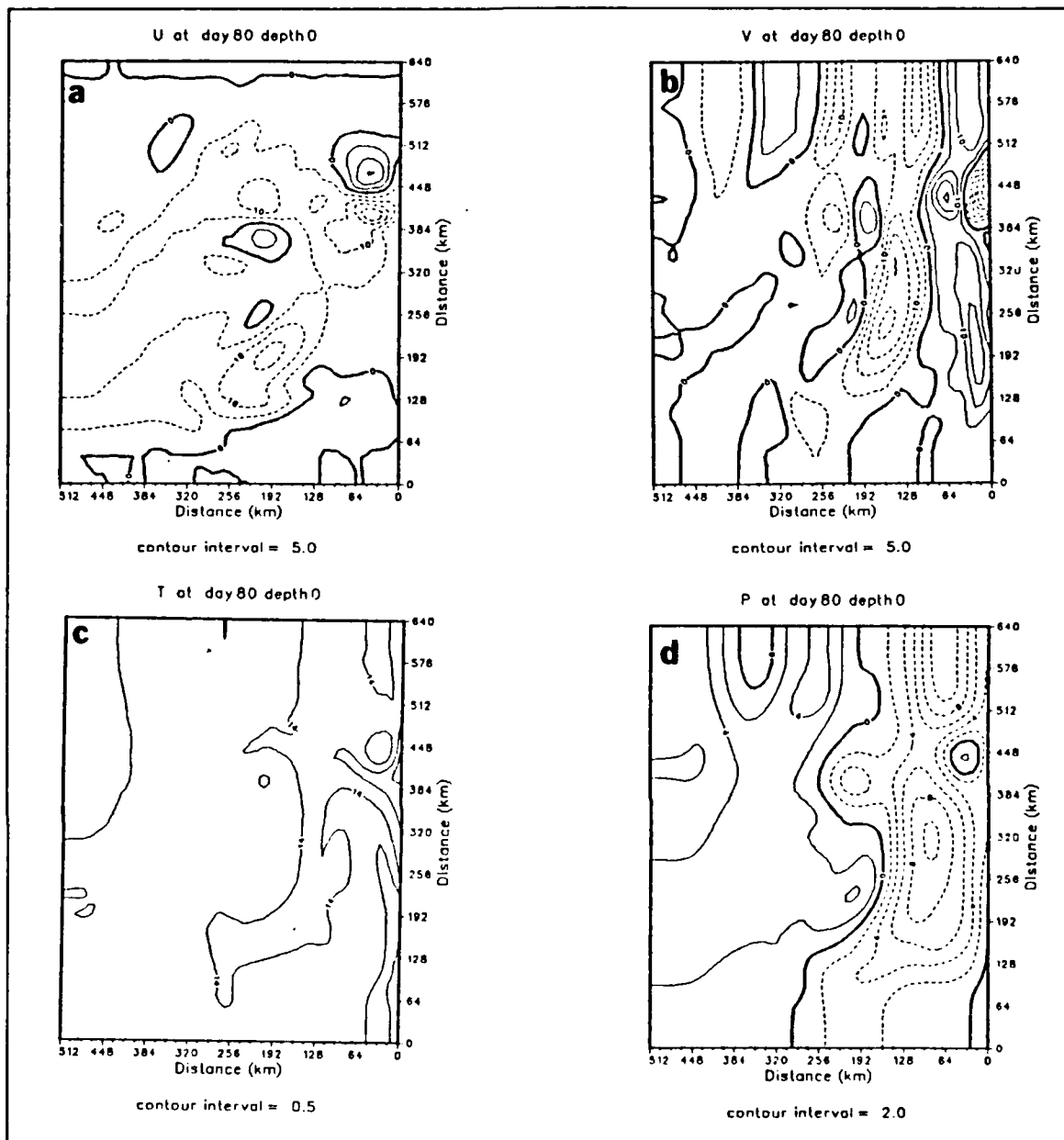


Figure 3.47 Surface isopleths of (a) zonal (u) velocity (cm s^{-1}), (b) meridional (v) velocity (cm s^{-1}), (c) temperature ($^{\circ}\text{C}$), and (d) dynamic height (cm) relative to 2400 m for Experiment 6 at day 80. Contour interval is 5.0 cm s^{-1} for (a) and (b), 0.5 $^{\circ}\text{C}$ for (c) and 2.0 cm for (d). Dashed contours denote offshore velocities in (a), equatorward velocities in (b) and negative values relative to 2400 m in (d).

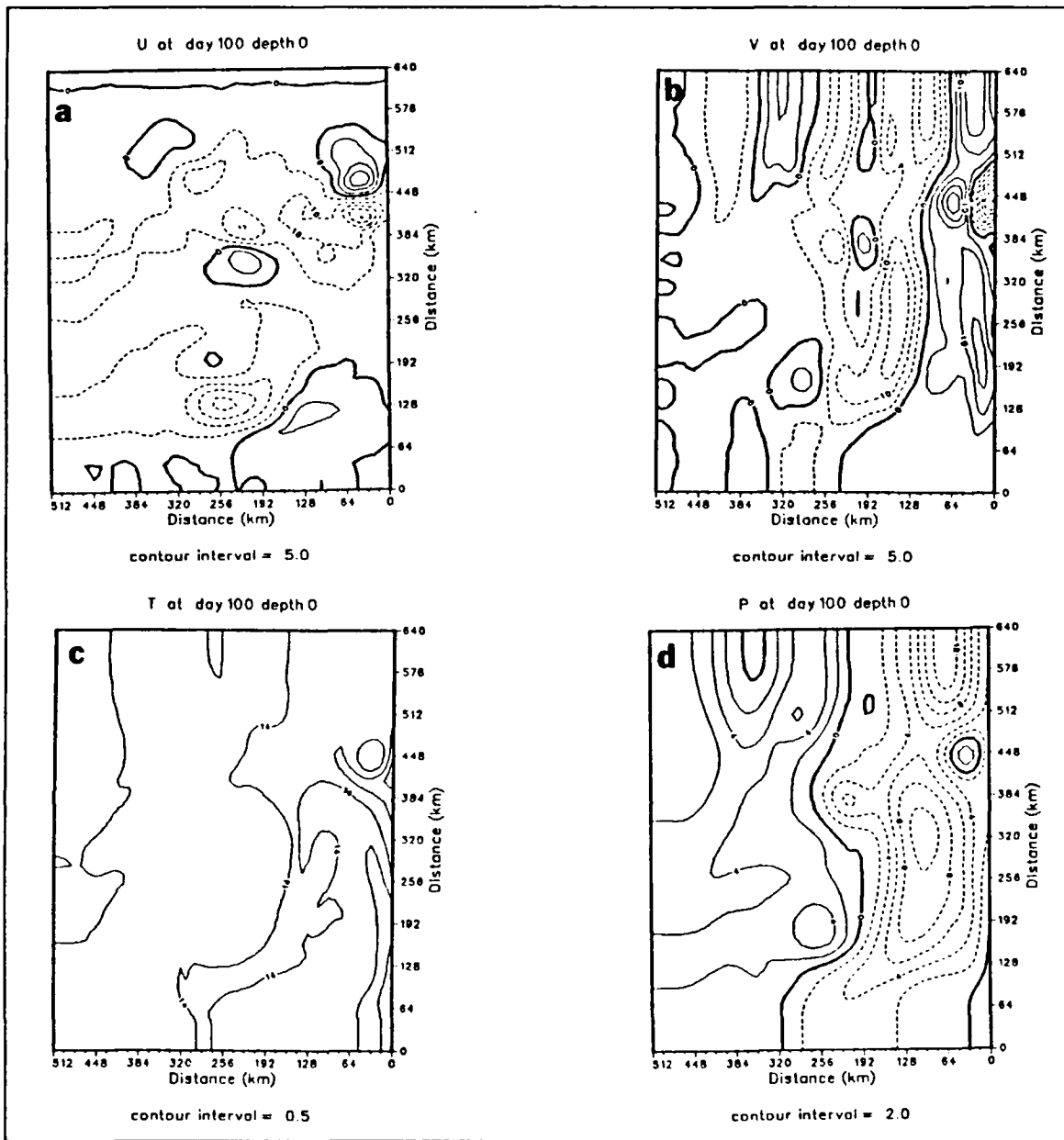


Figure 3.48 Surface isopleths of (a) zonal (u) velocity (cm s^{-1}), (b) meridional (v) velocity (cm s^{-1}), (c) temperature ($^{\circ}\text{C}$), and (d) dynamic height (cm) relative to 2400 m for Experiment 6 at day 100. Contour interval is 5.0 cm s^{-1} for (a) and (b), $0.5 \text{ }^{\circ}\text{C}$ for (c) and 2.0 cm for (d). Dashed contours denote offshore velocities in (a), equatorward velocities in (b) and negative values relative to 2400 m in (d).

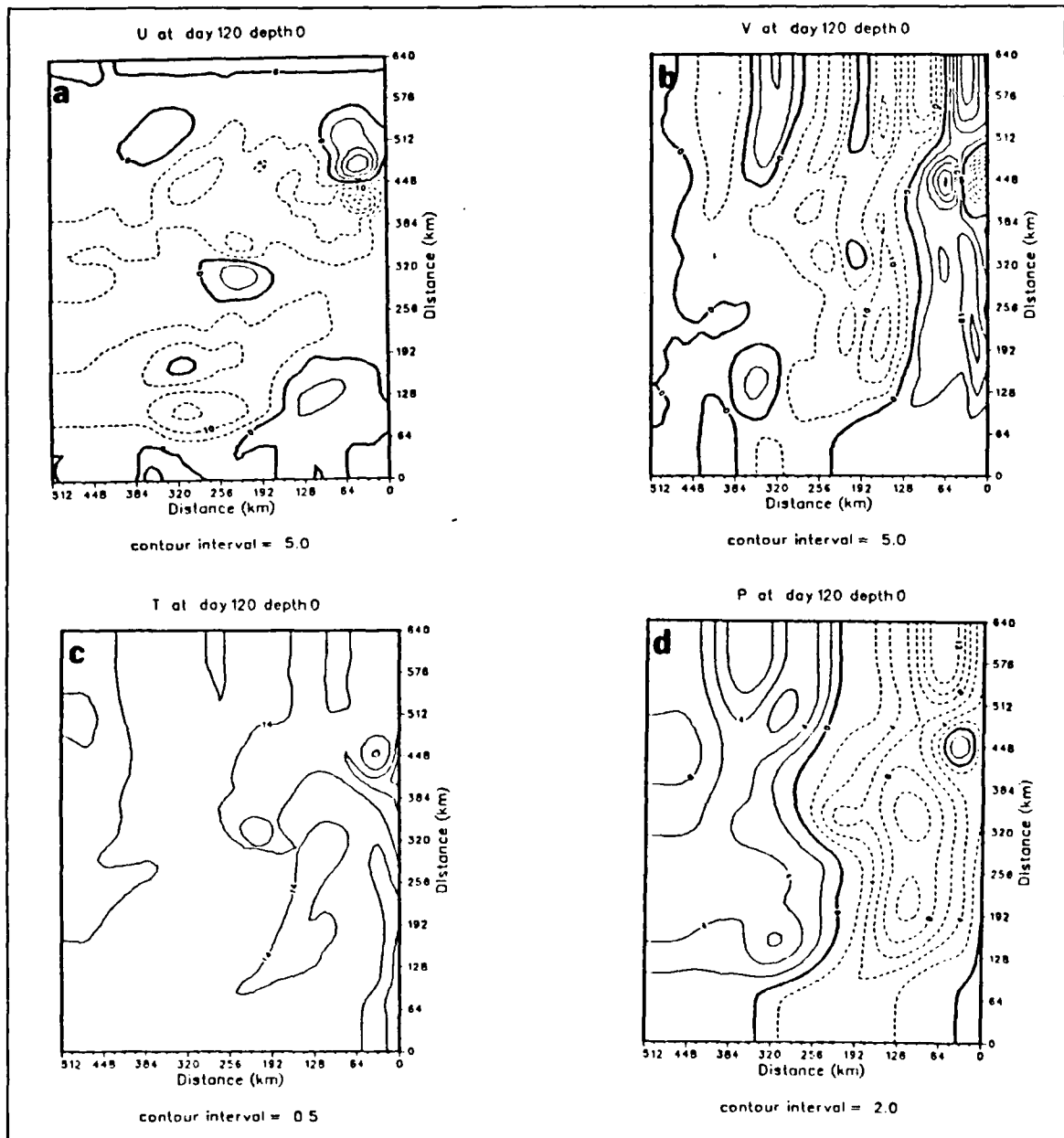


Figure 3.49 Surface isopleths of (a) zonal (u) velocity (cm s^{-1}), (b) meridional (v) velocity (cm s^{-1}), (c) temperature ($^{\circ}\text{C}$), and (d) dynamic height (cm) relative to 2400 m for Experiment 6 at day 120. Contour interval is 5.0 cm s^{-1} for (a) and (b), $0.5 \text{ }^{\circ}\text{C}$ for (c) and 2.0 cm for (d). Dashed contours denote offshore velocities in (a), equatorward velocities in (b) and negative values relative to 2400 m in (d).

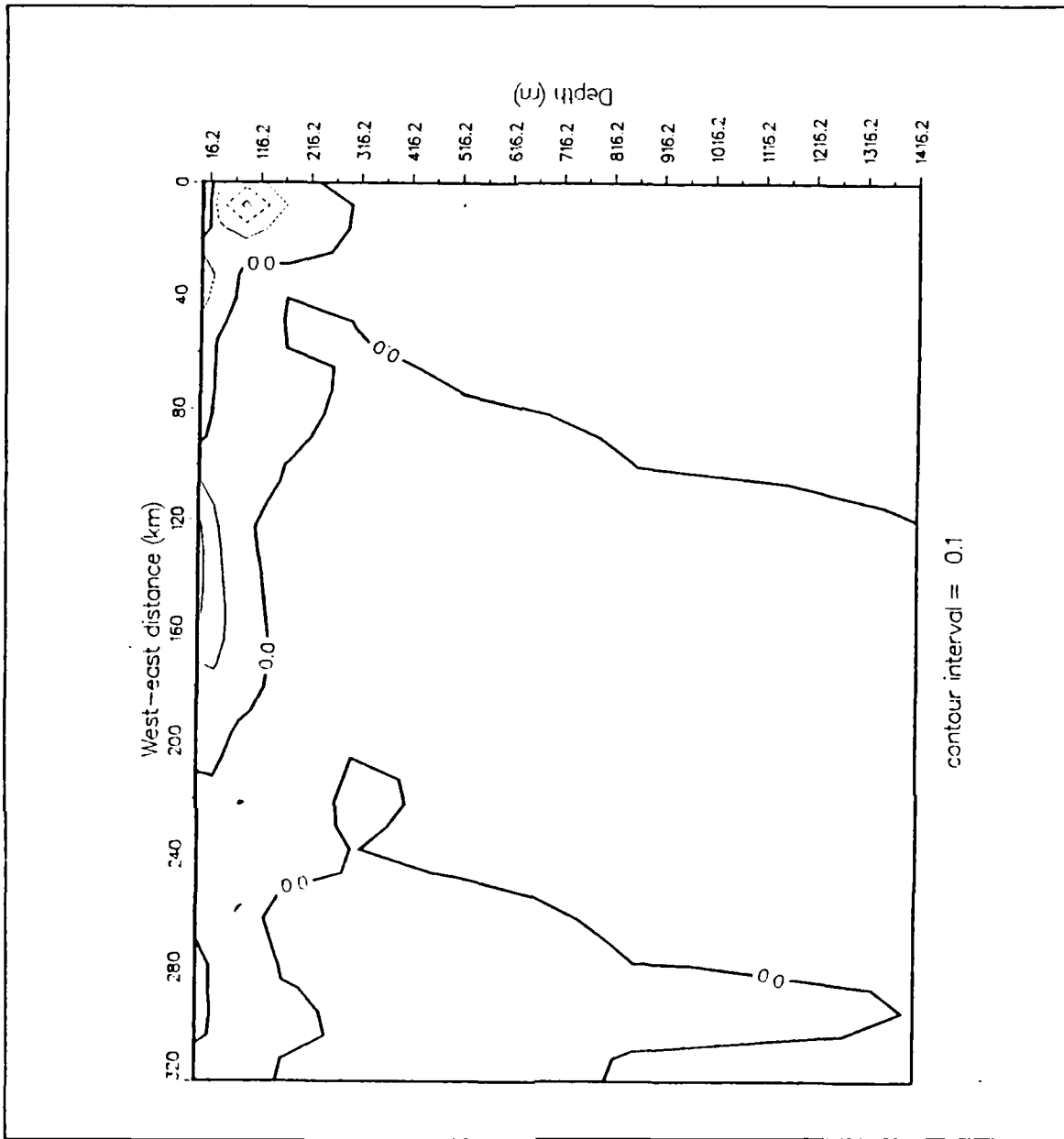


Figure 3.50 Vertical cross-section of the cross-stream derivative of potential vorticity multiplied by the grid size ($^{\circ}\text{C m}^{-1} \text{s}^{-1}$) scaled by 10^6 for the time-averaged days 90-99 of Experiment 5. Contour interval is $0.1^{\circ}\text{C m}^{-1} \text{s}^{-1}$. Dashed contours denote negative values. The vertical cross-section was alongshore-averaged.

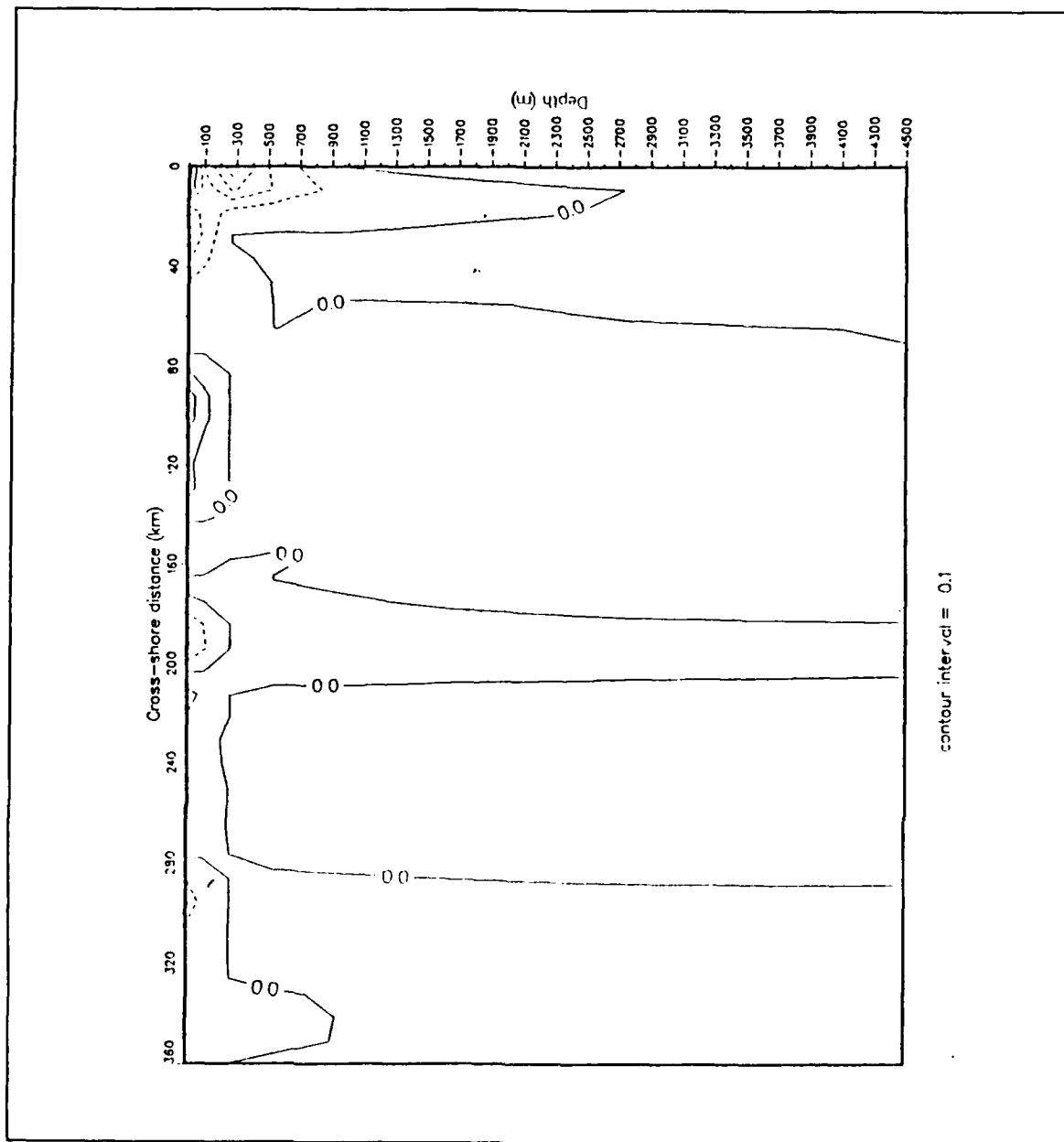


Figure 3.51 Vertical cross-section of the cross-stream derivative of potential vorticity multiplied by the grid size ($^{\circ}\text{C m}^{-1} \text{s}^{-1}$) scaled by 10^6 for the time-averaged days 5-15 of Experiment 6. Contour interval is $0.1^{\circ}\text{C m}^{-1} \text{s}^{-1}$. Dashed contours denote negative values. The vertical cross-section was alongshore-averaged.

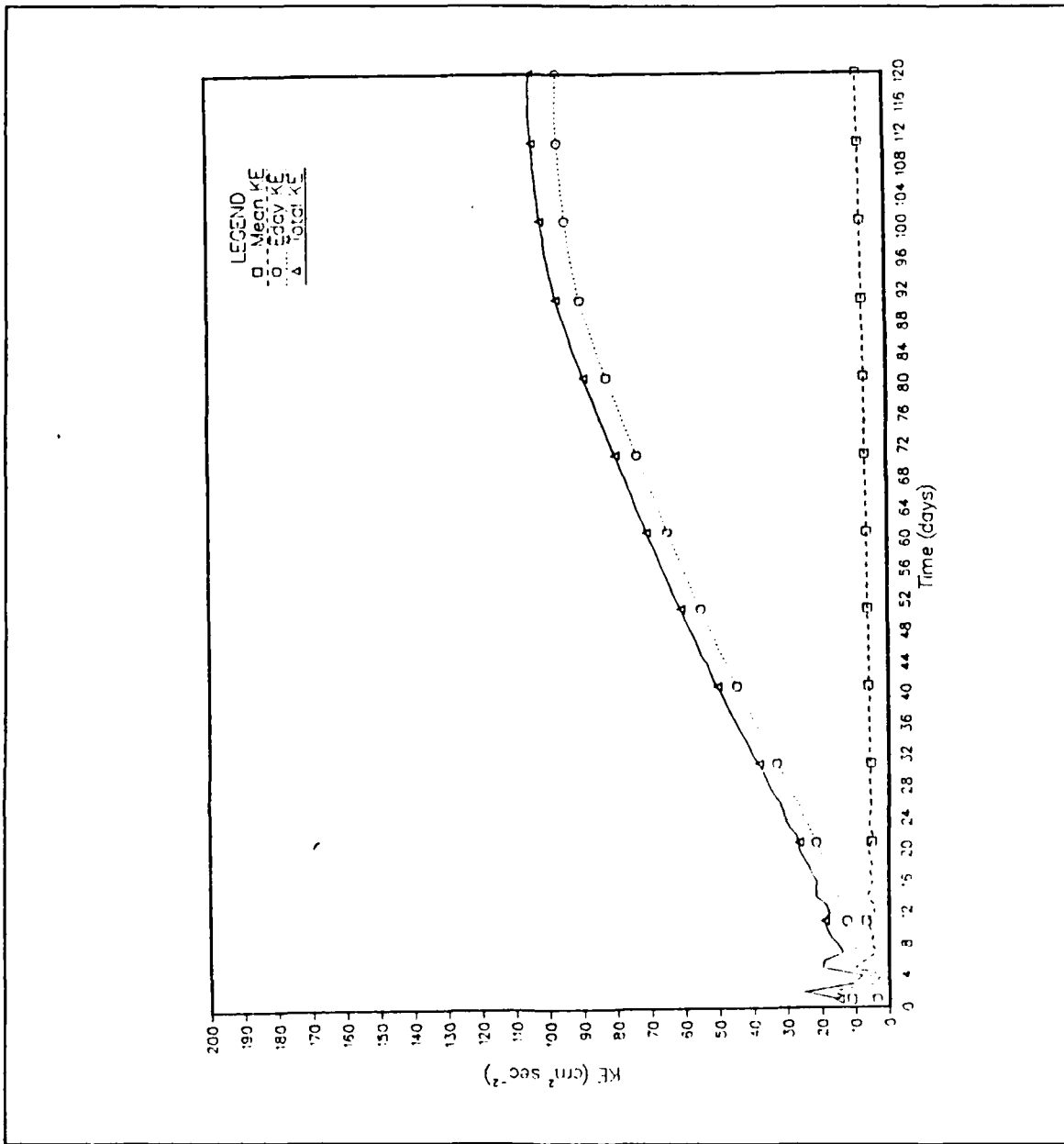


Figure 3.52 Kinetic energy (ergs cm⁻³) time series for Experiment 6.

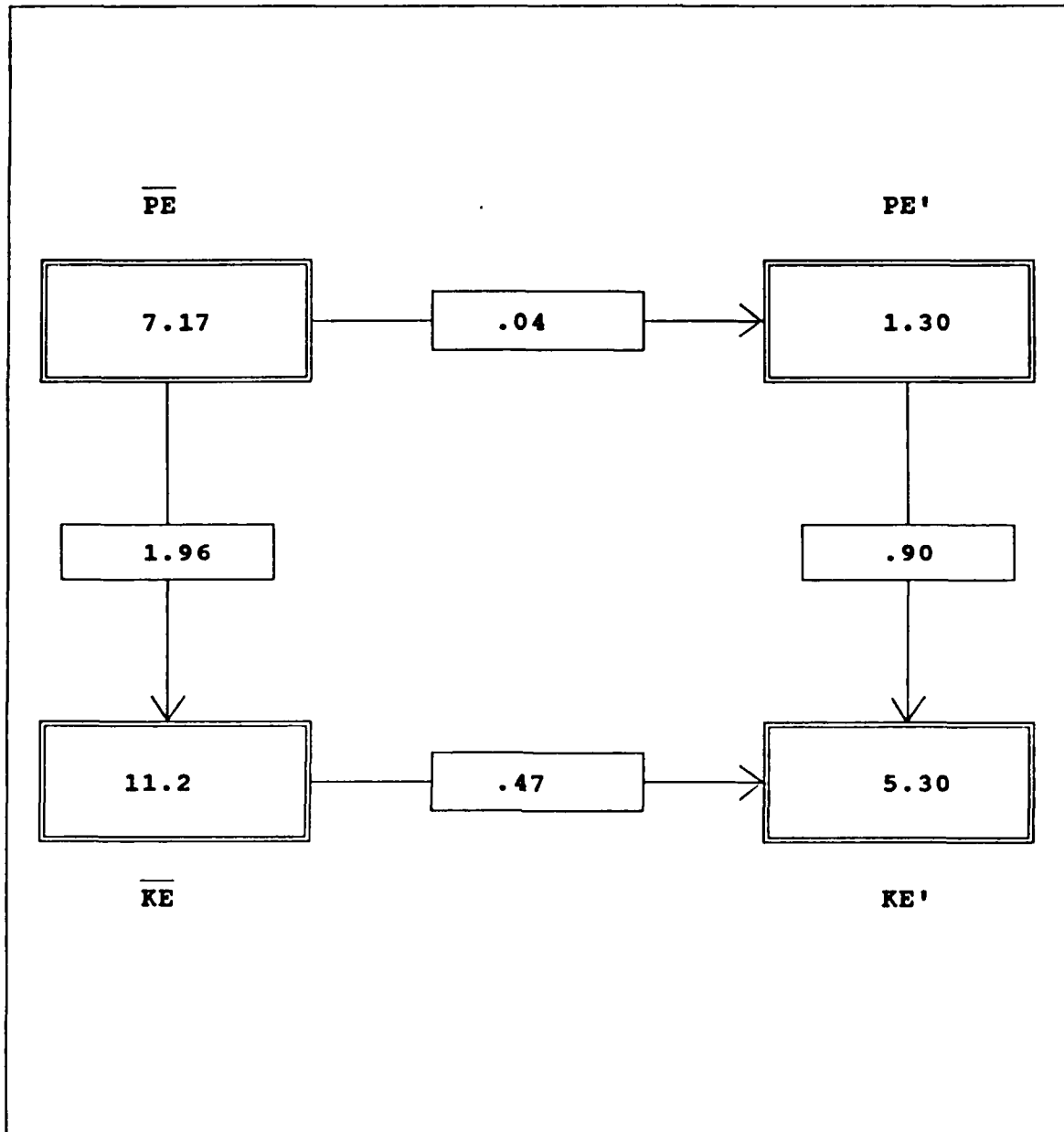


Figure 3.53 Basin-averaged energy diagram for days 1 to 12 of Experiment 6. Energies are in ergs cm^{-3} and transfer rates are in $10^6 \text{ ergs cm}^{-3} \text{ s}^{-1}$.

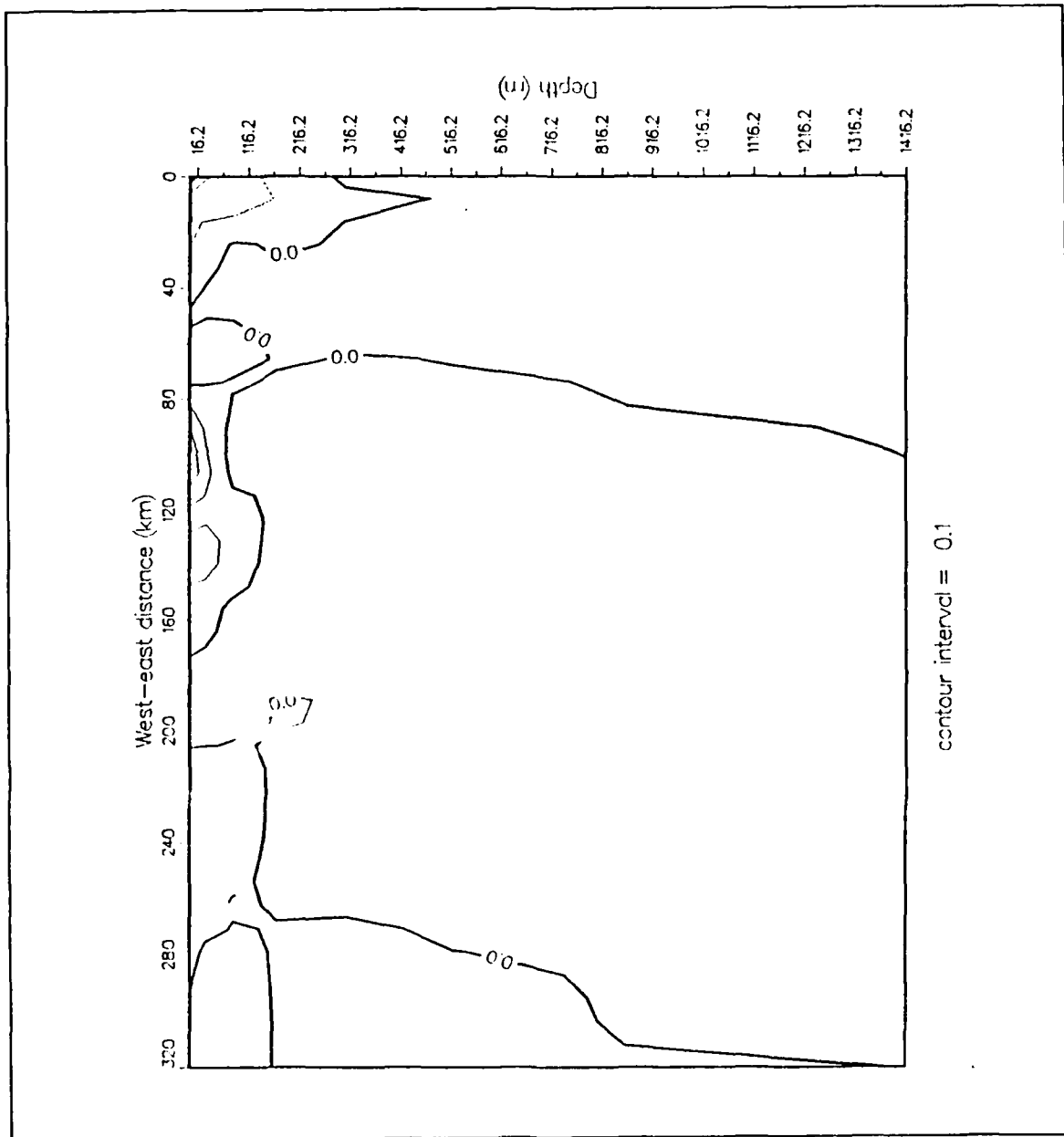


Figure 3.54 Vertical cross-section of the cross-stream derivative of potential vorticity multiplied by the grid size ($^{\circ}\text{C m}^{-1} \text{s}^{-1}$) scaled by 10^6 for the time-averaged days 100-120 of Experiment 6. Contour interval is $0.1^{\circ}\text{C m}^{-1} \text{s}^{-1}$. Dashed contours denote negative values. The vertical cross-section was alongshore-averaged.

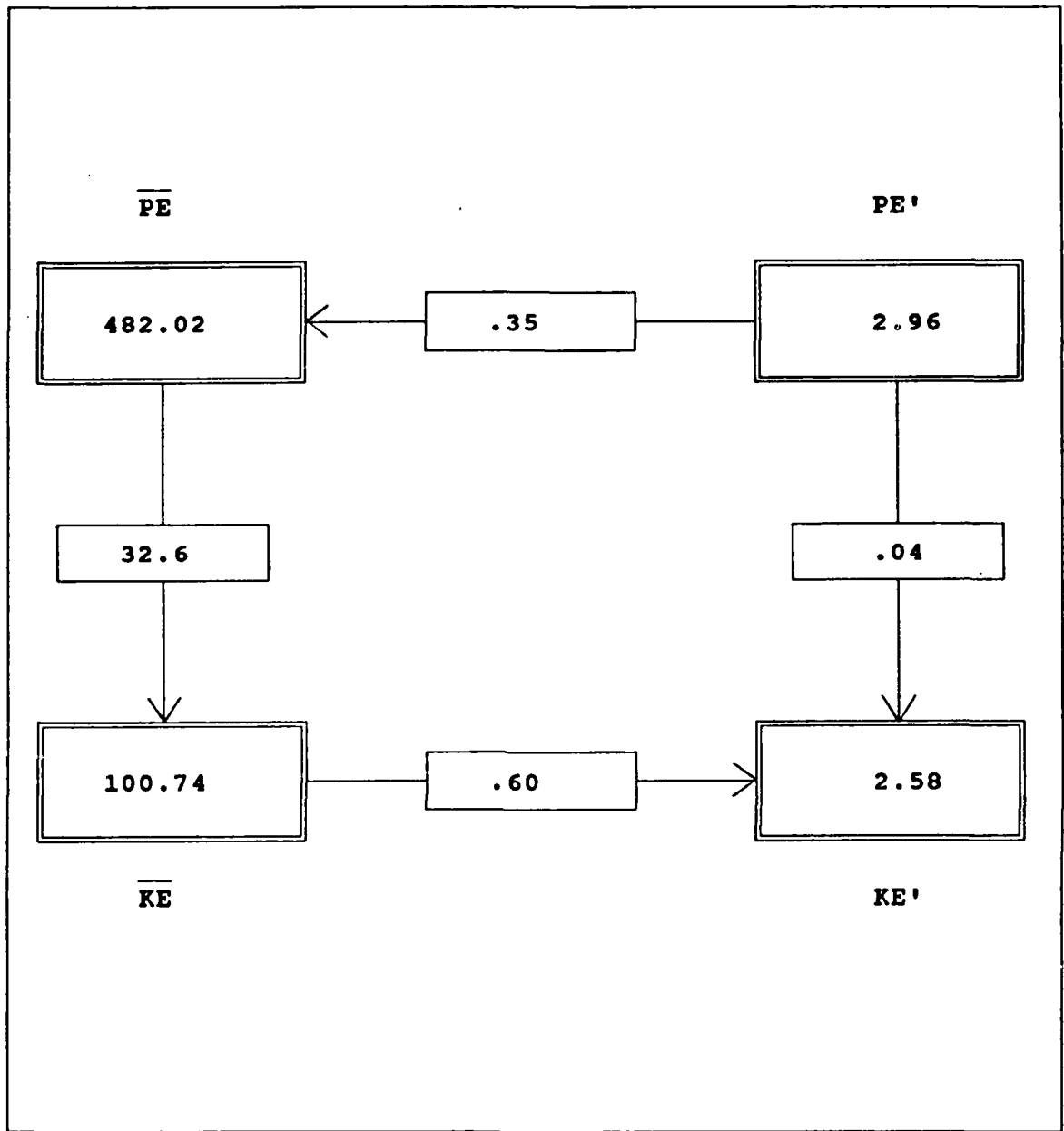


Figure 3.55 Basin-averaged energy diagram for days 100 to 120 of Experiment 6. Energies are in ergs cm⁻³ and transfer rates are in 10^6 ergs cm⁻³ s⁻¹.

IV. COMPARISON OF MODEL RESULTS WITH OBSERVATIONS

Quantitative comparisons of model results with actual observations are not easily done due to the diversity in the current field structure in the many experiments. However, a few assumptions can be made to assist in this comparison. First, equatorward flow exhibited anywhere in the nearshore region was considered a coastal jet. Secondly, poleward flow beneath the equatorward jet was considered an undercurrent even if this flow was contiguous with a northward surface current further offshore. Finally, values for Experiment 2 were taken at day 30 (June 30) during summer wind stress conditions. The resulting values are displayed in Table III with comparisons from Batteen *et al.* (1989) and various observational studies. Experiments 1 and 5 are not included in the table due to the lack of a coastal jet in these experiments.

As seen in Table III, the model gave widely varying results over the different experiments. No one experiment fit all the ranges of the observations, but several important comparisons can be made. The coastal jet of Experiment 2 (transient wind stress with a June 1 start) was weaker and narrower compared to observations. Additionally, the undercurrent velocity was too small. The other features, listed in the table, of both the coastal jet and undercurrent, do compare favorably with the observations. It should be noted, however, that no eddies or filaments developed in this experiment.

Experiment 3 (constant stress in the nearshore region) developed a reasonably strong, well defined coastal jet, but the undercurrent was too deep and wide. This

overdevelopment of the undercurrent could be a product of the much stronger coastal jet in this experiment. A stronger jet can lead to a larger alongshore pressure gradient and, therefore, a stronger poleward undercurrent.

Experiment 4 (climatological wind stress, constant in the nearshore region) exhibited the proper current structure except that the coastal jet was too weak. Additionally, the undercurrent was too wide and located too far offshore.

The results of Experiment 6 (two tenths degree climatological wind stress) showed a similar coastal jet structure as in Experiment 3, but a much shallower, narrower undercurrent. In Experiment 6 the coastal jet was confined to a relatively small region to the north at Cape Mendocino. Thus, the signal from the jet was greatly reduced due to its limited size. The jet in Experiment 6 was also the result of not only the strong stress in the region, but also the negative wind stress curl.

The results of Experiment 5 (not shown in the table) did show initial coastal jet development but this jet did not persist. The 14 cm s^{-1} velocity of a poleward surface current in Experiment 5, as well as the 4 cm s^{-1} velocity of this same current in Experiment 1 were considerably smaller than the observed peak velocities of 25 cm s^{-1} (Hickey, 1979).

In all experiments which developed eddies (Exps. 3-6), the size of the eddies compared well with the observations. There remained a discrepancy in zonal eddy velocity, however. The maximum eddy velocity of 40 cm s^{-1} was seen in Experiment 6. This velocity was still less than typical velocities observed during the CODE experiments (Kosro and Huyer, 1986). This can be attributed to the difference between the steady climatological wind stress values in the experiments and the much stronger

transient wind stress seen during CODE. It is interesting to note that the zonal eddy velocity obtained for Experiment 6 was at least twice as large as the other experiments including Batteen *et al.* (1989). This shows the importance of using the more representative, finer scale two tenths degree climatological wind forcing. The differences exhibited between observed and modeled values may also be a result of several modeling considerations: flat bottom rather than shelf / slope topography, transient rather than steady wind forcing, neglect of salinity and / or the climatological temperature profile used for the initial mean stratification (Batteen *et al.*, 1989).

The offshore equatorward flow seen in all the climatological forcing experiments (Exps. 3-6) also compares well to observations. The flow appears to be driven by the negative wind stress curl offshore (McCreary *et al.*, 1987).

The temperature fields of Experiment 6 exhibited filamentous structures which closely resemble the cold water plumes seen in many recent satellite observations. Kelly (1985) found that the plumes can extend offshore 200 km or more. Other filaments have been observed as long as 400 km (Ikeda and Emery, 1984). The filament of Experiment 6 extended to ~ 288 km before fragmenting, which compares favorably with these observations. The characteristic T-shaped termination of the initial modeled filament has also been observed in the field (Ikeda and Emery, 1984).

The variable current structure around Cape Mendocino in Experiment 6 correlates well with recent work done by Magnell and Winant (1987). Current meter data taken by them during the NCCCS program shows predominantly southward flow north of Cape Mendocino (Fig. 4.1a) and predominantly northward flow south of the Cape (Fig. 4.1b). (The placement of the current meters is shown in Figure 4.2.) This

opposing current pattern about Cape Mendocino is seen throughout Experiment 6 and is clearly illustrated in Figure 3.48, the meridional velocity field for day 120. The concept that spatial variations in wind stress leads to convergence of surface currents and the formation of a cold filament is also consistent with the work of Kelly (1985). Spatial variability in the wind field clearly has a significant effect on the oceanic response of the CCS, particularly in the development of opposing surface currents.

As several studies have indicated, it is possible that poleward flow driven by the positive curl at the coast is the normal flow in many regions of the CCS (Hickey, 1979; Chelton *et al.*, 1987). It is only when equatorward wind stress of significant intensity is present that the equatorward flow overcomes this poleward current with a resulting coastal jet (Hickey, 1979; McCreary *et al.*, 1987).

Overall the model results compare quite favorably with available observations, particularly in the structure and form of the current systems that develop. Most notable of these correlations is the opposing currents and cold filaments which develop in Experiment 6.

TABLE III Instantaneous comparison of model experiments (EXP.) with model results of Batteen *et al.* (1989) (BATTEEN) and observations (OBS.) of the CCS.

	OBS.	BATTEEN (Day 90)	EXP. 2 (Day 30)	EXP. 3 (Day 95)	EXP. 4 (Day 110)	EXP. 6 (Day 110)
Maximum coastal jet velocity (cm s ⁻¹)	30 - 80	15-20	8	45	8	40
Offshore location of coastal jet (km)	2.5 - 35	25-35	16	48	16	8
Offshore extent of coastal jet (km)	> 40	70-75	40	96	32	32
Depth of inshore coastal jet (m)	90 - 150	140-150	< 70	170	70	400
Maximum vertical shear of coastal jet ($\times 10^3$ s ⁻¹)	< 2.9	8-9	< 1.1	2.6	1.1	1.0
Maximum undercurrent velocity (cm s ⁻¹)	5 - 15	4-6	4	10	4	10
Offshore location of undercurrent axis (km)	10 - 40	10	10	15	70	12
Maximum width of undercurrent (km)	10 - 20	15-30	30	55	X	X
Depth of undercurrent axis (m)	200 - 300	300-330	200	620	120	70
Maximum zonal eddy diameter (km)	10 - 100	50-60	-	128	50 - 60	64
Maximum zonal eddy velocity (cm s ⁻¹)	50 - 80	20	-	15	6	40

References: (1) Kosro and Huyer (1986)
 (2) Huyer and Kosro (1987)
 (3) Kosro (1987)
 (4) Davis (1985)
 (5) Mooers and Robinson (1984)

X - Undercurrent extended entire width of coastal jet, surfacing offshore as a poleward current.

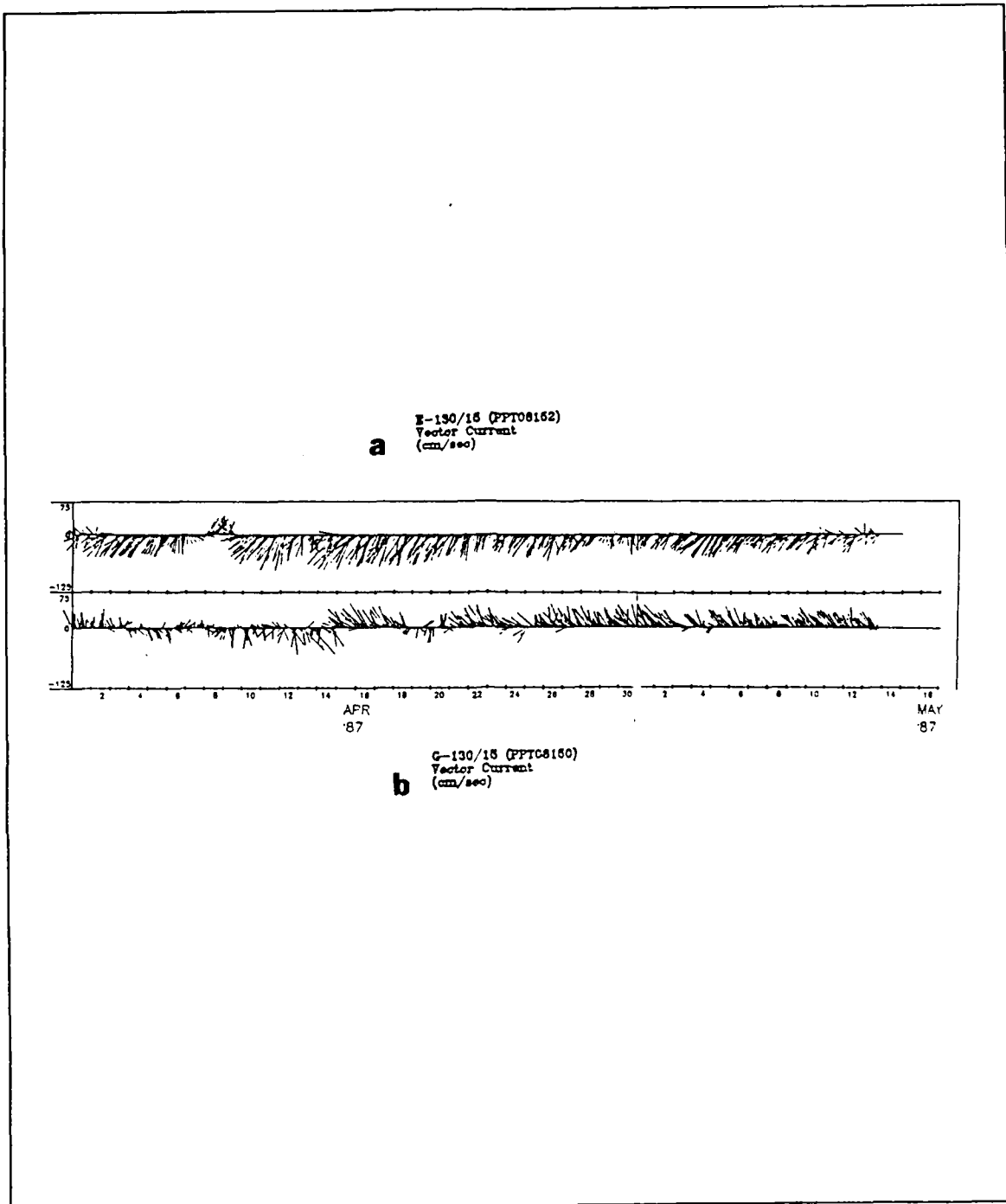


Figure 4.1 Current vector time series for a station (a) north of Cape Mendocino and a station (b) south of Cape Mendocino. Data from the NCCCS Program (from Magnell and Winant, 1987).

V. SUMMARY AND RECOMMENDATIONS

A. SUMMARY

This study used a high-resolution primitive equation model to study the effects both of transient and climatological wind forcing on eddy generation in the California Current System. An annually periodic wind forcing function with zonal variability, was used as transient forcing in an idealized, flat-bottom eastern boundary current model in several experiments. One degree and two tenths degree steady wind stress data, varying in x and y, were also used as climatological forcing in other experiments. In addition, stability analyses were made to describe any types of instability that occurred.

Experiments 1 and 2 utilized a periodic wind stress function for their forcing. In Experiment 1, since the curl component of the forcing was stronger than the stress, a surface poleward flow developed in the nearshore region with an equatorward flow offshore. This structure is similar to that of the Davidson Current during the winter although the modelled current was weaker than observed. At the end of the simulation, a coastal jet was beginning to form and move southward, denoting the beginning of the upwelling season. In Experiment 2, due to the stronger stress compared to the curl, a coastal jet developed with an undercurrent. Again, though, because the proportion of wind stress to wind stress curl decreased in the forcing, a poleward surface flow started to dominate and by late July, the coastal jet disappeared. No eddies were seen in either of these experiments due to the lack of a lasting jet / undercurrent structure and the resultant instability. These results support the findings of McCreary *et al.*

(1987), that wind stress curl is important in developing the Davidson Current in the winter season as well as the poleward surface flow seen throughout the year. It is also important in forming the equatorward offshore current. When the equatorward wind stress is sufficiently strong, a baroclinic equatorward surface jet develops, which overrides the poleward flow and forms an undercurrent.

Experiment 3 tested the application of a spatially varying steady climatological wind stress forcing in the offshore region and constant stress in the nearshore region. A strong coastal jet and a very large undercurrent developed. Large eddies formed, but had sluggish velocities compared to observations. The nearshore forcing was changed to be zonally constant in Experiment 4. In this case eddies developed near the shore, but were smaller in diameter and slower than observations. The current structure was more realistically sized, but still too slow compared to observed values. In both of these experiments there was no curl at the coast. The offshore area, with its spatially varying wind field and curl, did form well developed equatorward and poleward surface currents which were not seen in other steady forcing studies, as in Batteen *et al.* (1989).

The wind stress forcing of Experiment 5 was comprised exclusively of spatially varying one degree climatological wind stress data with positive curl along the coast. Although an equatorward jet was initially present, it was relatively weak and was soon overwhelmed by poleward surface flow from the south. The offshore region again exhibited the equatorward surface current. Some signs of eddy development were just beginning to show when the Experiment was terminated at day 110. In this experiment it would appear that the wind stress curl was strong relative to the stress

component and as such the curl was the dominant driving mechanism in the current system. The results were similar to those of Experiment 6 in that the where curl increased in strength in the fall season and overpowered the wind stress. However, the resolution of the wind field was too coarse to allow for the forcing of opposing current structures and the subsequent formation of filaments and eddies as a result of this convergence.

The final experiment, Experiment 6, utilized one degree climatological wind stress forcing in the offshore region and two tenths degree wind stress data in the region within 255 km of the coast. Again there was a positive curl in the coastal region, but the scale of the data was such that the forcing led to the formation of opposing currents. In the area near Cape Mendocino, there was a convergence in the surface flow which led to the development of a well defined cold filament. Additionally, the current structure was stronger than Experiment 5, with velocity values more representative of observations. The eddies formed during this experiment were of moderate size with maximum zonal velocities which compared quite well with previous observational studies. It is apparent from these results that spatial variability in the wind field is important for obtaining realistic current and eddy structures in the CCS.

Energy analyses were made for both Experiments 5 and 6. Since the eddies of Experiment 5 were still relatively weak at the time the experiment was completed, the analysis was inconclusive as to the type of instability occurring. Qualitatively, it was seen that analysis of the horizontal shear and potential vorticity showed that barotropic instability could be important. There was a shift in energy mechanisms during the time span of the Experiment 6. During the first 12 days, when the nearshore eddies were

forming, baroclinic instability was dominant. Later, as eddies began to be formed offshore, barotropic instability was dominant. Thus, during the model runs of this research both baroclinic and barotropic instability processes were present.

A final note can be made concerning the formulation of the forcing in the nearshore region. It appears that the most important consideration in nearshore forcing is the degree of complexity exhibited in this field. While the relative weights of stress to curl play an important role in the gross structure of the current system, the interaction of the diverse current structure driven by an equally diverse wind field can play an important role in the production of cold filaments and eddies.

B. RECOMMENDATIONS

The importance of using high resolution wind stress data in the nearshore region of a numerical model has been shown. The role of transient forcing, particularly in relation to this spatially varying climatological wind stress field, has yet to be clarified. A logical next step to this study is the use of a time series of climatological wind stress data, preferably of two tenths degree resolution, to force the model. This form of forcing would allow for not only a realistic wind field, but also an accurate seasonal pattern. Both a spatially and temporally varying forcing of this type would greatly help to clarify the role of wind forcing in the CCS. Once these wind forcing studies have been completed, parameters such as bottom and coastline topography should be incorporated into the model to study their effects on instability and mesoscale processes.

Another area of importance is the study of sudden, strong wind signals in the onset and intensification of upwelling. Wind events of this sort may also be of

importance in eddy generation (Carton, 1984; Carton and Philander, 1984). The incorporation of an intense wind stress forcing on an already established current system may be a simplistic but effective method of studying this phenomena.

Two additional projects are also recommended involving the model itself. First, the resolution of the model should be modified to allow for detection of frontal features. Fronts in the CCS have been observed with scales of 10 km or less (Mooers *et al.*, 1976). Reducing the model resolution to 1 km by 1 km vice the current 8 km by 10 km would be required to completely resolve these features. Secondly, the many regional models for the west coast of the United States should be coupled to derive a "total" CCS numerical model, encompassing the area from Baja California to Canada. Only by modeling the entire region can a true picture of the flow patterns in the CCS be properly simulated.

LIST OF REFERENCES

- Adamec, D., R.L. Elsberry, R.W. Garwood, Jr. and R.L. Haney, 1981: An embedded mixed layer-ocean circulation model. *Dyn. Atmos. Oceans*, 5, 69-96.
- Akima, H., 1978: A method of bivariate interpolation and smooth surface fitting for irregularly distributed data points. *ACM Trans. Math. Soft.*, 4, 148-159.
- Allen, J.S., 1980: Models of wind-driven currents on the continental shelf. *Ann. Rev. Fluid. Mech.*, 12, 389-433.
- Arakawa, A. and V.R. Lamb, 1977: Computational design of the basic dynamical processes of the UCLA general circulation model. In, *Methods in Computational Physics*, J. Chang, ed., Academic Press, 17, 173-265.
- Bakun, A., 1987: Applications of maritime data to the study of surface forcing of seasonal and interannual ocean variability in eastern boundary regions. Ph.D. dissertation, Oregon State University, Corvallis, Oregon, 226 pp.
- Batteen, M.L., 1989: Model simulations of a coastal jet and undercurrent in the presence of eddies and jets in the California Current System. In, *Poleward Flows on Eastern Boundaries*, S. Neshyba, C.N.K. Mooers, R.L. Smith and R.T. Barber, eds., Lecture Notes on Coastal and Estuarine Studies, Springer-Verlag, 263-279.
- Batteen, M.L. and Y.-J. Han, 1981: On the computational noise of finite-difference schemes used in ocean models. *Tellus*, 33, 387-396.
- Batteen, M.L., R.L. Haney, T.A. Tielking, and P.G. Renaud, 1989: A numerical study of wind forcing of eddies and jets in the California Current System. *J. Mar. Res.*, 47, 493-523.
- Bernstein, R.L., L.C. Breaker, and R. Whritner, 1977: California Current eddy formation: ship, air and satellite results. *Science*, 195, 353-359.
- Blumberg, A.F. and G.L. Mellor, 1987: A description of a three-dimensional coastal ocean circulation model. In, *Three-dimensional Coastal Ocean Models*, N. Heaps, ed., American Geophysical Union, 4, 1-16.
- Breaker, L.C., and C.N.K. Mooers, 1986: Oceanic variability off the central California coast. *Prog. in Oceanogr.*, 17, 61-135.

- Camerlengo, A.L. and J.J. O'Brien, 1980: Open boundary conditions in rotating fluids. *J. Comput. Physics*, 35, 12-35.
- Carton, J.A., 1984: Coastal circulation caused by an isolated storm. *J. Phys. Oceanogr.*, 14, 114-124.
- Carton, J.A., and S.G.H. Philander, 1984: Coastal upwelling viewed as a stochastic phenomena. *J. Phys. Oceanogr.*, 14, 1499-1509.
- Chelton, D.B., 1984: Seasonal variability of alongshore geostrophic velocity off central California. *J. Geophys. Res.*, 89, 3473-3486.
- Chelton, D.B., R.L. Bernstein, A. Bratkovich, and P.M. Kosro, 1987: The California Coastal Circulation Study. *EOS*, 68, 1, 12-13.
- Chelton, D.B., A.W. Bratkovich, R.L. Bernstein, and P.M. Kosro, 1988: Poleward flow off Central California during the spring and summer of 1981 and 1984. *J. Geophys. Res.*, 93, 10,604-10,620.
- Davis, R.E., 1985: Drifter observations of coastal surface currents during CODE: The method and descriptive view. *J. Geophys. Res.*, 90, 4741-4755.
- Emery, W.J. and L.A. Mysak, 1980: Dynamical interpretations of satellite-sensed thermal features off Vancouver Island. *J. Phys. Oceanogr.*, 10, 961-970.
- Freitag, H.P., and D. Halpern, 1981: Hydrographic observations off Northern California during May 1977. *J. Geophys. Res.*, 86, 4248-4252.
- Halliwell, Jr., G.R., and J.S. Allen, 1987: The large-scale coastal wind field along the west coast of North America, 1981-1982. *J. Geophys. Res.*, 92, 1861-1884.
- Halpern, D., 1976: Measurements of near-surface wind stress over an upwelling region near the Oregon Coast. *J. Phys. Oceanogr.*, 6, 108-112.
- Han, Y.-J., 1975: Numerical simulation of mesoscale ocean eddies. Ph.D. thesis, UCLA, 154 pp.
- Haney, R.L., 1974: A numerical study of the response of an idealized ocean to large-scale surface heat and momentum flux. *J. Phys. Oceanogr.*, 4, 145-167.
- Haney, R.L., 1985: Midlatitude sea surface temperature anomalies : A numerical hindcast. *J. Phys. Oceanogr.*, 15, 787-799.
- Haney, R.L., W.S. Shiver, and K.H. Hunt, 1978: A dynamical-numerical study of the formation and evolution of large scale ocean anomalies. *J. Phys. Oceanogr.*, 8, 952-969.

- Hickey, B.M., 1979: The California Current System - hypothesis and facts. *Prog. in Oceanogr.*, 8, 191-279.
- Holland, W.R., 1978: The role of mesoscale eddies in the general circulation of the ocean - numerical experiments using a wind-driven quasigeostrophic model. *J. Phys. Oceanogr.*, 8, 363-392.
- Holland, W.R. and M.L. Batteen, 1986: The parameterization of subgrid scale heat diffusion in eddy-resolved ocean circulation models. *J. Phys. Oceanogr.*, 16, 200-206.
- Huyer, A., 1983: Coastal upwelling in the California Current System. *Prog. in Oceanogr.*, 12, 259-284.
- Huyer, A., and P.M. Kosro, 1987: Mesoscale surveys over the shelf and slope in the upwelling region near Point Arena, California. *J. Geophys. Res.*, 92, 1655-1681.
- Ikeda, M., W.J. Emery, and L.A. Mysak, 1984a: Seasonal variability in meanders of the California Current System off Vancouver Island. *J. Geophys. Res.*, 89, 3487-3505.
- Ikeda, M., L.A. Mysak, and W.J. Emery, 1984b: Observation and modeling of satellite-sensed meanders and eddies off Vancouver Island. *J. Phys. Oceanogr.*, 14, 3-21.
- Ikeda, M., and W.J. Emery, 1984: Satellite observations and modeling of meanders in the California Current System off Oregon and Northern California. *J. Phys. Oceanogr.*, 14, 1434-1450.
- Kelly, K.A., 1985: The influence of winds and topography on the sea surface temperature patterns over the Northern California slope. *J. Geophys. Res.*, 90, 11,783-11,798.
- Kosro, P.M., and A. Huyer, 1986: CTD and velocity surveys of seaward jets off Northern California, July 1981 and 1982. *J. Geophys. Res.*, 91, 7680-7690.
- Lynn, R.J., K. Bliss and L.E. Eber, 1982: Vertical and horizontal distributions of seasonal mean temperature, salinity, sigma-t, stability, dynamic height, oxygen, and oxygen saturation in the California Current, 1950-1978. *CalCOFI Atlas 30*, State of Calif. Mar. Res. Comm., La Jolla, 513 pp.
- Lynn, R.J., and J.J. Simpson, 1987: The California Current System: The seasonal variability of its physical characteristics. *J. Geophys. Res.*, 92, 947-966.

- Magnell, B. and C. Winant, 1987: Real time currents from NCCCS. *The Coastal Transition Zone Newsletter*, 2, 10-17.
- McCreary, J.P., 1981: A linear stratified ocean model of the coastal undercurrent. *Phil. Trans. R. Soc. Lond. A*, 302, 385-413.
- McCreary, J.P., P.K. Kundu, S.-Y. Chao, 1987: On the dynamics of the California Current System. *J. Mar. Res.*, 45, 1-32.
- Mooers, C.N.K., C.A. Collins, and R.L. Smith, 1976: The dynamic structure of the frontal zone in the coastal upwelling region off Oregon. *J. Phys. Oceanogr.*, 6, 3-21.
- Mooers, C.N.K. and A.R. Robinson, 1984: Turbulent jets and eddies in the California Current and inferred cross-shore transports. *Science*, 223, 51-53.
- Nelson, C.S., 1977: Wind stress and wind stress curl over the California Current. *NOAA Tech. Rep. NMFS SSRF-714*, U.S. Dept. Commerce, 87 pp.
- Nelson, C.S. and D.M. Husby, 1983: Climatology of surface heat fluxes over the California Current Region. *NOAA Tech. Rep. NMFS SSRF-714*, U.S. Dept. Commerce, 155 pp.
- O'Brien, J.J., R.M. Clancy, A.J. Clarke, M. Crepon, R. Elsbery, T. Gammelsrod, M. MacVean, L.P. Roed, and J.D. Tompson, 1977: Upwelling in the ocean: Two- and Three-dimensional models of upper ocean dynamics and variability. In, *Modelling and Prediction of the Upper Layers of the Ocean*, E.B. Kraus, ed., Pergamon Press, New York, 178-228.
- Parrish, R.H., A. Bakun, D.M. Husby, and C.S. Nelson, 1983: Comparative climatology of selected environmental processes in relation to eastern boundary current pelagic fish production. In, *Proceedings of the expert consultation to examine changes in abundance and species of neritic fish resources*, G.D. Sharp and J. Csirke, eds., San Jose, Costa Rica, 18-19 April 1983. *FAO Fish Rep.* (291, Vol 3: 731-778).
- Paulson, C.A., and J.J. Simpson, 1977: Irradiance measurements in the upper ocean. *J. Phys. Oceanogr.*, 7, 952-956.
- Pedlosky, J., 1974: Longshore currents, upwelling and bottom topography. *J. Phys. Oceanogr.*, 4, 214-226.
- Philander, S.G.H. and J.-H. Yoon, 1982: Eastern boundary currents and coastal upwelling. *J. Phys. Oceanogr.*, 12, 862-879.

- Pond, S. and G.L. Pickard, 1983: *Introductory Dynamical Oceanography*. Second Edition, Pergamon Press, New York, 329 pp.
- Rabiner, L.R., M.R. Sambur, and C.E. Schmidt, 1975: Applications of a nonlinear smoothing algorithm to speech processing. *IEEE, Trans. Acoustics, Speech, Signal Proc.*, ASSP-23, 552-557.
- Reed, R.K., and D. Halpern, 1976: Observations of the California Undercurrent off Washington and Vancouver Island. *Limnol. Oceanogr.*, 21, 389-398.
- Reid, J.L., 1962: Measurements of the California Countercurrent at a depth of 250 meters. *J. Mar. Res.*, 20, 134-137.
- Reid, J.L., 1988: Physical oceanography, 1947-1987. *Calif. Coop. Oceanic Fish. Invest. Rep.*, 29, 42-65.
- Reid, J.L. and R.A. Schwartzlose, 1962: Direct measurements of the Davidson Current off Central California. *J. Geophys. Res.*, 67, 2591-2597.
- Robinson, A.R., 1983: *Eddies in Marine Science*. Springer-Verlag, New York, 609 pp.
- Robinson, A.R., J.A. Carton, C.N.K. Mooers, L.J. Walstad, E.F. Carter, M.M. Rienecker, J.A. Smith and W.G. Leslie, 1984: A real-time dynamical forecast of synoptic/mesoscale eddies. *Nature*, 309, 781-783.
- Rutherford, M.J., 1989: Modelling studies of the Leeuwin Current using a high-resolution primitive equation model. Master's Thesis. Naval Postgraduate School, Monterey, Ca., pp.
- Semtner, A.J., and Y. Mintz, 1977: Numerical simulation of the Gulf Stream and mid-ocean eddies. *J. Phys. Oceanogr.*, 7, 208-230.
- Strub, P.T., J.S. Allen, A. Huyer, and R.L. Smith, 1987: Large-scale structure of the spring transition in the coastal ocean off Western North America. *J. Geophys. Res.*, 92, 1527-1544.
- Sverdrup, H.U., M.W. Johnson, and R.H. Fleming, 1942: *The Oceans: Their Physics, Chemistry, and General Biology*. Prentice-Hall, Englewood Cliffs, New Jersey, 1087 pp.
- Thomson, R.E., 1984: A cyclonic eddy over the continental margin off Vancouver Island: Evidence for Baroclinic instability. *J. Phys. Oceanogr.*, 14, 1326-1348.
- Tielking, T.A., 1988: Wind forcing of eddies and jets in the California Current System. Master's Thesis. Naval Postgraduate School, Monterey, Ca., 107 pp.

- Watts, D.R., 1983: Gulf Stream variability. In, *Eddies in Marine Science*, A.R. Robinson, ed., Springer-Verlag, New York, 114-144.
- Watts, D.R. and W.E. Johns, 1982: Gulf Stream meanders: Observations on propagation and growth. *J. Geophys. Res.*, 87, 9467-9476.
- Wickham, J.B., A.A. Bird, and C.N.K. Mooers, 1987: Mean and variable flow over the central California continental margin, 1978-1980. *Cont. Shelf Res.*, 7, 827-849.
- Weatherly, G.L., 1972: A study of the bottom boundary layer of the Florida Current. *J. Phys. Oceanogr.*, 2, 54-72.
- Wright, D.G., 1980: On the stability of a fluid with a specialized density stratification. Part II. Mixed baroclinic-barotropic instability with application to the Northeast Pacific. *J. Phys. Oceanogr.*, 19, 1307-1322.

INITIAL DISTRIBUTION LIST

	No. Copies
1. Defense Technical Information Center Cameron Station Alexandria, VA 22304-6145	2
2. Library, Code 0142 Naval Postgraduate School Monterey, CA 93943-5002	2
3. Chairman (Code 68Co) Department of Oceanography Naval Postgraduate School Monterey, CA 93943	1
4. Chairman (Code 63Rd) Department of Meteorology Naval Postgraduate School Monterey, CA 93943	1
5. Dr. M.L. Batteen (Code 68Bv) Department of Oceanography Naval Postgraduate School Monterey, CA 93943	3
6. Dr. A.J. Semtner (Code 68Se) Department of Oceanography Naval Postgraduate School Monterey, CA 93943	1
7. Director, Naval Oceanography Division Naval Observatory 34th and Massachusetts Avenue NW Washington, DC 20390	1
8. Commanding Officer Fleet Numerical Oceanography Center Monterey, CA 93943	1
9. Commanding Officer Naval Environment Prediction Research Facility Monterey, CA 93943	1

- | | | |
|-----|--|---|
| 10. | Naval Ocean Research and Development Activity
NSTL Station
Bay St. Louis, MS 39522 | 1 |
| 11. | Dr. R.L. Haney (Code 63Hy)
Department of Meteorology
Naval Postgraduate School
Monterey, CA 93943 | 1 |
| 12. | Office of Naval Research (Code 420)
800 N. Quincy Street
Arlington, VA 2217 | 1 |
| 13. | Dr. Andy Bakun
Pacific Fisheries Environment Group
SWFC/NMFS/NOAA
P.O. Box 831
Monterey, CA 93942 | 1 |
| 14. | CDR Craig S. Nelson (Code 68)
Department of Oceanography
Naval Postgraduate School
Monterey, CA 93943 | 1 |
| 15. | Dr. Frank Schwing
Pacific Fisheries Environment Group
SWFC/NMFS/NOAA
P.O. Box 831
Monterey, CA 93942 | 1 |
| 16. | Dr. Robert L. Smith
College of Oceanography
Oregon State University
Corvallis, OR 97331 | 1 |
| 17. | Dr. Adriana Huyer
College of Oceanography
Oregon State University
Corvallis, OR 97331 | 1 |
| 18. | Dr. D. Evans
Office of Naval Research (Code 1122PO)
800 N. Quincy Street
Arlington, VA 2217 | 1 |

- | | | |
|-----|---|---|
| 19. | Dr. Tom Kinder
Office of Naval Research (Code 1122CS)
800 N. Quincy Street
Arlington, VA 2217 | 1 |
| 20. | Director of Research Administration (Code 012)
Naval Postgraduate School
Monterey, CA 93943 | 1 |
| 21. | LT. Robert Edson (Code 68)
Department of Oceanography
Naval Postgraduate School
Monterey, CA 93943 | 5 |